The Nature of the Decadal Variability of Surface Climate Over the North Atlantic Ocean

-------- Coupled Ocean-Atmosphere-Sea Ice Interaction Organized by Damped Ocean Mode

by

Feng He

A thesis submitted in partial fulfillment of the requirements for the degree

of

MASTER OF SCIENCES

(Atmospheric and Oceanic Sciences)

Supported by the

Center for Climatic Research

Gaylord Nelson Institute for Environmental Studies

at the

University of Wisconsin-Madison

2008

APPROVED

Advisor: _____

Title: Professor

Date: 8/18/2008

The University of Wisconsin - Madison
The Graduate School

Candidate for the degree of **MS**

Atmospheric and Oceanic Sciences

For: **Summer, 2008**

He, Feng

9026511742

The undersigned report that all degree requirements have been met on 08/18/08
(Date Completed MMDDYY)

If a thesis will be submitted to Memorial Library, indicate date to be delivered and thesis title.

(Date MMDDYY) *(Title)* The Nature of the Decadal Variability of Surface climate over the North Atlantic Ocean — Coupled Ocean-Atmosphere-Sea Ice interaction organized by Damped Ocean Mode

Will the student continue for a PhD/DMA in the department/program? (yes) no *(circle one)*

We recommend that the above named candidate be awarded the degree indicated

Committee Member Names	**Signature of Committee Members**
Liu, Zhengyu	
Vimont, Daniel J.	
McKinley, Galen A.	

Date Thesis Deposited in Memorial Library

To my parents

for their love and encouragement

The Nature of the Decadal Variability of Surface Climate Over the North Atlantic Ocean

-------- Coupled Ocean-Atmosphere-Sea Ice Interaction Organized by Damped Ocean Mode

by

Feng He

Under the supervision of Professor Zhengyu Liu

ABSTRACT

The nature of the observed 11~14-year decadal variability of the surface climate over the North Atlantic Ocean is investigated using the Fast Ocean Atmosphere Model (FOAM) and its data-atmosphere configuration. A 14~16-year damped ocean mode, characterized by the decadal variability of Atlantic Meridional Overturning Circulation (AMOC) and southward-moving western boundary low frequency waves, is found to be able to organize coupled atmosphere–ocean–sea ice interaction in the North Atlantic and produce the decadal variability of the surface climate in this region. In the North

Atlantic, the coupled simulation produces a faithful simulation of the observed decadal variability in terms of the pattern and periodicity of the main variability of sea surface temperature (SST), surface air temperature (SAT) and sea level pressure (SLP). Moreover, the coupled simulation also bears the observed dipole pattern of dynamic topography in West North Atlantic and the Great Salinity Anomaly (GSA)-like decadal salinity signature in the subpolar gyre. These connections between the coupled simulation and observations suggest coupled ocean-atmosphere-sea ice interaction organized by damped ocean mode is a plausible explanation for the observed decadal variability in this region.

In the coupled simulation, two physical processes, namely SAT-convection feedback and sea ice-convection feedback, were found to be critical for the decadal variability of surface climate in this region. The SAT-convection feedback is the local effect of SAT on oceanic convections in the Labrador Sea. Under cold episodes of surface climate in the North Atlantic, the damped ocean mode is pushed to its "positive" mode when the cold air induces stronger convective activity in the Labrador Sea. The stronger convections produce more vigorous AMOC and the trough of western boundary low frequency waves in the subpolar gyre. The clockwise circulation associated with the trough of western boundary low frequency waves induces more heat transport into the subpolar North Atlantic and generates warmer SST and SAT. This gives rise to the warm episodes of surface climate in the North Atlantic and a new cycle starts. The sea ice-convection feedback is the effect of salinity anomaly on oceanic convections in Labrador Sea due to nonlocal sea ice melting/growing. The

aforementioned warmer SAT induces more sea ice melting and results in low sea surface salinity (SSS) in the northern subpolar gyre, especially in Irminger Sea. After the low salinity is transported into Labrador Sea, it suppresses local convective activity and acts jointly with SAT-convection feedback to switch the damped ocean mode into its "negative" mode.

The damped ocean mode was uncovered in the stochastic atmospheric simulation and found to be responsible for the decadal time scale in the coupled simulations. The stochastic atmospheric simulation also reproduces the southward propagation of western boundary low frequency waves and the decadal variability of AMOC, but fails maintaining the decadal variability of ocean temperature and salinity in the North Atlantic both at surface and subsurface. This discrepancy between the coupled and stochastic atmosphere simulation underscores the critical role of coupled ocean-atmosphere-sea ice interaction in simulating the decadal variability of surface climate in the North Atlantic. In the coupled simulation, the atmospheric response to the subpolar SST substantially enhances the variability of the damped ocean mode on decadal time scales: when the subpolar SST is warmer, the warm-ridge dynamic response of the atmosphere provides the positive feedback by inducing northward Ekman transport to further increase the warming of SST; the local SAT-convection feedback and the remote sea ice-convection feedback act jointly to provide the delayed negative feedback in coupled ocean-atmosphere-sea ice interaction. In fact, given the insurmountable damping effect of the stochastic atmosphere, it is impossible to sustain the decadal variability of surface climate without any atmospheric response. Therefore

it is coupled ocean-atmosphere-sea ice interaction organized by the damped ocean mode that generates the decadal variability of the surface climate in the North Atlantic Ocean.

ACKNOWLEDGEMENTS

The completion of this thesis would have not been possible without the help from many people. I am deeply indebted to my adviser, Professor Zhengyu Liu, who brought me into the fascinating field of the decadal variability research in the North Atlantic and patiently guided me to build my own research habit. I am always encouraged by his passion on science and appreciate his special insights during our discussions. It is my great pleasure to have this opportunity to work under Professor Liu's guidance.

I am also grateful to Dr. Lixin Wu and Dr. Donna Lee, who helped me to start my journey on climate modeling and gave me many suggestions on the details of the climate analysis that helped me to improve my ability of exploring the climate dynamics from massive model outputs. Dr. Wu taught me the coupled modeling surgery technique that has been used extensively in this thesis. Dr. Lee helped me on the data atmosphere configuration and heat/salt budget analysis that have been used to substantially clarify the proposed mechanism in this work.

I would also like to thank Pat Behling for her computer assistant and advice on this study. She provided excellent resources for me to have a smooth and quick transition from PC to Unix environment during the first semester of my graduate study. I always get encouragement and advice from her so that I can move forward without hesitation.

I also want to express my gratitude to Melanie Woodworth, Marcia Verhage, Mark

Marohl and Lois Blackbourn for their excellent administrative work that provided the most comfortable research environment I ever had.

I would also want to thank all the faculties and researchers in CCR, especially the students in Dr. Liu research group: Yafang Zhong, Yun Liu, Guangshan Chen, Wei Liu, Na Wen, Andrew Park, John-Paul Argenti, Xiaojie Zhu, Jun Cheng. The weekly student meeting has always broadened my horizon on climate research.

A special thanks goes to my bachelor thesis adviser, Dr. Jiwei Tian, who introduced me into global climate research and provided me with the framework of my knowledge on climate dynamics.

Another special thanks goes to my life group from Blackhawk church, which transformed my attitude toward the people and helped me on my journey of a humble and righteous life.

I am also grateful for the support from my parents and parent-in-laws. It is their prayers that helped me to overcome the difficulties.

As always, my wife, Xiaoyi Sun and my son, Zijun He, deserve the most gratitude from me. We enjoy every minute of our life and share with each other the happiness

and sadness. It is their understanding and support that gave me the strength and preparation to move forward and enjoy my work as a climate researcher.

I would like to thank Gokhan Danabasoglu, Tom Delworth, John Marshall, Steve Vavrus, and Lixin Wu for very useful comments at various stages of this study. This research was funded by DOE and NSF. This research used resources of the National Energy Research Scientific Computing Center, which is supported by the Office of Science of the U.S. Department of Energy under Contract No. DE-AC02-05CH11231. The simulation was conducted on supercomputers Seaborg and Bassi and the results were analyzed on the analysis server DaVinci.

TABLE OF CONTENTS

Abstract iii

Acknowledgement vii

Table of Contents x

1 Introduction 1

2 Model and Experimental design 5

3 Decadal Variability in the North Atlantic 8

3.1 Observed Decadal Variability in the North Atlantic ……...…….8

3.2 Simulated Decadal Variability in the North Atlantic ……...……...……9

4 The Mechanism of the Decadal Variability of Atlantic Meridional Overturning Circulation 11

4.1 The Decadal Variability of AMOC in Coupled Simulation ……...……...…..…11

4.2 A Survey of the Decadal Variability in the North Atlantic Sector in Coupled Simulation …....12

4.3 The Synthesis of the Maximum Lagged Correlation in the Coupled Simulation ……....…….15

4.4 The Illustration of the Mechanism via Lagged Correlation Analysis ....…….……...……..18

5 The Evaluation of the Mechanism via Sensitivity Experiments 21

5.1 Stochastic Run: the Discovery of Damped Ocean Mode in FOAM …….…….....21

5.2 Switch-on Run: a Case Study on the Response of AMOC to NAO Forcing ……..... 23

5.3 Partial Blocking Run: the Necessity/Non-Necessity of Subpolar/Subtropical Dynamics of Sustaining the damped ocean mode……..……...……...24

5.4 Decadal AMIP Run: a Case Study on the Response of Atmosphere to Decadal SST Forcing ...26

6 Discussions and Conclusion 31

6.1 The Decadal Variability of the Dynamic Topography …….....……..31

6.2 The Great Salinity Anomaly……..……..……...……..36

6.3 The Decadal Variability of the Sea Surface Temperature …….....…….40

6.4 The Relevance of the Proposed Mechanism to the Earlier Investigations ……..…....46

7 Figure and Table Captions 49

8 References 59

9 Figures 66

1. Introduction

The decadal variability of surface climate in the North Atlantic is a great challenge to our understanding of the climate system and has been shown to have significant impact on the climate over North American and Europe [Sutton and Hodson, 2005]. In search of its origin, the Atlantic Meridional Overturning Circulation (AMOC) is regarded as one of the best candidates on this time scale. Both the observational [Deser and Blackmon, 1993; Häkkinen, 2000; Kushnir, 1994; Tourre et al., 1999] and the modeling studies [Collins et al., 2006; Griffies and Bryan, 1997] suggest that the decadal variability in the North Atlantic sector may be closely related with AMOC. However, the nature of the decadal variability of AMOC has been highly debated ever since the first coupled simulation of AMOC was performed using the GFDL model [Delworth et al., 1993] (D93, hereafter). Four schools of thoughts have been put forward to account for the decadal variability in D93. Greatbatch and Zhang [1995] attributed D93 oscillation to a self-sustained active ocean-alone mode. After comparing the results between a four-box model and D93, Griffies and Tziperman [1995] suggest the decadal variability of D93 is due to a damped ocean mode excited by stochastic atmospheric forcing. Even though the original analysis in D93 suggests the irregular oscillations in AMOC results primarily from oceanic processes, it did acknowledge the trigger effect from the stochastic atmospheric forcing. A similar stochastic forced decadal variability is also present in Hamburg Large-Scale Geostrophic (LSG) ocean model [Weisse et al., 1994]. A systematic examination of the response of the ocean component of GFDL model to prescribed flux forcing leads Weaver and Valcke [1998] to refuting the first two mechanisms and drawing the

conclude that the decadal variability comes from a coupled air-sea interaction. This conclusion is also supported by the coupled simulation of ECHAM-3/LSG model [Timmermann et al., 1998]. Delworth and Greatbatch [2000] did an extended investigation of D93 and attributed the decadal variability to an uncoupled oceanic response to internal low-frequency atmospheric variability. Note that one of the common flaws in the early modeling studies [Delworth et al., 1993; Delworth and Greatbatch, 2000; Timmermann et al., 1998] is flux correction, which can potentially introduce unrealistic impact on climate variability.

This work aims to reexamine the above four schools of thoughts, in particular, to answer whether the decadal variability of AMOC results from a coupled mode or simply from an oceanic response to internal low-frequency atmospheric forcing. The coupled climate model we are using is Fast Ocean Atmosphere Model (FOAM) [Jacob R. L., 1997], which has been successfully run for 6,000 years without using flux corrections [Liu et al., 2006]. In section 2, we will introduce the coupled model and the design of the sensitivity experiment. In section 3, we will compare the simulated decadal variability of sea surface temperature (SST), surface air temperature (SAT) and sea level pressure (SLP) with that from observation and show the capability of FOAM in simulating the decadal variability of surface climate in the North Atlantic. In section 4, firstly, the decadal variability of AMOC is analyzed to demonstrate that AMOC accounts for the decadal variability of the North Atlantic SST in FOAM. Secondly, we carry out a survey of the decadal variability in the North Atlantic sector in the coupled simulation. Thirdly, we perform the unprecedented synthesis of the maximum lagged correlation and the lag of the maximum lagged correlation in

FOAM's control simulation. This synthesis is based on the leading PC of the complete list of 37 two or three-dimensional principal variables and is able to show that the decadal variability of AMOC in the control simulation comes from coupled air-sea interactions. Lastly, we illustrate the mechanism of the decadal variability of AMOC using the lagged correlation analysis. In section 5, a suite of sensitivity experiments is conducted to verify some of the key physical processes in the proposed mechanism. The data-atmosphere configuration of FOAM is used to demonstrate the decadal variability of AMOC can also result from stochastic atmospheric forcing. Hence a damped ocean mode is uncovered in FOAM's North Atlantic region. We will also demonstrate two fundamental elements of the damped ocean mode in the switch-on experiment: the response of AMOC to atmospheric forcing and the salinity's delayed negative feedback on AMOC. Two partial blocking (PB) experiments are used to show explicitly the ocean dynamics in the subpolar gyre is necessary for the decadal variability in the North Atlantic. Lastly, a decadal AMIP (Atmospheric Model Intercomparison Project) -type experiment [Peng et al., 2003] demonstrates the evolution of atmospheric response to the decadal variability of subpolar SST. We conclude this work in section 6 with focuses on the data-model comparison. Lagged regression map are used to show the similarities between the coupled simulation and observations in terms of the evolution of the decadal variability of dynamic topography, ocean salinity and temperature in the North Atlantic. Furthermore, heat and salt budget analysis is utilized to elucidate the detailed physical processes involved in coupled atmosphere–ocean–sea ice interaction. By this means, we demonstrate the coupled atmosphere–ocean–sea ice interaction organized by the damped ocean mode is

a feasible mechanism for the observed decadal variability of surface climate in this region. In the end, we will briefly discuss the relevance of this work to the earlier studies.

2. Model and Experimental design

We report on the results from six simulations using four modeling techniques (Table 1). In addition to the fully coupled control simulation (CTRL), we used two data-atmosphere (DATM) simulations to uncover the damped ocean mode and explore its dynamics, two partial blocking (PB) simulation to demonstrate the vital role of subpolar oceanic dynamics in the damped ocean mode and one decadal AMIP-type simulation to investigate the atmospheric response to SST. Note that no filter has been used in this analysis in order to conserve the objectivity of this study.

In coupled configuration, FOAM's atmospheric component is a parallel version of National Center for Atmospheric Research (NCAR) Community Climate Model (CCM) 2.0 at R15, but with atmospheric physics replaced by CCM3, and with vertical resolution of 18 levels. The ocean model is similar to the Geophysical Fluid Dynamics Laboratory (GFDL) Modular Ocean Model (MOM) with a resolution of 1.4° latitude × 2.8° longitude × 24 levels. The basic land model in FOAM is taken from the default land model of CCM2; the sea ice model uses thermodynamics of NCAR's CSIM version 2.2.6. Without flux correction, FOAM produces a tropical climatology similar to most of the state-of-the-art climate models [Liu et al., 2004]. FOAM also produces reasonable ENSO [Liu et al., 2000] and Tropical Atlantic variability [Wu and Liu, 2002].

Data atmosphere (DATM) configuration is a necessary step to explore the role of ocean and sea ice dynamics in the coupled model. In this configuration, the atmosphere component of the coupled model is replaced by prescribed data input. To examine the existence of the damped ocean mode, we performed a 400-year stochastic data-

atmosphere (DATM_STOC) simulation with FOAM's atmosphere component replaced by prescribed stochastic atmospheric forcing dataset. In this simulation, an optimal atmospheric forcing pattern is derived from the lagged regression of surface data from CTRL onto the AMOC index (discussed later). In particular, we chose -2 as the lag, because the decadal variability of the atmosphere leads the index of AMOC by two years. Then the stochastic atmospheric forcing dataset is compiled by multiplying the optimal atmospheric forcing pattern by a white noise index. This white noise index has a normal distribution with the mean of zero and the standard deviation of two. Note that DATM_STOC is also a robust test on whether or not the decadal variability of AMOC originates from atmospheric internal low frequency variability.

The 20-year switch-on experiment (DATM_SWITCH) was also based on DATM configuration and was employed to excite the damped ocean mode and verify the intrinsic time scale found in CTRL. The atmospheric forcing dataset in DATM_SWITCH is compiled by multiplying the optimal atmospheric forcing pattern by a step function [Eden et al., 2002; Griffies and Tziperman, 1995] with 0 in the first 5 years and 2 for the rest of 15 years. It simulates a scenario in which an optimal atmospheric forcing with twofold standard intensity is suddenly switched on and kept constant afterward. By this means, we obtain the pure oceanic adjustment under a single optimal atmospheric forcing.

Partial blocking (PB) scheme [Liu et al., 2004] is used to evaluate the role of the ocean dynamics in the coupled simulation. In the middle of the Atlantic Ocean, a narrow latitudinal band of salinity and temperature below the mixed layer was restored to the seasonal-cycle value in order to block the propagation of oceanic Rossby waves

and any other oceanic anomalies that cross the Atlantic basin. By this means, we stop the ocean adjustment process and the coupled simulation evolves without the contribution from the ocean dynamics. In particular, we put PB scheme between 15N and 35N in PBATL1535N and between 35N and 50N in PBATL3550N to evaluate the role of subtropical and subpolar ocean dynamics in the coupled simulation.

Partial coupling (PC) scheme [Liu et al., 2004] is designed to evaluate the atmospheric response to SST in a coupled GCM. The CGCM (coupled general circulation model) AMIP-type simulation [Liu and Wu, 2004; Wu and Liu, 2005] is regarded as the most natural way to study the atmospheric response to SST forcing as compared with other AGCM (atmospheric general circulation model) AMIP-type simulations [Peng et al., 2003]. In the PC region, the atmosphere is forced by prescribed SST, while the ocean is still forced by the atmosphere through the coupler. By this means, ocean and atmosphere are coupled actively only outside the PC region, and the local coupling within the PC region is totally eliminated. In this study, a pair of 20-member-ensemble PC experiments, named as decadal atmosphere response run (D_ATM_R), is performed with each pair of the corresponding ensemble members starting from the same initial condition borrowed from CTRL. In the PC region of the zero-anomaly simulation, climatological seasonal cycle of SST is prescribed; in the PC region of the decadal-anomaly run, the SST anomaly with decadal variability is added as the additional forcing. The 20-member ensemble of the differences between the decadal-anomaly run and zero-anomaly run is analyzed via EOF analysis to derive the atmospheric response pattern and atmospheric response coefficient.

3 Decadal Variability in the North Atlantic

3.1 Observed Decadal Variability in the North Atlantic

We first performed the EOF analysis of the North Atlantic SST, SAT and SLP from the observations. SST and SLP data are derived from 1^o x 1^o HadISST dataset (1870 ~2007) [Rayner et al., 2003] and 5^o x 5^o HadSLP2 dataset (1860~2004) [Allan and Ansell, 2006][1]. SAT data are derived from 4^o x 6^o ICOADS dataset (1900-2006) [Woodruff et al., 2005]. We use 10N-80N and 80W-0 as the domain for the analysis. The leading EOF from wintertime (DJF) SST explains 26% of the total variance and the largest loadings are in subpolar region (Fig. 1a1). The spectrum of the leading PC (Fig. 1a2) shows a broadband peak at 10~20-year period and the spectrum from 11 to 14 years is significant over 95% confident level. This is consistent with the analysis of Tourre et al. [1999], who analyzed Kaplan's datasets [Kaplan et al., 1998; Kaplan et al., 2000] and found 11.4-year significant periodicity in the joint SST and SLP field using MTM-SVD method. In terms of SAT, the leading EOF explains 20% of the total variance and exhibits similar pattern (Fig. 1b1) as that from SST (Fig. 1a1). Note that there are substantial missing data in northern subpolar gyre and the negative loadings off the US coast are much stronger. However, the spectrum (Fig. 1b2) of the leading PC from the observed wintertime SAT has an even more significant (>95%) peak

[1] *HadSLP2 data provided by the NOAA/OAR/ESRL PSD, Boulder, Colorado, USA, from their Web site at http://www.cdc.noaa.gov*

around 11-16 years. The leading EOF (Fig. 2a1) of annual SLP explains 52% of the total variance and exhibits the dominant North Atlantic Oscillation (NAO) [Hurrell et al., 2003] pattern. The spectrum (Fig. 2a2) of the leading PC of the SLP doesn't show the similar peak between 11~16 years, but has a significant peak around 8 years, whose origin needs further investigation.

3.2 Simulated Decadal Variability in the North Atlantic

The 400-year control run of FOAM can simulate the main characteristics of the mean climate in the North Atlantic (Fig. 3). For example, the 400-year annual mean of barotropic streamfunctions (Fig. 3a) demonstrates the model has reasonable subpolar and subtropical gyres. The maximum convective variability in this model resides in the Labrador Sea (Fig. 3b). Due to the coarse resolution, the model simulates quite a diffusive Gulf Stream that fails maintaining the strong SST gradient (Fig. 3c) along its path. SSS has its maximum gradient in Irminger Sea, Labrador Sea and the coastal region off Newfoundland. The model also fails simulating the Atlantic inflow from northeast Atlantic into the Norwegian Sea. As a result, SSS in Norwegian Sea can not maintain the strong gradient along the East Greenland Current (Fig. 3d).

Compared with the observations, FOAM produces fairly good decadal variability in extratropical Atlantic. The leading EOF (Fig. 1c1) of annual SST from CTRL explains 36% of total variance and exhibits three similar features as found in observations: the largest loadings in the subpolar region, the second largest loadings in eastern subtropical Atlantic and the smallest loadings off the east coast of the United States. The power spectrum (Fig. 1c2) of the leading PC has a sharp and significant (95%)

peak around 14-16 years. As to SAT, the leading EOF explains 50% of total variance and has the largest loadings in subpolar region (Fig. 1d1). The spectrum (Fig. 1d2) of SAT exhibits a sharp and significant (>95%) spectral peak around 14-16 years as well. The leading EOF (Fig. 2b1) of SLP explains 52% of the total variance and exhibits the NAO-like pattern, but the southern center of the NAO shifts eastward by 20-degree longitude to Azores. The spectrum (Fig. 2b2) of the leading PC of SLP exhibits the same 14~16-year significant (>95%) peak as that of SST and SAT from CTRL, suggesting it is likely that the decadal variability in the North Atlantic comes from coupled air-sea interaction. In summary, both the observation and CTRL have pronounced decadal variability in SST, SAT and SLP in the North Atlantic. The 10~20-year decadal variability in the North Atlantic has also been successfully simulated in other coupled climate model simulations, but the nature of the decadal variability in these models still merits further investigation [Grötzner et al., 1998; Selten et al., 1999].

4 The Mechanism of the Decadal Variability of Atlantic Meridional Overturning Circulation

4.1 The Decadal Variability of AMOC in Coupled Simulation

The largest loadings of leading EOF of annual SST from CTRL in the subpolar region prompt us to the analysis of AMOC (Fig. 4). The 400-year average of AMOC (Fig. 4a) has a maximum of 14 Sv (1 Sv = 10^6 m^3/s), close to the 15Sv estimation from hydrographic data [Ganachaud and Wunsch, 2000]. The sinking region of AMOC is located at 56N, where deep convections in the Labrador Sea draw the surface water into deep ocean to form the North Atlantic Deep Water. The penetration of the Antarctic Bottom Water reaches 20N and has an intensity of ~8 Sv. The leading EOF of AMOC (Fig. 4b) explains 47% of the total variance and bears a monopole pattern confined between 40N and 60N. The maximum loadings are at the same location where the mean AMOC maximizes. The spectrum of the leading PC (Fig. 4c) exhibits the similar peak as that found in SST (Fig. 1c2). The sharp peak at 12~16 years is well over 95% confident level and the shape of the spectrum clearly demonstrates the tight connection between AMOC and SST. Note that the consistency of the 12~16-year decadal variability between the coupled model simulation of AMOC and the observations from the North Atlantic is rarely reported. In most coupled model simulations, the decadal variability of AMOC has a time scale about 25~50 years [Delworth et al., 1993; Dong and Sutton, 2005; Timmermann et al., 1998]. Based on a hybrid simulation, Eden and Greatbatch [2003] reported a 12~16-year decadal oscillation after they coupled a statistical atmosphere model to an ocean model of the

North Atlantic. On the other hand, we found AMOC is leading SST by 2 years with a lagged correlation (Fig. 10) of ~0.6 between the two leading PCs. If the three dimensional (3D) North Atlantic temperature instead of SST is used for the EOF analysis, AMOC can lead 3D ocean temperature by 2 years with a lagged correlation of ~0.8 (Fig. 10). The lagged correlation analysis strongly demonstrates the causality between SST and AMOC: decadal variability of SST in CTRL is driven by the decadal variability of AMOC--but what is the mechanism producing the decadal variability of AMOC?

4.2 A Survey of the Decadal Variability in the North Atlantic Sector in Coupled Simulation

In order to find the origin of the decadal variability of AMOC, we did a complete survey of the decadal variability of model output from the coupled simulation. To provide the necessary background for the proposed mechanism, we summarized the decadal variability of some key variables in this section (Fig. 5). The 1st EOF of the barotropical streamfunction (BSF, Fig. 5a1) explains 45% of the total variance and has a pronounced decadal variability between 10 to 16 years. The pattern of the 1st EOF exhibits a dipole in the West North Atlantic, with one center in Labrador Sea and the other off the east coast of the North America. As will be discussed in Section 6, the dipole pattern of the BSF is caused by the passage of western boundary low frequency waves instead of the barotropical response of the ocean circulation to the surface wind stress, because the bottom topography off the coast is not nil and the JEBAR effect is significant [Mellor, 1999]. The 1st EOF of the sea surface salinity (SSS, Fig. 5c1)

explains 31% of the total variance and has discernible decadal variability between 11 to 16 years as well as marginally significant multidecadal variability between 20 and 50 years. The main variability of SSS occupies the subpolar gyre with its maximum in the Irminger Sea. The 1st EOF of the sea ice fraction (Fig. 5b1) explains 38% of the total variance and has a pronounced decadal variability between 14 to 16 years. The main variability of sea ice fraction resides in the northern subpolar gyre, especially in Irminger Sea. The 1st EOF of the convective frequency (Fig. 5d1) explains 40% of the total variance and has a pronounced decadal variability between 5 and 10 years. The main variability of the convective adjustment occurs in the Labrador Sea.

It is instructive to compare the two-dimensional (2D) EOFs and spectra of the surface quantity of 3D variables with their 3D EOFs and spectra (Fig. 6), as the vertical structure of the decadal variability can be revealed. As to the 3D ocean temperature, the 1st EOF explains 20% of the total variance and has pronounced decadal variability between 12 and 16 years. Compared with SST, the 1st EOF of 3D ocean temperature has almost no variability for periods less than 5 years, whereas the 30~50 years multidecadal variability is more discernible. On the surface, the pattern of the 1st EOF (not shown) is similar to that of SST (Fig. 1c1), with main variability located in the subpolar gyre. However, at 1000m, the 1st EOF exhibits a dipole pattern with one center in the Labrador Sea and the other off the east coast of the North America. As will be discussed in section 6, this dipole deep-sea temperature signal is produced by the passage of the western boundary low frequency waves. As to the salinity, the 1st EOF explains 36% of the total variance and has pronounced decadal variability. Compared with SSS (Fig. 5b2), the 1st EOF of 3D salinity has much more

distinctive decadal and multidecadal variability between 11 and 16 years and between 30 and 50 years, respectively. The 1st EOF of 3D salinity also has no variability for periods less than 5 years. On the surface, the pattern of the 1st EOF (not shown) is similar to that of SSS as well, with main variability located in the subpolar gyre. However, at 300m, the 1st EOF exhibits a dipole pattern with one center in Irminger Sea and the other in Labrador Sea. As will be discussed in section 6, this dipole subsurface salinity signal is due to the mean zonal transport of the salinity anomaly from Irminger Sea into Labrador Sea. The 1st EOF of 3D air temperature and specific humidity explains 34% and 19% of the total variance, respectively. Both spectra exhibit distinctive decadal variability between 14 and 16 years. On the surface, the 1st EOFs of 3D air temperature and humidity show that the main variability of both variables resides in the subpolar gyre. There is also minor variability found in the subtropics for specific humidity, but not for air temperature. Note that both the spectra and the EOFs of 3D air temperature and relative humidity on the surface show little difference from those of SAT and surface specific humidity (not shown). Furthermore, the vertical structure of the 3D EOFs of both air temperature and specific humidity is equivalent barotropic with roughly linear decrease of EOF coefficients (not shown).

It is also informative to show the decadal variability of heat flux to give some clues on the atmosphere-ocean interactions. The 1st EOFs (Fig. 7) of sensible heat, latent heat, longwave radiation and short wave radiation flux explain 24%, 11%, 41% and 33% total variances, respectively. Radiative heat flux bear distinctive decadal variability between 14 and 16 years and the main variability resides in the subpolar gyre with the maxima in Irminger Sea. The main variability of latent heat flux is also

in the subpolar gyre and is enhanced on decadal time scales as well, albeit not significant. Sensible heat flux bears distinctive decadal variability between 14 and 16 years, and the main variability exhibits a dipole pattern with the maximum variability in the Labrador Sea and a secondary variability in Irminger Sea. The dipole pattern is mostly due to the variability of NAO. When the NAO is at its positive phase, the deepened Iceland low brings northwest wind with cold air over Labrador Sea and southwest wind with warm air over Irminger Sea. Therefore the sensible heat loss is enhanced in the first region but reduced in the other.

4.3 The Synthesis of the Maximum Lagged Correlation of the Coupled Simulation

Since the higher the lagged correlation, the tighter the connections we can infer among the variables, we perform the unprecedented synthesis of the maximum lagged correlation and the lag of the maximum lagged correlation in FOAM's control simulation. This synthesis is based on the leading PC of the complete list of 37 two- or three-dimensional principal variables. This synthesis provides us with two pieces of key information in terms of causality between each variable and AMOC: the maximum lagged correlation (MLC) between the leading PCs and the corresponding lag of MLC (LoMLC). MLC is the highest lagged correlation regardless of the sign of correlation. Fig. 8a-d is MLCs and LoMLCs between AMOC and the model variables from atmosphere, ocean, heat flux and freshwater flux, respectively. For atmospheric variables (Fig. 8a), the MLCs are about 0.5 (except meridional wind) when the atmospheric variables lead AMOC by 2 years (except specific humidity). This clearly

demonstrates that the decadal variability of atmospheric forcing excites that of AMOC. As to the oceanic variables (Fig. 8b), the MLCs are even more significant: vertical (W) and zonal current (U) have simultaneous correlations of more than 0.90; dynamic topography (P) and meridional current (V) lead AMOC by one year with MLCs around 0.85; salinity and density also lead AMOC by one year with MLCs around 0.55. Note that convections lead AMOC by one year with MLCs over 0.7, whereas ocean heat transport and ocean temperature lag AMOC by one year and two years, respectively. In Fig. 8c-d, the MLCs between heat/freshwater flux and AMOC help to elucidate the interactions between the atmosphere and ocean. Due to the fact that heat flux leads AMOC while freshwater flux lags AMOC, we conclude it is mainly through heat flux that the atmosphere drives AMOC. This is consistent with the results from Delworth et al. [2000]. Moreover, among different components of heat flux (Fig. 8c), we find that sensible heat flux dominates latent and radiation flux, as it is the only flux that leads AMOC.

Using AMOC as the benchmark, we have explicitly demonstrated the decadal variability of atmospheric variables leads the oceanic ones. If we use ice fraction (FRAC) as the benchmark instead, we can also demonstrate the second half of the cycle in the coupled air-sea interaction, namely, the response of atmospheric variables to oceanic forcing. Fig. 9a-d is MLCs and LoMLCs between FRAC and the model variables from atmosphere, ocean, heat flux and freshwater flux, respectively. First of all, we can use FRAC as the benchmark to confirm the lead-lag relationship obtained when AMOC is used as the benchmark. For example, the 2-year lead of AMOC and the zero lag of ocean temperature upon FRAC suggests AMOC leads the ocean

temperature by 2 years. Similarly, we can also confirm that meridional current (V) and density (D) lead AMOC by 1 year and HT lags AMOC by 1 year. These confirmations provide further support for the accuracy of the inferred causality among various physical processes.

In Fig. 9b, all of the ocean variables have a correlation of about 0.5 with FRAC. Most of the oceanic variables, AMOC in particular, lead FRAC by 2 years. As to the atmospheric variables (Fig. 9a), five out of 8 variables have a zero lag with FRAC. In addition, all of the strongest MLCs, i.e., those of geopotential height (Z2), atmospheric temperature (AT) and specific humidity (Q), have a zero lag with FRAC. Since oceanic variables lead FRAC by 2 year, whereas atmosphere covaries with FRAC, we can infer the oceanic variables also lead atmosphere variable by 2 years. Therefore the atmospheric variables do response to oceanic forcing. This response can be simply due to thermodynamic coupling through surface heat flux. In another word, the warm SST produces warm SAT. This conclusion will be further validated through sensitivity experiment D_ATM_R later. As to the cause of the decadal variability of FRAC, it has been shown that FRAC has a strong sensitivity to radiative flux, especially longwave radiation [Eisenman et al., 2007]. This sensitivity can also be found in CTRL, as Fig. 9c suggests that radiative flux, longwave radiation in particular, produces the bulk of the decadal variability for FRAC. Therefore, in terms of the sea ice melting/growing, the variability of atmospheric radiation is much more efficient than oceanic temperature. Actually, this can be readily seen from the fact that the MLC between FRAC and longwave radiation (~0.9) is much stronger than that between FRAC and ocean temperature (~0.6). Essentially, this demonstrates atmospheric response

provides a strong influence on the decadal variability of sea ice. In Fig. 9d, we found the sea ice melting/growing also produces the decadal variability of the ocean freshwater flux (QFLX). In summary, we conclude that the decadal variability of oceanic variables can lead that of the atmospheric variable by 2 years. Using AT and Z2 as the benchmark (not shown), we can show the ocean forces the atmosphere through sensible and latent heat flux. The atmospheric response to oceanic forcing can be simply due to thermodynamic coupling through surface heat flux. This is different from the mechanism of ocean's response to the atmosphere, which is through the atmospheric forcing on the convection sites in Labrador Sea and the ensuing adjustment of AMOC.

4.4 The Illustration of the Mechanism via Lagged Correlation Analysis

Combining Fig. 8 and Fig. 9, we illustrate in Fig. 10 that the coupled air-sea interaction is the emerging mechanism that governs the decadal variability of AMOC. At lag -2, colder SAT in Labrador Sea induces stronger sensible heat flux loss (Fig. 8c) that initiates stronger convections at lag -1. These stronger convections result in more North Atlantic Deep Water and produce the maximum AMOC at lag 0. In the mean time, due to the reduced longwave radiation and cold SST, the brine ejection from the growth of sea ice induces the salinity maximum between lag -1 and 0, and contributes the maximum of the AMOC as well. Associated with the increase of AMOC, ocean heat transport increases and maximizes at lag +1. The increased ocean heat transport helps to increase SST to its maximum at lag+2. And the increase of SST finally alters the sign of SAT through sensible and latent heat flux and therefore one

half cycle completes. If we use the lagged correlation curve of SST to estimate the period of oscillation, we have MLC at lag+2 and minimum lagged correlation at lag-3--therefore the half period is 6 years and total period 12 years, which is in good agreement with the 14-16 year estimate from the spectrum analysis (Fig. 1c2).

Note that there are two pieces of evidence to support the response of SAT to SST at lag+2 in Fig. 10: first, the persistence of SAT between lag+1 and lag+2 should result from the persistence of SST [Mosedale et al., 2006]; secondly, regarding the timing of the zero crossing of lagged correlation, SST leads SAT by 1 year. Furthermore, the timing of the zero crossing of the lagged correlation between SAT and AMOC as well as the symmetric shape of the lagged correlation along the positive and negative lags implies the variability of SAT has a 90^0 phase shift to that of AMOC. When we compare the lagged correlation curve with the autocorrelation curve of AMOC, the 90^0 phase shift is even more intriguing: when the curve of AMOC reaches zero-crossing from negative to positive at lag -3, SAT is near its minimum; when AMOC maximizes at lag 0, SAT reaches its own zero-crossing; and when AMOC reaches zero-crossing from positive to negative at lag 3, SAT is near its maximum. Hence we can schematically write down the governing equation for SAT and AMOC to illustrate their phase relationship:

$$\frac{dAMOC}{dt} = -k1 \times SAT \qquad 1a)$$

$$\frac{dSAT}{dt} = +k2 \times AMOC \qquad 1b)$$

Here $\sqrt{k1 \times k2} = \frac{2\pi}{T}$, where T is the decadal period of the system, namely, 12~16 years. Eq1a denotes the response of AMOC to SAT forcing. The physical processes

behind it involves the convections induced by the surface cooling of SAT and the density variability due to sea ice melting/growing, which is an indirect effect through SAT as well. Eq1b denotes the response of SAT to AMOC forcing, and the associated physical processes include the meridional heat transport, SST variability and thermodynamic coupling through sensible and latent heating. Eq1 implies the decadal variability of the AMOC in FOAM is the product of the air-sea interaction, with the time scale determined by the product of the response time of both AMOC to SAT and SAT to AMOC.

5 The Evaluation of the Mechanism via Sensitivity Experiments

5.1 Stochastic Run: the Discovery of the Damped Ocean Mode in FOAM

To examine whether decadal variability of AMOC relies on internal low frequency atmospheric forcing, we analyzed the 400-yr annual AMOC from DATM-STOC. In this simulation, the spectrum of the atmospheric forcing index shows the characteristics of white noise (Fig. 11a). The leading EOF of AMOC (not shown) is similar to the leading EOF from CTRL (Fig. 4b), which implies the convections in Labrador Sea are still producing the bulk of AMOC variability in DATM-STOC. Furthermore, the spectrum (Fig. 11b) of the leading PC of AMOC clearly indicates that the power spectrum has been enhanced around 10~20 years, and the spectral peak of 11~14 years is even significant above 95% confident level. A gain function (Fig. 11c), defined as the ratio of normalized AMOC spectrum to the normalized atmospheric forcing spectrum, provides another view of the enhancement of the response spectrum between 10 and 20 years. DATM-STOC provides clear evidence that the decadal variability of AMOC in CTRL does not originate from the internal low-frequency atmospheric variability [Delworth and Greatbatch, 2000]; furthermore, the enhanced decadal variability under stochastic forcing uncovers the damped ocean mode in FOAM. Note that the damped ocean mode is not contradictory to the proposed mechanism in the last section. Instead, it is the damped ocean mode that organizes the coupled atmosphere–ocean–sea ice interaction and selects 14~16 year as its preferred time scale.

Another characteristics of the damped ocean mode is the southward propagation of western boundary low frequency waves, as will be discussed in section 6. Here we just

show the EOF and spectrum of BSF from DATM-STOC. The 1st EOF of BSF (Fig. 12a) remains as a dipole pattern in the West Atlantic and the spike of the spectrum between 10 and 20 years is even more striking than that of AMOC. Note that the pronounced decadal peak exists without any surface forcing of significant decadal variability. Compared with coupled simulation, the main variability of sea ice fraction (Fig. 12b) has moved significantly northward and bears the spectrum of stochastic atmospheric forcing. Even though the 1st EOFs of sensible heat flux and convective frequency (Fig. 12c,d) stay roughly the same as that of CTRL, the spectra of them are essentially white. The evidence strongly suggests the 10~20-year intrinsic time scale of the damped ocean mode originates inside the ocean. However, the surface climate over North Atlantic Ocean fails to retain its decadal variability under stochastic atmospheric forcing. Compared with CTRL, the 1st EOFs of both SST and SSS (Fig. 13a,b) can not retain the monopole pattern in the subpolar gyre, and the spectra between 10 and 20 years are not significant, either. As to 3D ocean temperature and salinity (Fig. 13c,d), even though the 1st EOF of 3D salinity retains the dipole pattern at 300m in the North subpolar gyre as found in CTRL, the 1st EOF of 3D ocean temperature can not sustain its dipole pattern at 1000m. Furthermore, the stochastic surface damping also eliminates the 10~20-year decadal variability from both of them. In summary, even though the damped ocean mode provides the intrinsic time scale for the surface climate over North Atlantic Ocean, it can not prevent it from being damped by the stochastic atmospheric forcing. In other words, coupled ocean-atmosphere-sea ice interaction is necessary to sustain the observed decadal variability of the surface climate in the North Atlantic sector.

5.2 Switch-on Run: a Case Study on the Response of AMOC to NAO Forcing

To identify the physical processes involved in the damped ocean mode, especially to find out what processes set up the negative feedback and the associated 14~16 years time scale, we analyzed the 20-yr model output from DATM-SWITCH. Before we turn on NAO-like atmospheric forcing, AMOC is in its equilibrium state (Fig. 14a). This equilibrium state implies there is no active ocean mode in FOAM [Weaver and Valcke, 1998]. At year 1, the optimal atmospheric forcing pattern is turned on and kept constant. The sudden switch of atmospheric forcing induces strong convections in the Labrador Sea (not shown) and immediate increase of the AMOC. It takes two years from year 1 to year 3 for AMOC to reach its maximum. This confirms the result from CTRL that atmosphere leads AMOC by 2 years. Then AMOC starts to decrease and almost returns back to the equilibrium state at year 11. Therefore the half cycle of the damped ocean mode is 8 years from the maximum at year 3 to the minimum at year 11. This again confirms the results from both CTRL and DATM-STOC that the damped ocean mode has a time scale of 14~16 years. The negative feedback that brings AMOC back to the equilibrium state is the advection of salinity (Fig. 14b,c). At year 4 when AMOC starts the decreasing trend, there is substantial low salinity water existing in Irminger Sea. This low salinity water is not due to ice melting, because sea ice (not shown) has been more or less fixed due to the fixed atmospheric forcing. Instead, this low salinity water is due to the southward currents (Fig. 14b) that cross the salinity fronts (not shown) in this region. Then the low salinity anomaly is advected westward by East/West Greenland Current along the southern coast of Greenland from Irminger

Sea to Labrador Sea. By year 11, the freshening of the Labrador Sea eventually draws AMOC down to the equilibrium state (Fig. 14c). The southward current that produces the negative salinity in year 4 is caused by the negative dynamic topography as the water cools and sinks in the Labrador Sea. The details of the variability of the dynamic topography associated with AMOC will be discussed in section 6. In summary, experiment DATM-SWITCH provides a case study of the response of AMOC to the atmospheric forcing. It confirms the two-year response time of AMOC to atmospheric forcing and the 14~16-year intrinsic time scale of the damped ocean mode. It also identifies the anomalous advection and mean advection of salinity in the northern subpolar gyre as the negative feedback for the damped ocean mode.

5.3 Partial Blocking Run: the Necessity and Non-Necessity of Subpolar and Subtropical Dynamics of Sustaining the Damped Ocean Mode

Both data-atmosphere sensitivity simulations underscore the importance of the ocean dynamics: the damped ocean mode can be stochastically excited and it determines the time scale of the decadal variability in the North Atlantic. However, two types of ocean dynamics [Delworth et al., 1993; Grötzner et al., 1998] had been put forward to account for the decadal variability in the North Atlantic. D93 emphasized the subpolar ocean dynamics that the advection of salinity/temperature into the subpolar gyre induces the local density variability and AMOC variability. Grötzner et al. [1998] underscored the subtropical air-sea interaction that consists of a positive feedback between subtropical SST and local wind stress and a negative feedback between the subtropical gyre and remote wind stress. To further

verify the source region of decadal variability, two partial blocking experiments were used to alter either the subpolar or subtropical ocean dynamics to examine which ocean dynamics provides the necessary condition for the decadal variability in the North Atlantic.

In PBATL1535N (Fig. 15), the 5-degree wide "sponge wall" is placed at 40W between 15N and 35N (Fig. 15a). The subtropical ocean circulation of the North Atlantic has been transformed into a double-cell circulation, as can be seen from the 400-year average of barotropic stream function (Fig. 15a). However, with the altered subtropical ocean dynamics, both AMOC (not shown) and SST keep the leading EOF (Fig. 15b) and the power spectrum (Fig. 15c) of the leading PC the same as that in CTRL: the maximum variability of the SST is still at the subpolar region and the significant (>95%) spectral peak is still around 16 years. PBATL1535N provides clear evidence that the subtropical oceanic dynamics is not necessary to sustain the damped ocean mode, and the origin of the decadal variability of AMOC stays in the subpolar region. It is surprising to see the decadal variability of the surface climate in the North Atlantic remains intact after subtropical ocean dynamics is totally in ruins. But this surprise is just adding more confidence that the result from PBATL1535N is extremely robust. Actually, the success of PBATL1535N is due to the fact that the main ingredients of the damped ocean mode, such as the convections, sea ice and the atmospheric response to the damped ocean mode, are mainly in the subpolar region and intact in the experiment.

In PBATL3550N (Fig. 16), the 5-degree wide "sponge wall" is placed at 40W between 35N and 50N (Fig. 16b). Due to the change of the subpolar ocean circulation,

AMOC has been quickly shut down, as can be seen from the 400-year annual average of AMOC of 55N and 1700m depth (Fig. 16a). The negative value of AMOC indicates the Antarctic Bottom Water has extended northward and replaced the NADW in this region. With AMOC being eliminated, the interplay between SAT and AMOC has completely broken down (Eq1), so does the 14~16 year decadal variability of SST. Compared to the CTRL, the power spectrum of the leading PC of SST fails to maintain the 14~16 year decadal peak (Fig. 16c), and the center of the maximum loadings of the leading EOF (Fig. 16b) has moved from the middle to the east of the subpolar gyre, a straightforward outcome resulting from the blocking of westward propagation of Rossby waves. Therefore, the partial blocking of the subpolar gyre proves that the subpolar ocean dynamics, that of AMOC in particular, is necessary to sustain the decadal variability of surface climate in the North Atlantic in FOAM. However, in PBATL3550N, we do observe the 34~37-year multidecadal variability in SST (Fig. 16c), which is also discernible in the time series of the AMOC (Fig. 16a) and the power spectrum of the leading PC of AMOC (not shown). We suspect this multidecadal variability is associated with the variability of Antarctic Bottom Water as it penetrates further into the North Atlantic after the AMOC is shut off. However, further investigation is needed to address this issue.

5.4 Decadal AMIP Run: a Case Study on the Response of Atmosphere to Decadal SST Forcing

The response of ocean, AMOC in particular, to atmosphere forcing has been demonstrated in DATM-SWITCH, and here we use decadal atmosphere response run

(D_ATM_R) to demonstrate the response of atmosphere to decadal SST forcing. A decadal optimal SST forcing pattern is derived from lagged regression of SST in the subpolar region (-70W~0; 40N~65N) over AMOC. For lags between -3 and 2, even though the sign of the pattern slowly reverses (Fig. 10), the pattern of the lagged regression resembles the leading EOF of SST and exhibits a monopole in the subpolar region. We tripled the regression coefficients from lag -3 to +2 and use them for decadal optimal SST forcing pattern between year 1 and year 6. As a result, the magnitude of decadal optimal SST forcing pattern at the center of the subpolar region goes from -1.3 at year 1 to 2.2 at year 5 and drops to 1.7 at year 6 (Fig. 17). Then we reverse the sign of the first 6 years of decadal optimal SST forcing pattern and use them as another half of the decadal cycle of decadal optimal SST forcing pattern. And the magnitude of decadal optimal SST forcing pattern at the center of the subpolar region goes from 1.3 at year 7 to -2.2 at year 11 and increases to -1.7 at year 12. Then we reuse the first 8 years of the decadal optimal SST forcing pattern as the last 8 years of the 20-year decadal optimal SST forcing pattern. In this way, the constructed decadal optimal SST forcing pattern can provide the most realistic decadal SST forcing for atmosphere model. The difference between the response run and control run provides the ensemble of the atmosphere response to decadal optimal SST forcing pattern.

The leading EOF/PC of the ensemble response provides us the pattern/coefficient of the atmospheric response (Fig. 17 and Fig. 18). Here the coefficients are scaled to match the amplitude of the SST forcing and the corresponding EOFs are scaled back to conserve the magnitude of the response. The explained variances of the leading EOF

for SAT, surface pressure (PS), 250 mb and 500 mb geopotential height (Z250 and Z500), sensible (SHFLX) and latent (LHFLX) heat flux are 84%, 70%, 83%, 76%, 47% and 40%, respectively. The large explained variance indicates the signal-to-noise ratio from these ensemble experiments is high enough to distinguish atmospheric response from the background noise. All of the response coefficients (Fig. 17) closely follow the decadal variations of the SST forcing. The correlation between the SST forcing and the response coefficient ranges between 0.35 and 0.91, with SAT and LHFLX having the highest correlation and PS having the least. The high correlations between the response coefficients and SST forcing clearly demonstrate strong atmospheric response to the SST forcing. There are also high correlations among the response coefficients themselves. For instance, the correlations between the response coefficients and that of SAT range from 0.55 to 0.99, with SHFLX and LHFLX having the least and Z500 having the highest. Noticeably PS has a high correlation of 0.72 with SAT as well. In summary, the correlations between the response coefficients and SST forcing indicate the atmosphere can respond to SST forcing both dynamically and thermodynamically. The decadal response of PS to SST forcing suggests the decadal variability of NAO (Fig. 2b2) in FOAM is due to air-sea coupling. In fact, it is conceivable that thermodynamic response of SAT to SST forcing can result from the reduced thermal coupling [Barsugli and Battisti, 1998; Sura and Newman, 2008]: warmer SST provides more sensible and latent heating to the atmosphere and the atmosphere becomes warmer and moister. But it is worth pointing out that the dynamic response of PS, Z500/Z250 to SST forcing is not trivial since the dynamic field is under strong influence of the stochastic nature of the mid-latitude atmosphere.

Fig. 18 summarizes the patterns of atmospheric responses. The response of SAT (Fig. 18a) resembles the leading EOF of SAT (Fig. 1d1) of CTRL and has the maximum variability in the subpolar region. The response pattern of PS (Fig. 18b) is also reminiscent of the leading EOF of PS (Fig. 2b1), an NAO-like pattern with northern center of maximum variability sitting above Irminger Sea and the southern center of the maximum located above Azores. The warm/ridge response has an equivalent barotropic structure, as PS, Z500 and Z250 (Fig. 18b-d) all bare the similar NAO pattern. This finding is consistent with Rodwell et al. [1999], who found a barotropic cold/trough response in an atmosphere-alone model. Furthermore, both studies show the atmospheric warm/ridge (cold/trough) response should provide the positive feedback on SST through Ekman transport, but the sensible and latent heat flux (Fig. 18e,f) provides a negative feedback on SST.

As the response coefficients have the same amplitude of SST forcing, in the linear sense, the atmospheric response patterns provide the amplitude of atmosphere response to unit SST forcing. The maximum response amplitude for SAT, PS, Z500, Z250, SHFLX and LHFLX are 1.8 ^{o}C/K, 1.5 mb/K, 18m/K, 22m/K, 12W/m2/K and 8W/m2/K, respectively. The magnitude of the response of both PS and Z500 is at the lower end of the modeling studies, of which the reported atmospheric response ranges from 1.2 to 5 mb/K for PS and 20 to 40m/K for Z500 [Kushnir et al., 2002]. Therefore the variability of the damped ocean mode can be enhanced by an atmosphere that is only modestly sensitive to SST, and the decadal variability of AMOC is not an artifact of air-sea interaction resulted from excessive atmospheric response to SST forcing. In fact, the enhancement of the decadal variability of the damped mode in the coupled

simulation can result from reduced thermal coupling between SST and SAT. Even though SAT introduces a damping effect to reduce the amplitude of SST anomaly, the real role of the SAT is to change the convective activity in the Labrador Sea to reverse the decadal variability of AMOC. Since the damped ocean mode can not sustain itself, the increase of SST doesn't automatically guarantee the slowdown of the AMOC, therefore the damped ocean mode can only express itself through stochastic resonance in the stochastic run. However, with the help of the reduced thermal coupling, SAT can act as a trigger mechanism to systematically initiate the damped ocean mode, so that both of them form an active air-sea coupled mode as formulated mathematically in Eq1.

6 Discussions and Conclusion

We have demonstrated in section 3 that there are close relationships between the observed and simulated decadal variability of surface climate over the North Atlantic Ocean. Even though the period of SLP is shorter than that of SST in the observational study, the coupled atmosphere-ocean-sea ice interaction should still be valid since the thermodynamic response of SAT to SST should be quite robust. Another caveat for this study is the lack of the dynamic sea ice in the coupled simulation, which might have significant impact on the role of sea ice in the coupled interaction.

Here we adopt the approach of the data-model intercomparison to provide further evidence of the connections between the simulation and observations in terms of the decadal evolution of dynamic topography, ocean salinity and ocean temperature.

6.1 The Decadal Variability of the Dynamic Topography

The damped ocean mode is most easily tracked through the lagged regression map of oceanic dynamic topography upon AMOC (Fig. 19), where giant western boundary low frequency waves are seen propagating along the western basin of the Atlantic Ocean. Western boundary low frequency waves are the low frequency dynamic topography anomalies that propagate along the western boundary of the North Atlantic. It originates from Labrador Sea and takes 6 ~ 9 years to arrive at the southeast coast of the Unites States, where it decays. Even though it has been found in quite a few ocean modeling studies [Döscher et al., 1994; Gerdes and Köberle, 1995; Greatbatch and Peterson, 1996] and is attributed to either a first baroclinic mode of Kelvin wave or the topographic Rossby wave, the timescale of the propagation seems to be too long for

such a mechanism [Eden and Willebrand, 2001] and its dynamics still merits further investigation.

In CTRL, between lag -2 and lag -1, the trough of western boundary low frequency waves starts to form in the northern subpolar gyre. Then it expands and occupies the whole subpolar gyre by lag +1. From lag+2 to lag +3, the trough propagates from subpolar into subtropical gyre, and straddles the subpolar-subtropical boundaries by lag +3. What happens to the trough after lag +3 can be inferred from the propagation of the crest of western boundary low frequency waves at lag -2. The crest starts to elongate along the diagonal between Ireland and southeast US during lag -2 and lag -1. Then it decays and breaks up during lag 0 and lag +1 and propagates along the subtropical and subpolar route, respectively. From lag +2 to lag +3, the southern part of the crest continues the subtropic route and eventually decays near Bahamas; but the northern part of the crest takes the subpolar route and actually strengths and moves into Irminger Sea as the new seed of the western boundary low frequency waves. Except during the transition time between lag +1 and +2, the pattern of the western boundary low frequency waves resembles a bi-color 'comma', with the head as the trough/crest of western boundary low frequency waves in the subpolar gyre and the tail as the crest/trough along the gyre boundary. The 12-year period of the western boundary low frequency waves is consistent with the time scale of the damped ocean mode. It takes about 6 years for western boundary low frequency waves to propagate from subpolar gyre into subtropical gyre and another 6 years for the northern part of the western boundary low frequency waves to propagate back into the subpolar gyre to restart the cycle. For large-scale ocean circulations, the geostrophic balance guarantees that the

gradient of dynamic topography drives the ocean circulation variability. Therefore, along the passage of the western boundary low frequency waves, ocean circulation changes accordingly, with anti-clockwise circulation surrounding the troughs and clockwise circulation surrounding the crests. This can be readily seen from the streamlines that are derived from the lagged regression of the ocean currents upon AMOC. For example, at lag +3, there is northeastward current on the east side and southwest current on the west side of the trough, forming a large anti-clockwise circulation that almost occupies western half of the North Atlantic basin. As will be discussed in the next sections, these large-scale ocean circulation anomalies are also accompanied by the anomalous convergence of salt and heat flux that has a significant impact on ocean temperature and salinity.

The propagation of the western boundary low frequency waves on decadal time scale has also been captured by the observations and other modeling studies. D93 pointed out the critical role of the dynamic topography on the polarward transport of salt flux. Using Principle Oscillation Pattern analysis, Eden and Willebrand [2001] can identify a 15-year-period western boundary low frequency waves, excited by the convective events in Labrador Sea. In a hybrid-coupled simulation, Eden and Greatbatch [2003] identified a 15-year decadal variability in AMOC; furthermore, their regression of dynamic topography over AMOC index (their Fig. 8) is essentially the same as that in Fig. 14 in our study. Notably the seeds of western boundary low frequency waves in both studies reside in the Irminger Sea.

The vertical structure of the western boundary low frequency waves is essentially barotropic, as can be seen from the similar regression map at 200 m and 1000m (Fig.

20) during lag -1. And this barotropic structure of the circulation has also been observed on the Labrador continental slope [Häkkinen and Rhines, 2004]. Both the observations and the modeling study [Häkkinen and Rhines, 2004; Hatun et al., 2005] also confirm the 'comma' pattern as the leading EOF of the sea surface height (SSH), which bears strong decadal variability as well. Our result suggests the observed/simulated 'comma' pattern in the leading EOF of SSH actually results from the passage of western boundary low frequency waves (Fig. 5a1). Furthermore, the observations show that for the last 75 years pronounced decadal variations have been found in tidal data in the southeast US but not in the western European [Häkkinen, 2000]. This can be simply due to the fact that western boundary low frequency waves has little signal on the east coast of the North Atlantic. Regionally, observations show that the minimum/maximum mode of coupled slope water system (CSWS) [Pershing et al., 2001; Pickart et al., 1999] south of Newfoundland is closely related to the negative/positive phase of NAO. Basically this means during positive phase of NAO, the southwestward transport of the Labrador Sea Water (LSW) is reduced, whereas the hydrographic characteristics of LSW in the Deep Western Boundary Current are enhanced. This can be simply due to the geostrophic adjustment of the coastal water to the passage of the western boundary low frequency waves: the positive NAO produces more convection that results in the trough of the western boundary low frequency waves in the subpolar gyre (Fig. 19a). The trough of the western boundary low frequency waves induces anomalous northeast current along the continental shelf off Nova Scotia that reduces the southwestward transport of the Labrador Sea Water. On the other hand, the more convection in the Labrador basin generates the enhanced

hydrographic characteristics of LSW in the Deep Western Boundary Current.

The dynamics of the western boundary low frequency waves and its 12~16 time scale is closely related to the decadal variability of AMOC. Even though it is tempting to speculate the decadal variability of dynamic heights results from its response to the variability of wind stress forcing, DATM-SWITCH roughly provides the evidence that the propagation of western boundary low frequency waves can sustain itself without the influence of the varying wind stress (Fig. 21). One year after the positive NAO is switched on, the convection in the Labrador Sea develops and the western boundary low frequency wave emerges. The local convective cell produces western boundary low frequency waves, which can be seen from the dynamic topography dipole in the northwest North Atlantic, with the trough (crest) of western boundary low frequency waves in the downwelling (upwelling) region inside (outside) the Labrador Sea. For the next five years, the trough slowly moves out of the Labrador Sea, as it does in CTRL. And the southern part of the crest starts to strengthen and moves southward along the coast, and eventually it decays near Bahamas. At the same time, the northern part of the crest finds its way into Irminger Sea and strengthen itself substantially there during year three and four and eventually moves into Labrador Sea by year six. DATM-SWITCH roughly reproduces both the subtropical and the subpolar propagation route of western boundary low frequency waves, as found in the regression analysis of CTRL. Hence, western boundary low frequency waves found in the coupled control run and in the observation can mainly result from the ocean's dynamic response to the convective activity in the Labrador Sea. Eden and Greatbatch [2003] demonstrated the Rossby wave propagation is not responsible for the

determination of the 15-year time scale found in their hybrid simulation. Instead they attribute the time scale of the decadal oscillation to the advection of the deep west boundary currents. Here we show that the time scale is mainly controlled by the propagation of the western boundary low frequency wave along its subpolar route, and this argument is also consistent with the regression analysis of barotropic streamfunction in Eden and Greatbatch [2003] (their Fig. 8). But why is there a subpolar route for the western boundary low frequency waves in the first place? It turns out to be due to the propagation of the salinity anomaly in the subpolar gyre.

6.2 The Great Salinity Anomaly

The dynamic topography is modulated by the density distribution, which in turn is determined by the distribution of water salinity and temperature. As the dynamic topography is inversely proportional to density, high salinity or cold temperature results in low dynamic topography. Therefore the direct effect of salinity (temperature) results in negative (positive) correlation with dynamic topography. Furthermore, due to the nonlinearity of the equation of state, salinity has a greater effect on the density of water than temperature does when the temperature of seawater is near freezing point. Fig. 22 shows the map of local correlation between dynamic topography and salinity or temperature. In the subpolar region, salinity's effect on the dynamic topography is dominant. The absolute correlation between salinity and dynamic topography is over 0.5 in most of the subpolar region. In Irminger Sea, the correlation is even over 0.8. In contrast, the temperature exhibits indirect effect and is mainly confined in the Labrador Sea. However, in the subtropics, the salinity's effect is diminishing and the dynamic

topography is dominated by the temperature. For example, the correlation is over 0.7 in the western subtropical Atlantic. Therefore, the southward propagation route of western boundary low frequency waves results from the interaction between dynamic topography and temperature and the subpolar route of western boundary low frequency waves results from its interaction with salinity.

In fact, the salinity in the subpolar gyre does propagate along the subpolar route of western boundary low frequency waves, as can be seen from the lagged regression map of salinity over AMOC (Fig. 23) in CTRL. Between lag -2 and lag -1, the saline water in the northern subpolar gyre increases the density in the upper ocean and excites convections in the Labrador Sea. As can be inferred from the overlaid streamline, the convective cell produces the trough of western boundary low frequency waves in the Labrador Sea and northern subpolar gyre as well as the crest of western boundary low frequency waves in the southern subpolar gyre and western subtropical gyre. On the southeastern subpolar gyre, the crest of the western boundary low frequency waves induces southward flows that result in fresher water (Fig. 23a,b). This freshwater is then advected northeastward via the North Atlantic Current and reaches Irminger Sea by lag +3 (Fig. 23c-f), where strong salinity front between Arctic water and the North Atlantic water resides. On one hand, the low salinity in Irminger Sea intensifies because it induces positive dynamic topography and strong clockwise flows to draw freshwater southward near the salinity fronts (Fig. 23g,h). On the other hand, with the help of the atmospheric positive feedback, the warming of the subpolar gyre induces vast sea ice melting and produces extremely low salinity in Irminger Sea as well. By lag +5, the saline water in the northern subpolar gyre during lag -1 has been replaced

by the freshwater and then the other half of the cycle continues. Note that the propagation route in CTRL is consistent with evolution of salinity anomaly in DATM-SWITCH (Fig. 14) and this confirms that negative feedback of the propagation of salinity anomaly along the subpolar gyre is a robust feature of the damped ocean mode and this propagation can exist without varying atmospheric forcing.

The intensification of the salinity anomaly in the Irminger Sea is closely related to ice melting/growing (Fig. 24). During lag -2 and -1 when the air temperature is at the minimum (Fig. 10), sea ice grows in the northern subpolar gyre, especially in the Irminger Sea (Fig. 24a,b). The brine ejection from the growing sea ice produces the corresponding positive salinity anomaly (Fig. 23a,b & Fig. 10) in the northern subpolar gyre. Between lag +1 and +3, when the positive SST anomalies prevails in the subpolar gyre (Fig. 10), the sea ice melting in the northern subpolar gyre (Fig. 24d-f) dumps freshwater into Irminger Sea and the positive salinity anomaly starts diminishing at lag +1 and is replaced by negative salinity anomaly at lag+3. The effect of sea ice on the salinity can be mixed down to great depth via turbulent and convective mixing.

The 30m subsurface salinity budget analysis (Fig. 25&26) is used to further elucidate the mechanism of the salinity variability in the subpolar gyre. The map of lagged correlation of the each salinity tendency term upon the index of AMOC is used to illustrate the various terms of the salinity budget and the salinity dynamics among different regions in the subpolar gyre. At lag -1 (Fig. 25a,b), the positive salinity anomaly in the Irminger Sea is mainly caused by convective mixing resulted from brine ejection/ice melting. The positive salinity anomaly also induces negative

dynamic height and anomalous northward circulation that brings saltier water from south into Irminger Sea, so that the anomalous circulation also contributes to the positive salinity anomaly (Fig. 25c). At the mean time, the mean circulation in the northern subpolar gyre transports the ensuing salty water eastward into the Labrador Sea (Fig. 25d). Along the North Atlantic Current, the Ekman pumping excites anomalous vertical advection and produces negative salinity anomaly. The effects of convective mixing, mean zonal advection contribute to the salinity variability in this region as well. To shed the light on the mechanism of the propagation of the salinity anomaly and to quantify the relative contribution of each tendency term, the lagged correlation curves of the tendency terms from four regions along the track of the propagation is depicted in Fig. 26. In Irminger Sea, as discussed earlier, the top three contributors are convective mixing, anomalous meridional circulation transport and mean zonal advection (Fig. 26a). The lag between the circulation variability and convective mixing is due to the fact that the salinity anomaly induced by the convective mixing excites the circulation anomaly, so that even though the sea ice started to retreat (Fig. 24a,b) at lag0, the anomaly northward advection still brings saltier water into the Irminger sea to keep the positive salinity anomaly intensify. In Labrador Sea, the effect of convective mixing is dominating (Fig. 26b). Along the North Atlantic Current, both Ekman pumping and convective mixing are responsible for the salinity tendency, whereas the mean advection damps the salinity anomaly (Fig. 26c).

In summary, the salt budget analysis underscores the important role of the sea ice in coupled ocean-atmosphere-sea ice interaction. In the northern subpolar gyre, brine

ejection/ice melting are the main contributor of the salinity tendency, which is further amplified via the anomalous meridional circulation; along the North Atlantic Current, both Ekman pumping and convective mixing are responsible for the salinity tendency. In both regions, the mean zonal circulation advects the ensuing anomaly around the subpolar gyre (Fig. 25d). The propagation of the salinity anomaly around subpolar gyre in FOAM simulation is quite similar to the observed Great Salinity Anomaly (GSA) during 70s, 80s and 90s [Belkin et al., 1998; Belkin, 2004; Dickson et al., 1988]. These GSA events formed either in GIN (Greenland-Iceland-Norwegian) Sea or in Labrador Sea and involved strong decadal scale salinity, temperature and sea ice variability. Recent OGCM studies [Zhang and Vallis, 2006] have shown that GSA can significantly weaken AMOC and induce SST variability. With only thermodynamic sea ice algorithm, FOAM cannot simulate the export of the sea ice from Arctic into the North Atlantic. But the impact of sea ice production/melting on the salinity and the ensuing effect on decadal variability of AMOC is very well captured in this coupled climate simulation. The similarity between the modeled and observed GSA events suggests the mechanism of coupled ocean-atmosphere-sea ice interaction found in FOAM has its implication on the observed decadal variability in the North Atlantic.

6.3 The Decadal Variability of the Sea Surface Temperature

The simulated decadal variability of the North Atlantic SST in FOAM captures the characteristics of both EOF and spectra from the observation and is proved to be caused by the decadal variability of AMOC. In this section, we will analyze the lagged

regression map of ocean temperature and the corresponding heat budget to shed more lights on the dynamics of subpolar SST.

Bjerknes introduced the concept of time scale dependence in the air-sea interaction [Bjerknes, 1964]: on the interannual time scale, Atlantic SST is mostly influenced by the surface heat flux, but on the decadal or longer time, the influence of the heat transport through ocean circulation becomes more and more important. Even though the contribution of subtropical gyre variability, as he conjectured in his seminal paper, is dwarfed by the subpolar gyre and AMOC variability, it is still illuminating to apply the lagged correlation map analysis (Fig. 27) to identify how the ocean circulation variability, especially that induced by western boundary low frequency waves, produced the decadal ocean temperature variability. Between lag -2 and -1, when the crest of western boundary low frequency waves has moved out of the Labrador Sea, it induces cold (warm) temperature anomaly in central subpolar gyre (off east coast of North America) by southward (westward and northward) anomalous advection. There is also another center of cold (warm) temperature anomaly in tropical (northeastern) North Atlantic that is presumably due to surface heat flux and thermocline variability. The anomalous temperatures exhibit a quadrapole pattern in the North Atlantic before AMOC maximizes at lag 0. Lag 0 marks the transition time between the crest and trough regimes of western boundary low frequency waves. When the crest of western boundary low frequency waves starts diminishing and the trough begins to move out of Labrador Sea to occupy the western North Atlantic (Fig. 19). The interesting feature of this transition time is the connection of the western side

of the crest and the eastern side of the trough, such that the northward anomalous advections in both sides produce the warm temperature anomaly along the western North Atlantic from Florida all the way to Iceland (Fig. 27c). This transition also marks the transition of the phase of quadrapole, as all the temperature anomalies of the quadrapole reverse during lag +1 and +2. During lag +3 (Fig. 27d), the warm temperature anomalies seemingly start to connect with each other. If we compare lag 0 and lag +3, the subsurface temperatures exhibit a clockwise rotation from north-south dipole during lag 0 to the east-west dipole during lag +3. A similar rotation of subsurface temperature has also been documented in coupled atmosphere–ocean–sea ice model (ECBILT) [Selten et al., 1999]. Apparently the rotation of temperature is caused by the passage of the western boundary low frequency waves along West North Atlantic, hence this rotation is not the rotation caused by the mean advection, as conceived by intuition, but by heat transports due to local circulation variability. The lagged correlation map analysis provides the vivid illustration how the decadal variability of AMOC induces the decadal variability of subpolar temperature through the heat transport associated with the passage of the western boundary low frequency waves.

Heat budget analysis is taken to further elucidate the mechanism that produces the decadal variability of the near-surface ocean temperature. When the SST anomaly peaks at lag +2 (Fig. 28a), the central subpolar near-surface temperature is mainly caused by anomalous meridional heat transport and convective heating (Fig. 28b,c). The anomalous meridional heat transport mimics the shape of western boundary low frequency waves and proves explicitly the importance of the circulation variability in

producing ocean temperature variability. Thermocline variability (Fig. 28d) is also contributing to the temperature quadrapole, especially to the two centers on the eastern North Atlantic, where the effect from anomalous meridional heat transport and convective heating is minimal. The convective heating in the subpolar gyre is actually due to the reduction of sea ice melting after the margin of the sea ice retreated (Fig. 24e). This can be seen from the surface heat budget analysis (Fig. 29). At lag +2, surface heat flux is into the ocean (Fig. 29a) and this is mainly caused by the reduction of the heat flux used to melt the sea ice (Fig. 29b). The effects from net longwave and shortwave radiation (Fig. 29c,d) mostly cancel each other due to the response from cloud and the increase of sensible and latent heating due to the water exposure is still dwarfed by the reduction of the ice melting. The area-averaged heat budgets of the four centers (Fig. 28a) of quadrapole are summarized in Fig. 30. In central subpolar gyre (Fig. 30a), both anomalous meridional heat transport and surface heating produces the temperature maximum at lag +2. The meridional heat transport maximizes at lag 0 and +1, and part of the heat is used to melt the sea ice, so that the surface heating due to the reduction of the ice melting takes effect at lag +2 and +3. The damping effect of sea ice during lag 0 and lag +1 on the heating from meridional heat transport might explain the 2-year delay of the SST warming after AMOC peaks at lag 0. In the central west of the North Atlantic (Fig. 30b), the effect of the reduction of the meridional heat transport is dominating. In both southeast and northeast of the North Atlantic, the effect of thermocline variability and meridional heat transport dominates convective heating (Fig. 30c,d). In summary, the central subpolar temperature variability is caused by the western boundary low frequency waves-induced meridional circulation

variability and it is further enhanced by the reduction of the surface heating due to sea ice melting. The effect of anomalous circulation on the temperature is mostly along the passage of western boundary low frequency waves in west North Atlantic; in the eastern North Atlantic, the variability of thermocline variability prevails.

It is intriguing to compare the evolution of the quadrapole pattern from control simulation of FOAM with that from HadISST (1870 ~2007) [Rayner et al., 2003]. Since there is no index of AMOC from observation, we use the area-averaged SST (Fig. 31a) as the proxy for the strength of AMOC. The map of the simultaneous correlation (Fig. 31a) between HadISST SST and the AMOC proxy exhibits a similar quadrapole pattern as that from control simulation, with the northeast North Atlantic center becomes substantially weaker. Connecting the middle point of the rest three centers, we obtain a track along which the lagged correlation between SST and AMOC proxy can be plotted in the Hovmoller diagram (Fig. 31b). The three centers of the quadrapole is clearly identified at lag 0 of the Hovmoller diagram and persists for about two year in both lead and lag. But the asymmetry arises when we compare the anti-phase signature of the quadrapole between lag +4 and lag -4. There is some antiphase correlation during lag -4, but none of them are found during lag+4. The antiphase correlation during lag -4 implies there is 16-year decadal variability in the North Atlantic SST from HadISST, and the asymmetry between lag-4 and lag +4 implies the subpolar SST is more connected to the northward propagation anomaly from central west of the North Atlantic than its impact on the rest of the SST along the track. A similar feature is also observed from the same analysis using SST from control simulation (Fig. 31c). Owing to the 400-year longer data, the antiphase

correlation at lag-4 is more significant than that from HadISST. The northward propagation can be more easily observed after the subsurface data is used (Fig. 31d). The central west subtropical centers at both lag -4 and 0 propagate northward and reach the central subpolar center after 4 years. As discussed earlier, the northward propagation is the result of the passage of western boundary low frequency waves. Especially during the transition phase of the western boundary low frequency waves regime at lag 0, the SST variability in both subpolar center and the western subtropical center is connected along the track (Fig. 27c). On the other hand, the impact of subpolar SST during positive lags on the rest of SST is mostly through atmosphere response, which has a much weaker signal-to-noise ratio than the pure oceanic connection via western boundary low frequency waves. This explains the asymmetry found in both simulated and observed lagged correlation Hovmoller diagram. In summary, using the lagged correlation Hovmoller diagram, we found a 4-year lag antiphase correlation in SST from both control simulation and HadISST. This antiphase correlation is caused by the passage of the western boundary low frequency waves, through which the induced anomalous heat transport warms both the central western North Atlantic and the central subpolar ocean. The asymmetry between positive and negative lags from the Hovmoller diagram is due to the fact that the impact of subpolar SST through atmosphere response has a much smaller signal-to-noise ratio than that of the oceanic processes, such as the induced temperature anomaly by anomalous heat transport via the passage of western boundary low frequency waves. Again, the similarity between the modeled and observed lagged-correlation Hovmoller diagram suggests the mechanism of coupled ocean-atmosphere-sea ice

interaction found in FOAM has its implication on the observed decadal variability in the North Atlantic.

6.4 The Relevance of This Mechanism to the Earlier Investigations

Based on coupled and data-atmosphere simulation, we validated a novel mechanism for the 14~16-year decadal variability of AMOC in FOAM. We uncovered a damped ocean mode in data-atmosphere simulations. The intrinsic decadal time scale is determined by the sum of the response time of AMOC to atmospheric forcing and the advection time of salinity anomaly from the Irminger Sea to the Labrador Sea. Furthermore, after the stochastic atmosphere model is replaced by fully coupled atmosphere model, the damped ocean mode organizes an energetic decadal coupled atmosphere–ocean–sea ice interaction in the North Atlantic and produces far more distinctive decadal variability in AMOC. In fact, in the coupled simulation, the atmospheric response to the subpolar SST substantially enhances the variability of the damped ocean mode on decadal time scales. On one hand, when the subpolar SST is warmer, the warm-ridge dynamic response of the atmosphere provides the positive feedback by inducing northward Ekman transport to further increase the warming of SST, on the other hand, the local SAT-convection feedback and the remote sea ice-convection feedback act jointly to provide the delayed negative feedback in the coupled ocean-atmosphere-sea ice interaction.

There are ample connections of this work to the earlier studies. Consistent with earlier coupled model studies [Delworth and Greatbatch, 2000; Weaver and Valcke,

1998], the decadal variability of AMOC does not come from a self-sustained active ocean-alone mode [Greatbatch and Zhang, 1995]. The role of sea ice in coupled ocean-atmosphere-sea ice interaction is similar to the study by Yang and Neelin [1993], except that they found a self-sustained active mode in the zonally averaged AMOC model coupled to the thermodynamic sea ice model. The nature of damped mode in the uncoupled simulation agrees with the box model study by Griffies and Tziperman [1995], but our study differs from theirs with respect to the role of ocean temperature in the damped mode. In Griffies and Tziperman [1995], the ocean temperature provides the direct negative feedback to AMOC by the reduction of the water density. In our study, in addition to the direct negative feedback on the water density, the far more important role of the ocean temperature is to provide the indirect negative feedback to AMOC through atmospheric response and ice melting, since the effect of ocean salinity is more critical than ocean temperature on the water density in the subpolar ocean (Fig. 22). Note that D93 found another indirect negative feedback from ocean temperature, by which the meridional AMOC is coupled with the horizontal circulation in the middle of the North Atlantic. A similar coupling between the meridional and horizontal circulation is also observed in this study, but the horizontal circulation is induced by western boundary low frequency waves, which itself is excited through ocean salinity instead of ocean temperature. The distinction between this study and Delworth and Greatbatch [2000] is on the origin of the low frequency variability of the atmosphere: we demonstrated in D_ATM_R that the response of atmosphere to decadal variability of subpolar SST produces the low frequency variability in the atmosphere, as opposed to Delworth and Greatbatch [2000], who

attributed the low frequency variability of atmosphere to the internal variability of the atmosphere as found in James and James [1989]. It is this distinction that defines the mechanism found in the coupled simulation as coupled atmosphere-ocean-sea ice interaction organized by the damped ocean mode. This novel mechanism has not been documented by other coupled climate models, however, Eden and Greatbatch [2003] reported a coupled air-sea interaction organized by a damped ocean mode in their hybrid climate models. Furthermore, they reached the same conclusion that the positive feedback in the decadal cycle is the process to distinguish the coupled air-sea interaction from the damped oscillation in an ocean alone model. Dong and Sutton [2005] also reported the important role of the stochastic atmospheric forcing on convective activities and attribute it as preconditions for the decadal variability of AMOC in HadCM3. Even though the atmospheric dynamic response to mid-latitude SST varies broadly across the climate models [Kushnir et al., 2002], thermodynamic response between SAT and SST should be robust. Without the atmospheric response, even though both AMOC and BSF exhibit significant decadal variability, the damped ocean mode fails producing the decadal variability of SST. Therefore, we do regard the coupled atmosphere-ocean-sea ice interaction organized by the damped ocean mode as one of the plausible mechanisms to explain the decadal variability of the surface climate over the North Atlantic sector.

7 Figure and Table Captions

Fig. 1. Leading EOFs and power spectra of the leading PCs from HadISST SST (a1,a2), ICOADS SAT (b1,b2), FOAM CTRL SST (c1,c2) and FOAM CTRL SAT (d1,d2). The contour intervals of the normalized EOFs are 0.10 and the units of the power spectra are ($^oC^2$*year). Theoretical Markov spectrum and the 0.05/0.95 lower and upper confidence curves are also plotted. The vertical lines delineate the power spectra of the periods between 10 years and 20 years. All the EOFs and power spectra are calculated using NCL (NCAR Command Language).

Fig. 2. (a1,a2), as Fig. 1 (a1,a2), but for HadSLP2 SLP. (b1,b2), as Fig. 1 (c1,c2), but for FOAM CTRL SLP. The contour intervals of the normalized EOFs are 0.20.

Fig. 3. Climatology of FOAM control simulation (CTRL) in the North Atlantic based on 400 year annual data output : a) barotropic stream function (Sv) b) standard deviation of convective frequency (counts/month) c) sea surface temperature (^oC) d) sea surface salinity (psu). The contour intervals (ci) are a) 5 Sv, b) 200 counts/month, c) 2 ^oC, d) 1 psu.

Fig. 4. (a) Climatology (ci: 2 Sv), (b) leading EOF (normalized) and (c) power spectrum (Sv^2*year) of the leading PC of AMOC from 400-year annual model output of FOAM's control simulation. Theoretical Markov spectrum and the 0.05/0.95 lower

and upper confidence curves are also plotted. The vertical lines delineate the power spectra of the periods between 10 years and 20 years.

Fig. 5. As in Fig. 2, but for barotropical streamfunction (BSF, a1,a2), sea ice fraction (b1,b2), sea surface salinity (c1,c2) and convective frequency (d1,d2).

Fig. 6. As in Fig. 2, but for 3D ocean temperature at 1000 m depth (a1,a2), 3D ocean salinity at 300 m depth (b1,b2), 3D air temperature on the surface (c1,c2), and 3D specific humidity on the surface (d1,d2).

Fig. 7. As in Fig. 2, but for sensible heat flux (a1,a2), latent heat flux (b1,b2), longwave radiation flux (c1,c2) and shortwave radiation flux (d1,d2).

Fig. 8. The maximum lagged correlations (MLC) and the corresponding lag of MLC (LoMLC) between PC1 of AMOC and PC1 of (a) Atmospheric, (b) oceanic, (c) radiative and (d) freshwater variables. Atmospheric variables include 3D geopotential heights (Z2), 3D zonal wind (AU), 3D meridional wind (AV), 3D vertical motion (OMEGA), 3D air temperature (AT), 3D specific humidity (Q) and surface pressure (PS). Oceanic variables include Atlantic Meridional overturning circulation (MOC), barotropic streamfunction (BSF), 3D vertical current (W), 3D dynamic topography (P), 3D zonal currents (U), 3D meridional currents (V), 3D density (D), 3D salinity (S), 3D ocean temperature (T), convections (CONVEC) and heat transport (HT). Radiative variables include heat flux into the ocean (OHEAT), short wave radiation (RAD), long

wave radiation (LWV), sensible heat flux (SHF), latent heat flux (LHF), low cloud (CLDLOW), median cloud (CLDMED), high cloud (CLDHGH) and total cloud (CLDTOT). Freshwater variables include freshwater flux into the ocean (OQFLX), evaporation (EVP), large scale precipitation (PRECL), convective precipitation (PRECC), precipitation from atmosphere (OPREC), sea ice thickness (THCK), sea ice fraction (FRAC), melting potential (METLP), surface ice temperature (ICET1). The maximum lagged correlation (thin black bars) and the associated lag (thick red/blue bars) are scaled by the right and left axis, respectively. Only the absolute value of MLC is plotted.

Fig. 9. Same as Fig. 5, but using PC1 of sea ice fraction (FRAC) as the index.

Fig. 10. Annually lagged correlation between the leading PC of AMOC and the leading PC of SAT (blue), convections (light blue), SST(purple), heat transport (black), 3D ocean temperature (green), SST (Red), AMOC (black dash), ice fraction (black dot).

Fig. 11. (a) Power spectrum (1^2*year) of the atmospheric forcing index in DATM-STOC simulation. (b) as (a), but for the power spectrum (Sv^2*year) of leading PC of AMOC . (c) gain function for DATM-STOC simulation. The ratio between the normalized spectra of (b) and (a) is plotted as the gain function. Theoretical Markov spectrum and the 0.05/0.95 lower and upper confidence curves are also plotted. The vertical lines delineate the power spectra of the periods between 10 years and 20 years.

Fig. 12. As in Fig. 2, but for DATM-STOC. (a1,a2), BSF; (b1,b2), sea ice fraction; (c1,c2), sensible heat flux; (d1,d2), convective frequency.

Fig. 13. As in Fig. 12, but for SST (a1,a2), SSS (b1,b2), 3D ocean temperature at 1000 m depth (c1,c2), 3D ocean salinity at 300 m depth (d1,d2).

Fig. 14. (a) AMOC intensity (Sv) and SAT anomaly (^{o}C) in DATM-SWITCH simulation. The positive NAO forcing is switched on at year zero. AMOC intensity is defined as the annual mean value of the streamfunction at 55N and 1700 m. SAT anomaly is plotted using the annual mean SAT anomaly at southern tip of Greenland (40W,60N). The letter "b" and "c" delineate the state of AMOC during which the Figure (b) and (c) is plotted, respectively. (b) The anomaly of salinity (psu; ci: 0.06), zonal (m/s) and meridional current (m/s) at 50m depth four years after the positive NAO forcing is switched-on. The current vector is omitted when either zonal current or meridional current is less than 1e-4 m/s. (c) as (b), but at 300 m and 11 years after the positive NAO forcing is switched-on.

Fig. 15. (a) Climatology of barotropic streamfunction (Sv), (b) the leading EOF (normalized) and (c) the power spectrum ($^{o}C^{2}$*year) of the leading PC of SST based on 400 year annual data from experiment PBATL1335N. The solid bar in (a) denotes the position of the "sponge wall". The contour intervals in (a) are 5 Sv for negative BSF, 10 Sv for BSF smaller than 60 and 60 Sv for BSF larger than 60. Theoretical Markov spectrum and the 0.05/0.95 lower and upper confidence curves are also plotted. The

vertical lines delineate the power spectra of the periods between 10 years and 20 years.

Fig. 16. (a) Time series of AMOC (Sv) at (55N, 1700 m), (b) the leading EOF (normalized) and (c) the power spectrum ($^oC^2$*year) of the leading PC of SST based on 400 year annual data from experiment PBATL3550N. The solid bar in (b) denotes the position of the "sponge wall". Theoretical Markov spectrum and the 0.05/0.95 lower and upper confidence curves are also plotted. The vertical lines delineate the power spectra of the periods between 10 years and 20 years.

Fig. 17. The atmospheric response coefficient in experiment D_ATM_R. The 20-member ensemble of the difference of the various quantities in each twin experiment are analyzed using EOF technique. The derived leading EOF/PC are the atmospheric response patterns/coefficients for various quantities. The PCs are scaled by multiplying the ratio of minimum anomalous SST forcing at southern tip of Greenland (40W,55N) and the minimum of PCs, and the EOFs are scaled back by dividing the corresponding ratio. The atmospheric response coefficient of various quantities are SAT (black), Z500 (red), PS (green), latent heat flux (blue), sensible heat flux (light blue) and Z250 (purple). The SST forcing at Greenland (40W,55N) is also plotted in black dash. The correlation between the SST forcing and the response coefficient of various quantities are 0.81 (SAT), 0.35(PS), 0.76 (Z500), 0.72 (Z250), 0.71 (SHFLX) and 0.91 (LHFLX). The correlation between the response coefficient of SAT and that of other various quantities are 0.72 (PS), 0.99(Z500), 0.97 (Z250), 0.72 (Z250), 0.55 (SHFLX) and 0.66 (LHFLX).

Fig. 18. The atmospheric response pattern: a) SAT (ci: 0.3 ^{o}C/^{o}C), b) PS (ci: 0.3 mb/^{o}C), c) Z500 (ci: 2 m/^{o}C), d) Z250 (ci: 2 m/^{o}C), e) SHFLX (ci: 2 W/m^{2}/^{o}C), f) LHFLX(ci: 2 W/m^{2}/^{o}C).

Fig. 19. The map of the lagged regression of 30m dynamic topography and the horizontal streamline upon the leading PC of AMOC in FOAM's control simulation. The contour intervals are 0.02 m^{2}/s^{2}/Sv for values between -0.2 and 0.2 and 0.4 m^{2}/s^{2}/Sv for values between -1 and -0.2 and between 0.2 and 1. The data are omitted for values weaker than 1/30 of the strongest lagged regression coefficients. The negative/positive lag indicates dynamic topography and the streamline is leading/lagging the 1st PC of AMOC.

Fig. 20. Same as Fig. 14., but at a) 200 m and b) 1000 m during lag -1.

Fig. 21. 30m dynamic topography and the horizontal streamline anomaly in experiment DATM-SWITCH. The contour intervals are 0.02 m^{2}/s^{2}. The data are omitted for values weaker than 1/30 of the strongest anomaly.

Fig. 22. Pointwise correlation between dynamic topography and a) salinity and b) temperature at 30m depth in FOAM's control simulation.

Fig. 23. Same as Fig. 14, but for salinity. The contour intervals are 0.05 psu/Sv for

values between -0.20 and 0.20 and 0.15 psu/Sv for values between -0.35 and -0.20 and between 0.20 and 0.35. The data are omitted for values weaker than 1/10 of the strongest lagged regression coefficients.

Fig. 24. Same as Fig. 14., but for sea ice fraction and without horizontal streamline. The contour intervals are 0.01 Sv^{-1} for values between -0.05 and 0.05 and 0.05 Sv^{-1} for values between -0.10 and -0.05 and between 0.05 and 0.10.

Fig. 25. The map of lagged regression of a) salinity and b)-e) various salinity tendency terms upon the leading PC of AMOC in FOAM's control simulation at 30m depth during lag -1. The various tendency terms are b) convective mixing, c) anomalous meridional transport, d) mean zonal transport, e) anomalous vertical transport. The contour intervals are a) 0.05 psu/Sv and b)-e) 0.04 psu/year/Sv. The boxes in a) denotes the detailed location of Irminger Sea (IS), Labrador Sea (LS) and the North Atlantic Current (NAC) in Fig. 26.

Fig. 26. Area-averaged lagged regression coefficient (RC, psu/year/Sv) from a) Irminger Sea, b) Labrador Sea and c) the North Atlantic Current between various tendency terms and the leading PC of the AMOC. The various tendency terms are anomalous/mean zonal transport (black/blue), anomalous/mean meridional transport (red/light blue), anomalous/mean vertical transport (green/purple), and vertical mixing (black dot). The detailed location for the three regions is labeled in Fig. 25a.

Fig. 27. Same as Fig. 19, but for temperature. The contour intervals are 0.025 ^{o}C/Sv for values between -0.15 and 0.15 and 0.45 ^{o}C/Sv for values between -0.75 and -0.40 and between 0.40 and 0.75. The data are omitted for values weaker than 1/15 of the strongest lagged regression coefficients.

Fig. 28. The map of lagged regression of a) ocean temperature and b)-d) various temperature tendency terms upon the leading PC of AMOC in FOAM's control simulation at 30m depth during lag +2. The various tendency terms are b) anomalous meridional transport, c) convective mixing, d) anomalous vertical transport. The contour intervals are a) 0.05 ^{o}C/Sv and b)-d) 0.01 ^{o}C/year/Sv. The boxes in a) denotes the detailed location of Central Subpolar Gyre (CSG), Central West North Atlantic (CWNA), southeast North Atlantic (SENA) and Northeast North Atlantic (NENA) in Fig. 30.

Fig. 29. The map of lagged regression of surface heat flux (^{o}C/year/Sv, positive into the ocean) upon the leading PC of AMOC in FOAM's control simulation at lag +2. a) total surface heat flux, b) surface heat flux due to ice melting, c) net short wave radiative flux, d) net long wave radiative flux, e) sensible heat flux, f) latent heat flux. The contour intervals are a)-b) 3 ^{o}C/year/Sv and c)-f) 0.5 ^{o}C/year/Sv.

Fig. 30. Area-averaged lagged regression coefficient (RC, ^{o}C/year/Sv) from a) Central Subpolar Gyre, b) Central West North Atlantic, c) southeast North Atlantic and d)

Northeast North Atlantic between various tendency terms and the leading PC of the AMOC. The various tendency terms are anomalous/mean zonal transport (black/blue), anomalous/mean meridional transport (red/light blue), anomalous/mean vertical transport (green/purple), and vertical mixing (black dot). The detailed location for the three regions is labeled in Fig. 28a.

Fig. 31. a) The map of simultaneous correlation of winter (DJF) HadISST SST upon the area-averaged winter SST in the subpolar region (black box). The contour interval is 0.2. The black dot lines are the track along which the lagged correlation Hovmoller diagram is drawn in b)-d). b) Along track lagged correlation Hovmoller diagram for HadISST SST. Negative lags mean the SST along the track is leading the subpolar SST. The vertical line in the middle separates the southern track from the northern track. The contour interval is 0.1 and the correlation smaller than 0.13 is not drawn. c) Same as b), but for FOAM control simulation. d) Same as c), but for ocean temperature at 50m.

Table 1 Experiments performed in this study

Simulation name	Configuration	Run length (yrs)	Memo
CTRL	Control	400	
DATM-STOC	Stochastic run/data atmosphere	400	Atmospheric forcing is stochastic in time, non-varying in space
DATM-SWITCH	Switch-on run/data atmosphere	20	Atmosphere forcing switched into positive NAO phase in year 1
PBATL1535N	Partial blocking	400	Temperature/salinity restoring between 15-35N in 5 degree band centered at 40W
PBATL3550N	Partial blocking	400	Temperature/salinity restoring between 35-50N in 5 degree band centered at 40W
D_ATM_R	Partial coupling	20X20 20X20	PC scheme is applied in the North Atlantic north of 45N in the twin experiments.

REFERENCES

Allan, R., T. Ansell, 2006: A New Globally Complete Monthly Historical Gridded Mean Sea Level Pressure Dataset (HadSLP2): 1850–2004. *J.Clim.,* **19**, 5816-5842.

Barsugli, J. J., D. S. Battisti, 1998: The Basic Effects of Atmosphere-Ocean Thermal Coupling on Midlatitude Variability*. *J.Atmos.Sci.,* **55**, 477-493.

Belkin, I. M., 2004: Propagation of the "Great Salinity Anomaly" of the 1990s around the northern North Atlantic. *Geophys.Res.Lett.,* **31**, L08306.

Belkin, I. M., S. Levitus, J. Antonov, and S. A. Malmberg, 1998: "Great Salinity Anomalies" in the North Atlantic. *Prog.Oceanogr.,* **41**, 1-68.

Bjerknes, J., 1964: Atlantic Air-Sea Interaction. *Adv.Geophys.,* **10**, 1-82.

Collins, M., M. Botzet, A. Carril, H. Drange, A. Jouzeau, M. Latif, S. Masina, O. Otteraa, H. Pohlmann, and A. Sorteberg, 2006: Interannual to Decadal Climate Predictability in the North Atlantic: A Multimodel-Ensemble Study. *J.Clim.,* **19**, 1195-1203.

Delworth, T., S. Manabe, and R. Stouffer, 1993: Interdecadal Variations of the Thermohaline Circulation in a Coupled Ocean-Atmosphere Model. *J.Clim.,* **6**, 1993-2011.

Delworth, T. L., R. J. Greatbatch, 2000: Multidecadal Thermohaline Circulation Variability Driven by Atmospheric Surface Flux Forcing. *J.Clim.,* **13**, 1481-1495.

Deser, C., M. L. Blackmon, 1993: Surface Climate Variations over the North Atlantic Ocean during Winter: 1900–1989. *J.Clim.,* **6**, 1743-1753.

Dickson, R. R., J. Meincke, S. A. Malmberg, and A. J. Lee, 1988: The great salinity anomaly in the northern North Atlantic 1968-1982. *Prog.Oceanogr.,* **20**, 103-151.

Dong, B., R. T. Sutton, 2005: Mechanism of Interdecadal Thermohaline Circulation Variability in a Coupled Ocean-Atmosphere GCM. *J.Clim.,* **18**, 1117-1135.

Döscher, R., C. W. Böning, and P. Herrmann, 1994: Response of Circulation and Heat Transport in the North Atlantic to Changes in Thermohaline Forcing in Northern Latitudes: A Model Study. *J.Phys.Oceanogr.,* **24**, 2306-2320.

Eden, C., R. J. Greatbatch, 2003: A Damped Decadal Oscillation in the North Atlantic Climate System. *J.Clim.,* **16**, 4043-4060.

Eden, C., R. J. Greatbatch, and J. Lu, 2002: Prospects for decadal prediction of the North Atlantic Oscillation (NAO). *Geophys.Res.Lett.,* **29**, 1466–1469.

Eden, C., J. Willebrand, 2001: Mechanism of Interannual to Decadal Variability of the North Atlantic Circulation. *J.Clim.,* **14**, 2266-2280.

Eisenman, I., N. Untersteiner, and J. S. Wettlaufer, 2007: On the reliability of simulated Arctic sea ice in global climate models. *Geophys.Res.Lett.,* **34**.

Ganachaud, A., C. Wunsch, 2000: Improved estimates of global ocean circulation, heat transport and mixing from hydrographic data. *Nature,* **408**, 453-457, doi:10.1038/35044048.

Gerdes, R., C. Köberle, 1995: On the Influence of DSOW in a Numerical Model of the North Atlantic General Circulation. *J.Phys.Oceanogr.,* **25**, 2624-2642.

Greatbatch, R. J., K. A. Peterson, 1996: Interdecadal variability and oceanic thermohaline adjustment. *J.Geophys.Res.[Oceans],* **101**, 20467-20482.

Greatbatch, R. J., S. Zhang, 1995: An Interdecadal Oscillation in an Idealized Ocean Basin Forced by Constant Heat Flux. *J.Clim.,* **8**, 81-91.

Griffies, S. M., K. Bryan, 1997: Predictability of North Atlantic Multidecadal Climate Variability. *Science,* **275**, 181-184.

Griffies, S. M., E. Tziperman, 1995: A Linear Thermohaline Oscillator Driven by Stochastic Atmospheric Forcing. *J.Clim.,* **8**, 2440-2453.

Grötzner, A., M. Latif, and T. P. Barnett, 1998: A Decadal Climate Cycle in the North Atlantic Ocean as Simulated by the ECHO Coupled GCM. *J.Clim.,* **11**, 831-847.

Häkkinen, S., 2000: Decadal Air–Sea Interaction in the North Atlantic Based on Observations and Modeling Results. *J.Clim.,* **13**, 1195-1219.

Hakkinen, S., P. B. Rhines, 2004: Decline of Subpolar North Atlantic Circulation During the 1990s. *Science,* **304**, 555-559.

Hatun, H., A. B. Sando, H. Drange, B. Hansen, and H. Valdimarsson, 2005: Influence of the Atlantic Subpolar Gyre on the Thermohaline Circulation. *Science,* **309**, 1841-1844.

Hurrell, J. W., Y. Kushnir, G. Ottersen, and M. Visbeck, 2003: The North Atlantic Oscillation: Climate Significance and Environmental Impact. Geophysical Monograph.

Jacob R. L., 1997: Low frequency variability in a simulated atmosphere–ocean system.

James, I. N., P. M. James, 1989: Ultra-low-frequency variability in a simple atmospheric circulation model. *Nature,* **342**, 53-55.

Kaplan, A., M. A. Cane, Y. Kushnir, A. C. Clement, M. B. Blumenthal, and B. Rajagopalan, 1998: Analyses of global sea surface temperature 1856-1991. *Journal of Geophysical Research,* **103**, 18567-18590.

Kaplan, A., Y. Kushnir, and M. A. Cane, 2000: Reduced Space Optimal Interpolation of Historical Marine Sea Level Pressure: 1854–1992. *J.Clim.,* **13**, 2987-3002.

Kushnir, Y., 1994: Interdecadal Variations in North Atlantic Sea Surface Temperature and Associated Atmospheric Conditions. *J.Clim.,* **7**, 141-157.

Kushnir, Y., W. Robinson, I. Bladé, N. M. J. Hall, S. Peng, and R. Sutton, 2002: Atmospheric GCM Response to Extratropical SST Anomalies: Synthesis and Evaluation. *J.Clim.,* **15**, 2233-2256.

Liu, Z., S. P. Harrison, J. Kutzbach, and B. Otto-Bliesner, 2004: Global monsoons in the mid-Holocene and oceanic feedback. *Clim.Dyn.,* **22**, 157-182.

Liu, Z., J. Kutzbach, and L. Wu, 2000: Modeling climate shift of El Nino variability in the Holocene. *Geophys.Res.Lett.,* **27**, 2265-2268.

Liu, Z., Y. Wang, R. Gallimore, M. Notaro, and I. C. Prentice, 2006: On the cause of abrupt vegetation collapse in North Africa during the Holocene: Climate variability vs. vegetation feedback. *Geophys.Res.Lett.,* **33**, No. L22709.

Liu, Z., L. Wu, 2004: Atmospheric Response to North Pacific SST: The Role of Ocean–Atmosphere Coupling. *J.Clim.,* **17**, 1859-1882.

Liu, Z., Q. Zhang, and L. Wu, 2004: Remote Impact on Tropical Atlantic Climate Variability: Statistical Assessment and Dynamic Assessment. *J.Clim.,* **17**, 1529-1549.

Mellor, G., 1999: Comments on "On the Utility and Disutility of JEBAR". *J.Phys.Oceanogr.,* **29**, 2117-2118.

Mosedale, T. J., D. B. Stephenson, M. Collins, and T. C. Mills, 2006: Granger Causality of Coupled Climate Processes: Ocean Feedback on the North Atlantic Oscillation. *J.Clim.,* **19**, 1182-1194.

Peng, S., W. A. Robinson, and S. Li, 2003: Mechanisms for the NAO Responses to the North Atlantic SST Tripole. *J.Clim.,* **16**, 1987-2004.

Pershing, A. J., C. H. Greene, C. Hannah, D. Sameoto, E. Head, D. G. Mountain, J. W. Jossie, M. C. Benfield, P. C. Reid, and T. G. Durban, 2001: Oceanographic responses to climate in the Northwest Atlantic. *Oceanography,* **14**, 76-82.

Pickart, R. S., T. K. McKee, D. J. Torres, and S. A. Harrington, 1999: Mean Structure and Interannual Variability of the Slopewater System South of Newfoundland*. *J.Phys.Oceanogr.,* **29**, 2541-2558.

Rayner, N., D. Parker, E. Horton, C. Folland, L. Alexander, D. Rowell, E. Kent, and A. Kaplan, 2003: Global analyses of sea surface temperature, sea ice, and night marine air temperature since the late nineteenth century. *J.Geophys.Res,* **108**, 4407, doi:10.1029/2002JD002670.

Rodwell, M. J., D. P. Rowell, and C. K. Folland, 1999: Oceanic forcing of the wintertime North Atlantic Oscillation and European climate. *Nature,* **398**, 320-323.

Selten, F. M., R. J. Haarsma, and J. D. Opsteegh, 1999: On the Mechanism of North Atlantic Decadal Variability. *J.Clim.,* **12**, 1956-1973.

Sura, P., M. Newman, 2008: The Impact of Rapid Wind Variability upon Air–Sea Thermal Coupling. *Journal of Climate,* **21**, 621-637.

Sutton, R. T., D. L. R. Hodson, 2005: Atlantic Ocean Forcing of North American and European Summer Climate. *Science,* **309**, 115-118.

Timmermann, A., M. Latif, R. Voss, and A. Grötzner, 1998: Northern Hemispheric Interdecadal Variability: A Coupled Air–Sea Mode. *J.Clim.,* **11**, 1906-1931.

Tourre, Y. M., B. Rajagopalan, and Y. Kushnir, 1999: Dominant Patterns of Climate Variability in the Atlantic Ocean during the Last 136 Years. *J.Clim.,* **12**, 2285-2299.

Weaver, A. J., S. Valcke, 1998: On the Variability of the Thermohaline Circulation in the GFDL Coupled Model. *J.Clim.,* **11**, 759-767.

Weisse, R., U. Mikolajewicz, and E. Maier-Reimer, 1994: Decadal variability of the North Atlantic in an ocean general circulation model. *J.Geophys.Res,* **99**, 12411-12422.

Woodruff, S. D., H. F. Diaz, S. J. Worley, R. W. Reynolds, and S. J. Lubker, 2005: Early Ship Observational Data and ICOADS. *Clim.Change,* **73**, 169-194.

Wu, L., Z. Liu, 2002: Is Tropical Atlantic Variability driven by the North Atlantic Oscillation? *Geophys.Res.Lett.,* **29**, 1653, doi:10.1029/2002GL014939.

--2005: North Atlantic Decadal Variability: Air–Sea Coupling, Oceanic Memory, and Potential Northern Hemisphere Resonance. *J.Clim.,* **18**, 331-349.

Yang, J., J. D. Neelin, 1993: Sea-ice interaction with the thermohaline circulation. *Geophys.Res.Lett.,* **20**, 217-220.

Zhang, R., G. K. Vallis, 2006: Impact of Great Salinity Anomalies on the Low-Frequency Variability of the North Atlantic Climate. *J.Clim.,* **19**, 470-482.

Figures

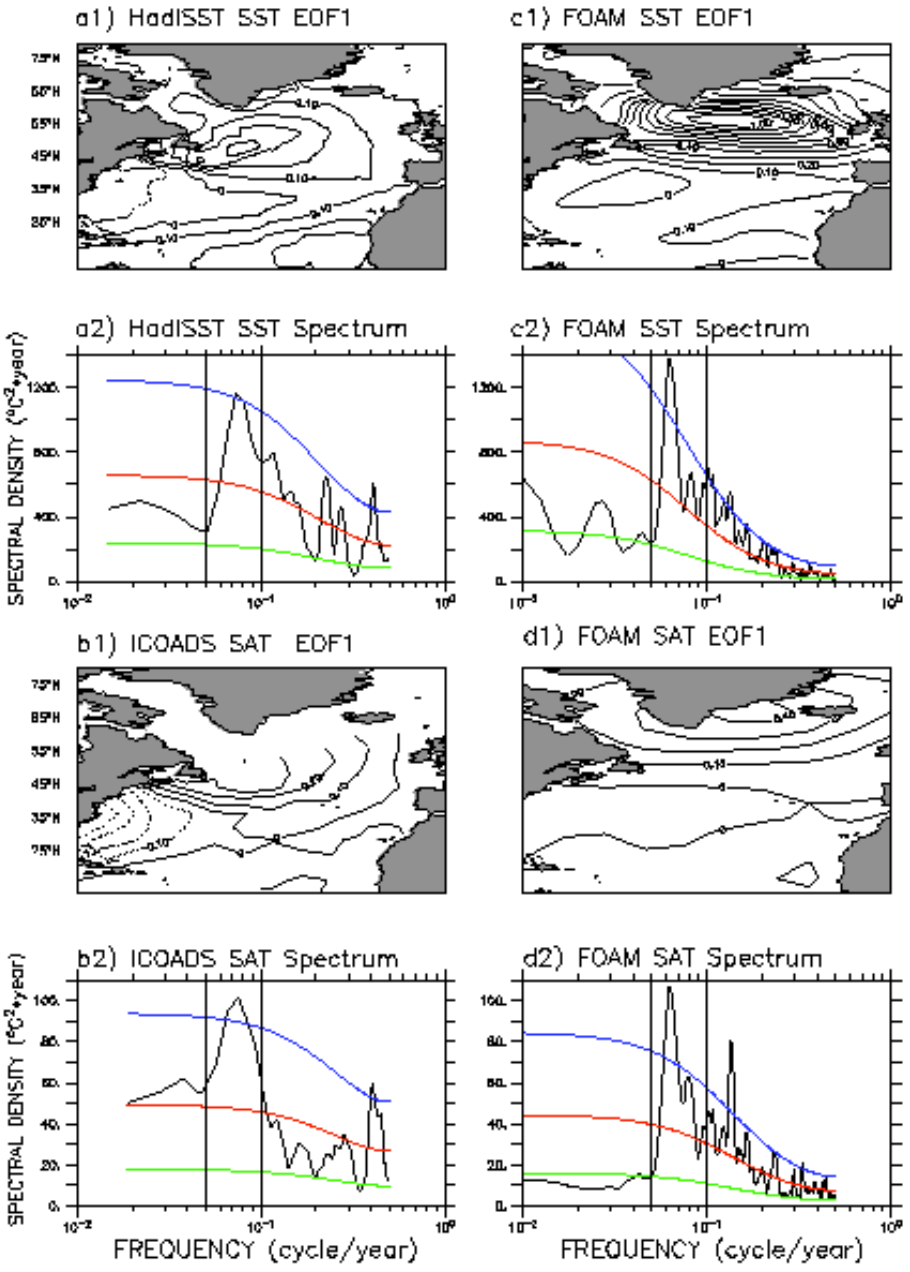

Fig. 1. Leading EOFs and power spectra of the leading PCs from HadISST SST (a1,a2), ICOADS SAT (b1,b2), FOAM CTRL SST (c1,c2) and FOAM CTRL SAT (d1,d2). The contour intervals of the normalized EOFs are 0.10 and the units of the power spectra are ($^oC^2$*year). Theoretical Markov spectrum and the 0.05/0.95 lower and upper confidence curves are also plotted. The vertical lines delineate the power spectra of the periods between 10 years and 20 years. All the EOFs and power spectra are calculated using NCL (NCAR Command Language).

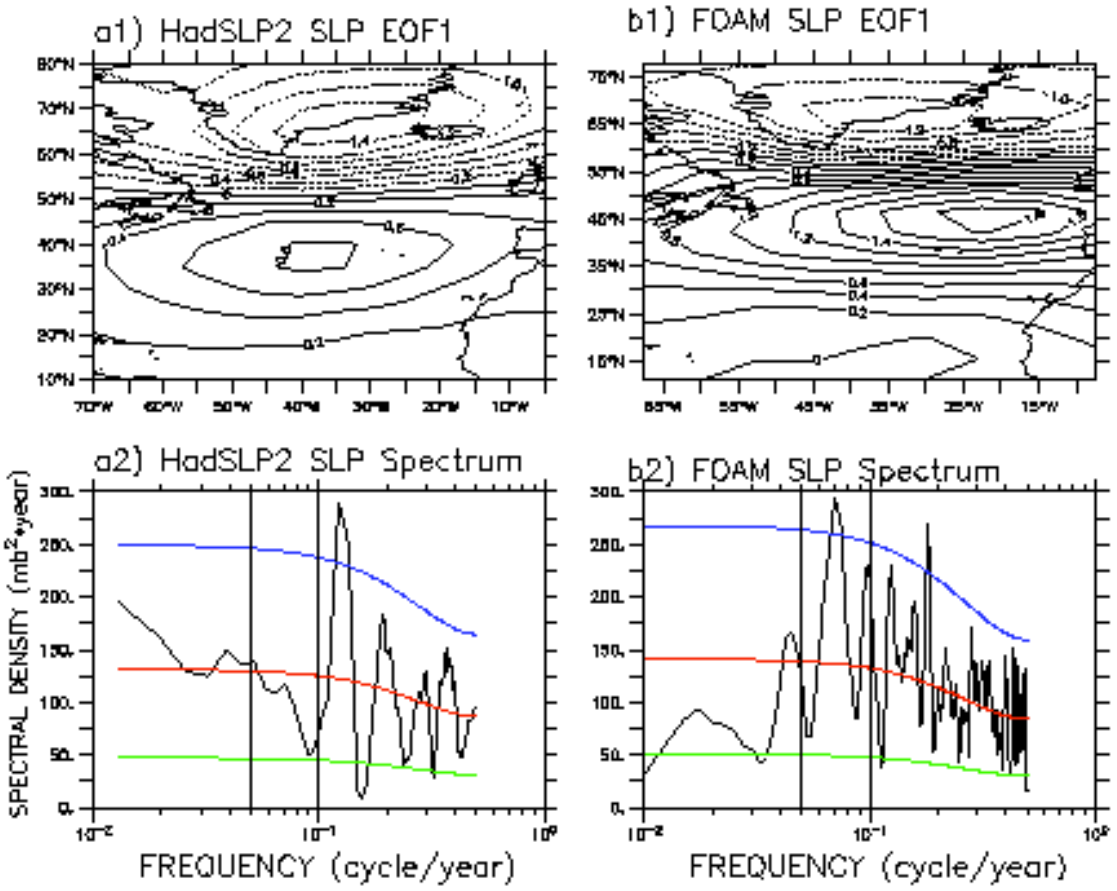

Fig. 2. (a1,a2), as Fig. 1 (a1,a2), but for HadSLP2 SLP. (b1,b2), as Fig. 1 (c1,c2), but for FOAM CTRL SLP. The contour intervals of the normalized EOFs are 0.20.

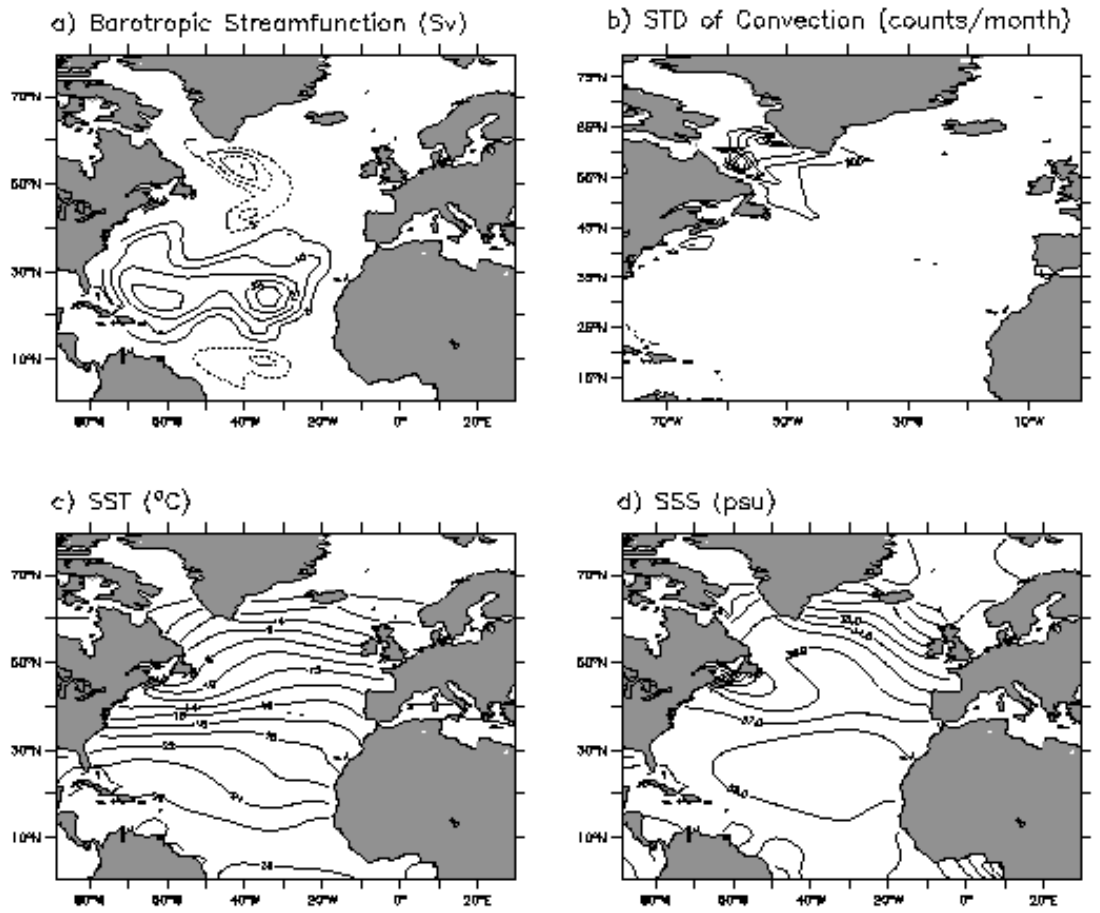

Fig. 3. Climatology of FOAM control simulation (CTRL) in the North Atlantic based on 400 year annual data output : a) barotropic stream function (Sv) b) standard deviation of convective frequency (counts/month) c) sea surface temperature (°C) d) sea surface salinity (psu). The contour intervals (ci) are a) 5 Sv, b) 200 counts/month, c) 2 °C, d) 1 psu.

.

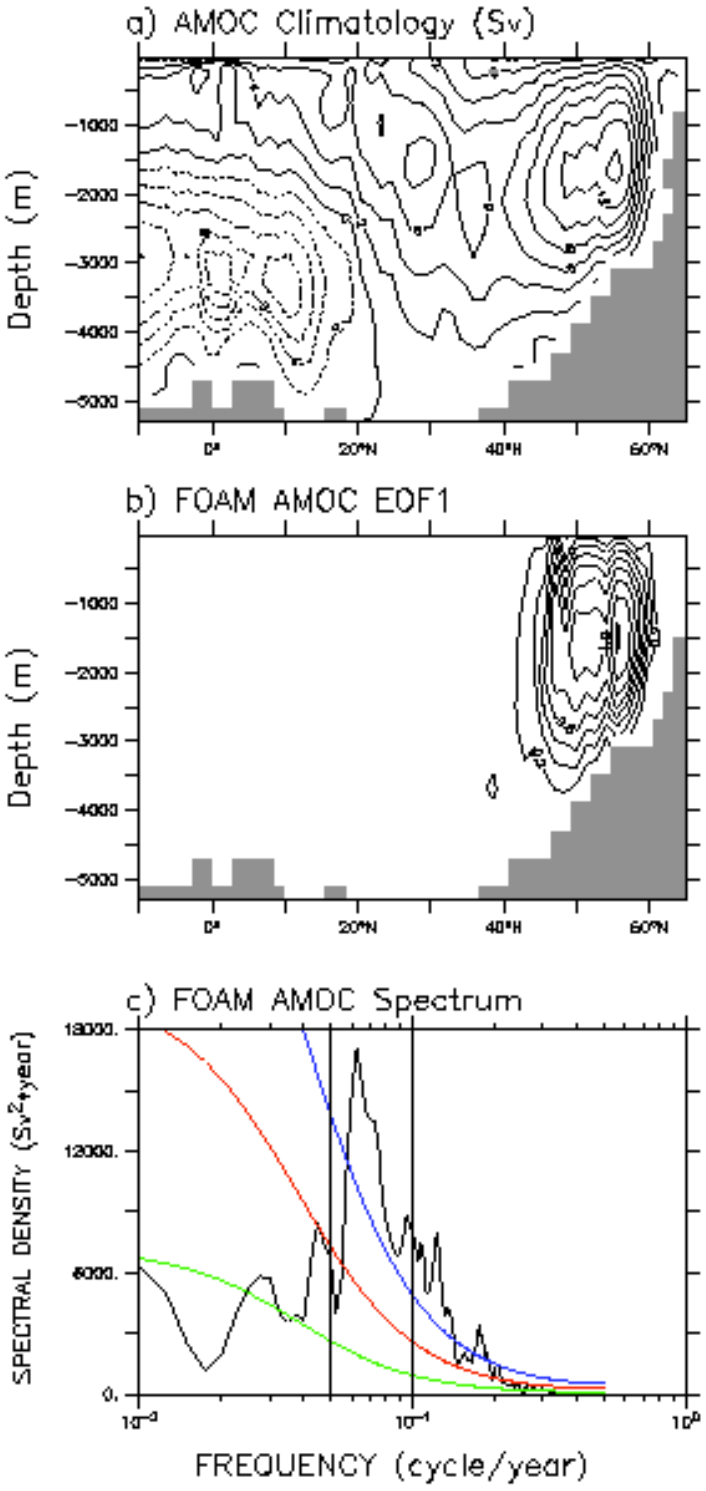

Fig. 4. (a) Climatology (ci: 2 Sv), (b) leading EOF (normalized) and (c) power spectrum (Sv^2*year) of the leading PC of AMOC from 400-year annual model output of FOAM's control simulation. Theoretical Markov spectrum and the 0.05/0.95 lower and upper confidence curves are also plotted. The vertical lines delineate the power spectra of the periods between 10 years and 20 years.

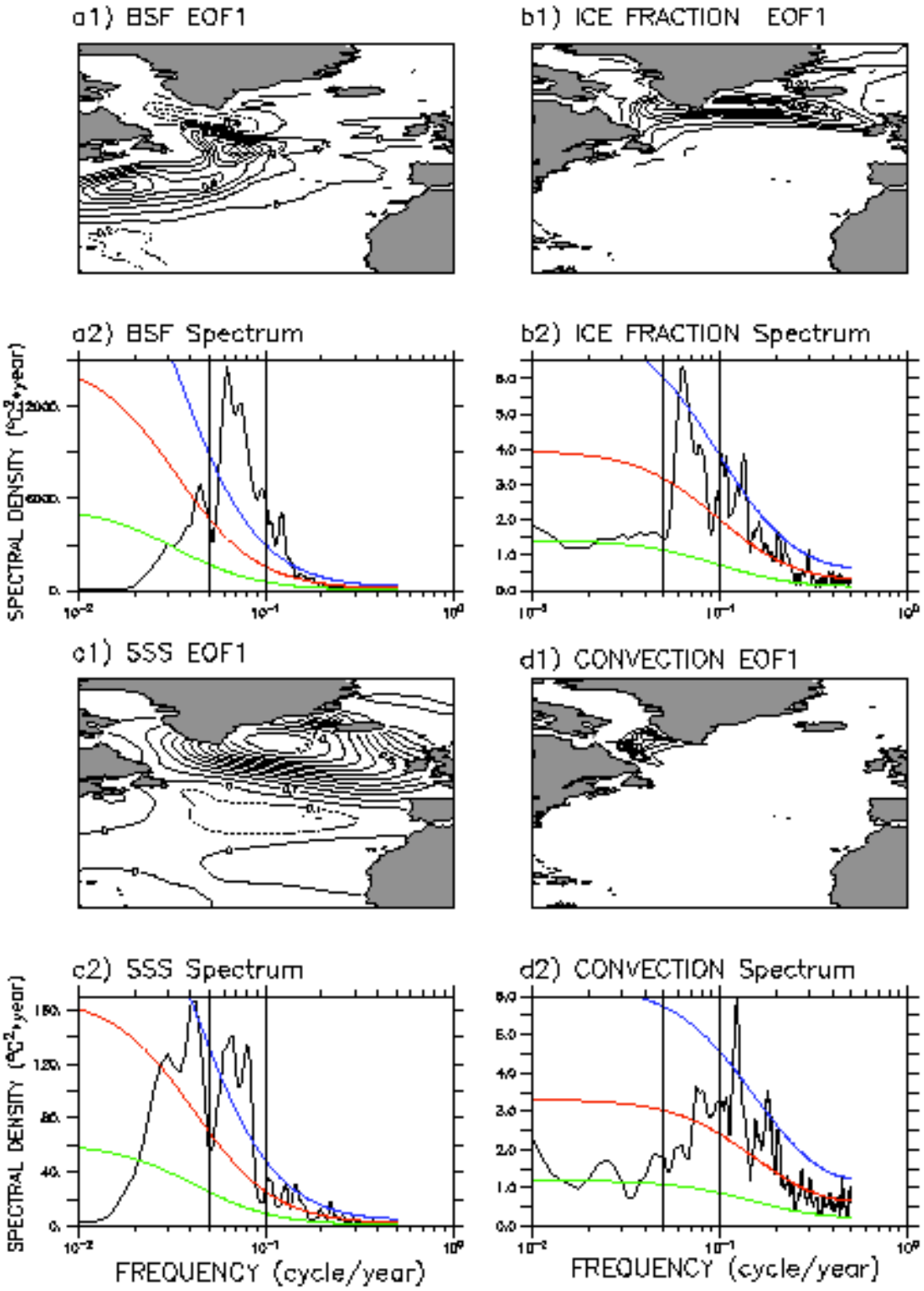

Fig. 5. As in Fig. 2, but for barotropical streamfunction (BSF, a1,a2), sea ice fraction (b1,b2), sea surface salinity (c1,c2) and convective frequency (d1,d2).

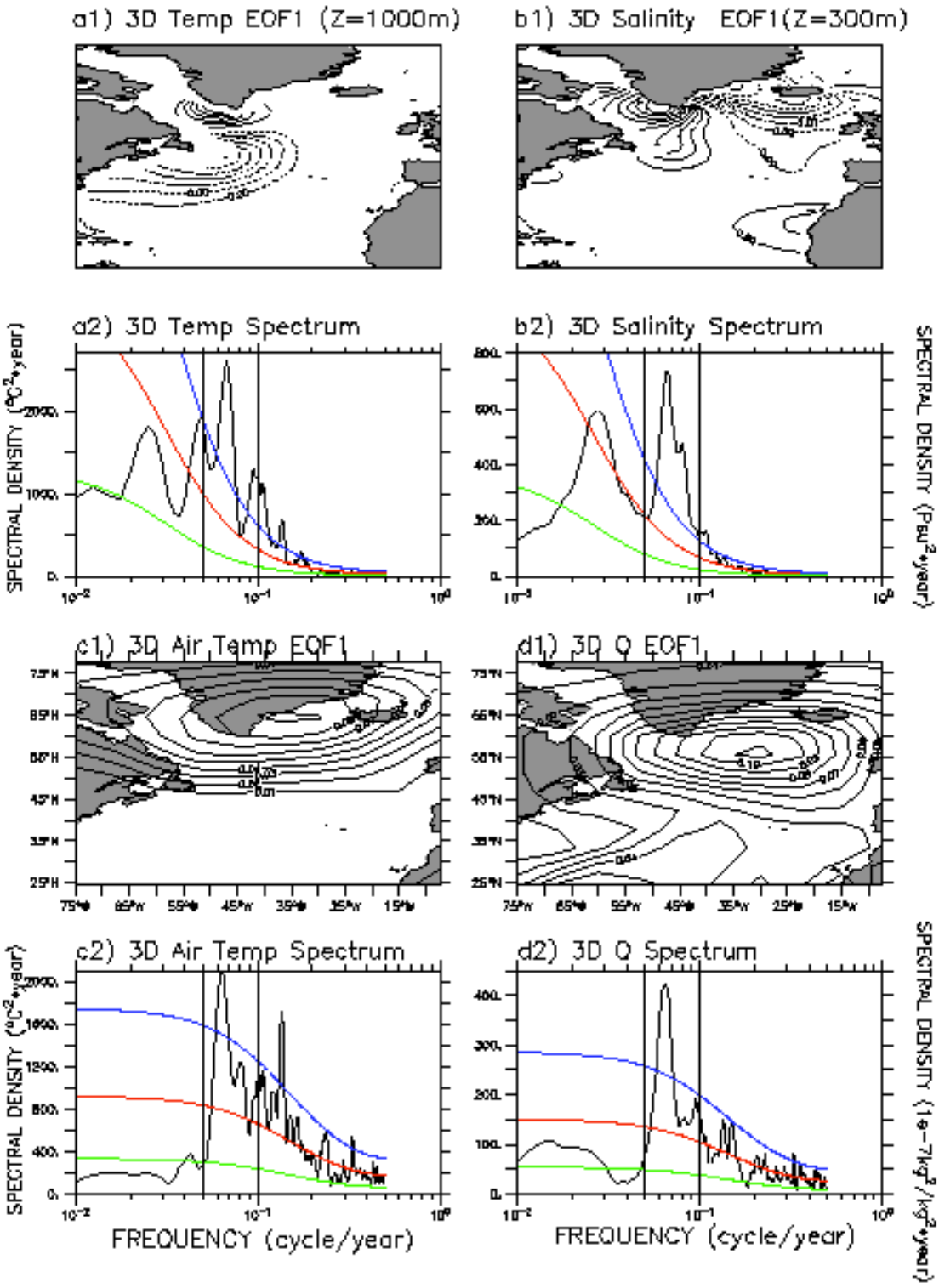

Fig. 6. As in Fig. 2, but for 3D ocean temperature at 1000 m depth (a1,a2), 3D ocean salinity at 300 m depth (b1,b2), 3D air temperature on the surface (c1,c2), and 3D specific humidity on the surface (d1,d2).

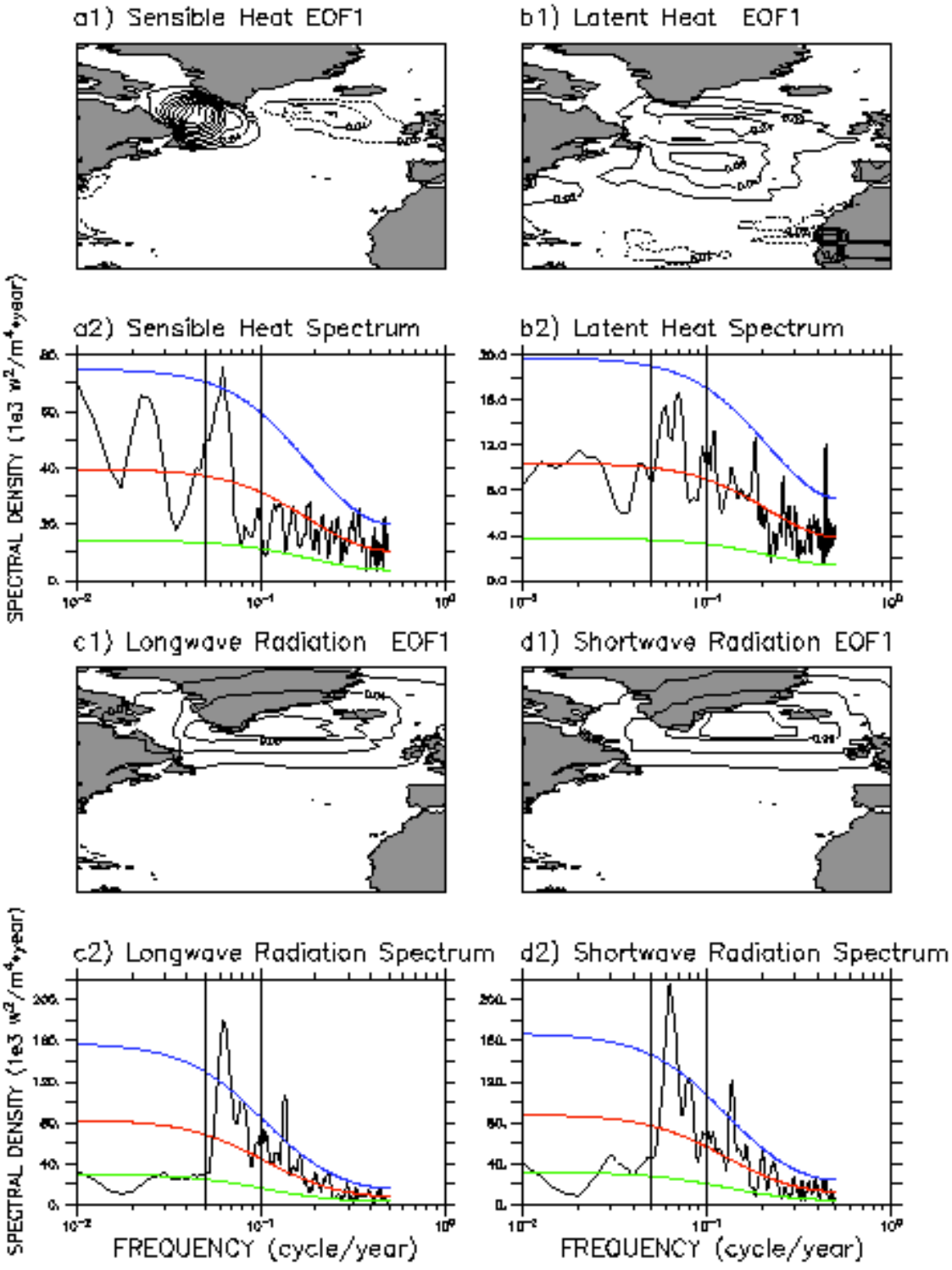

Fig. 7. As in Fig. 2, but for sensible heat flux (a1,a2), latent heat flux (b1,b2), longwave radiation flux (c1,c2) and shortwave radiation flux (d1,d2).

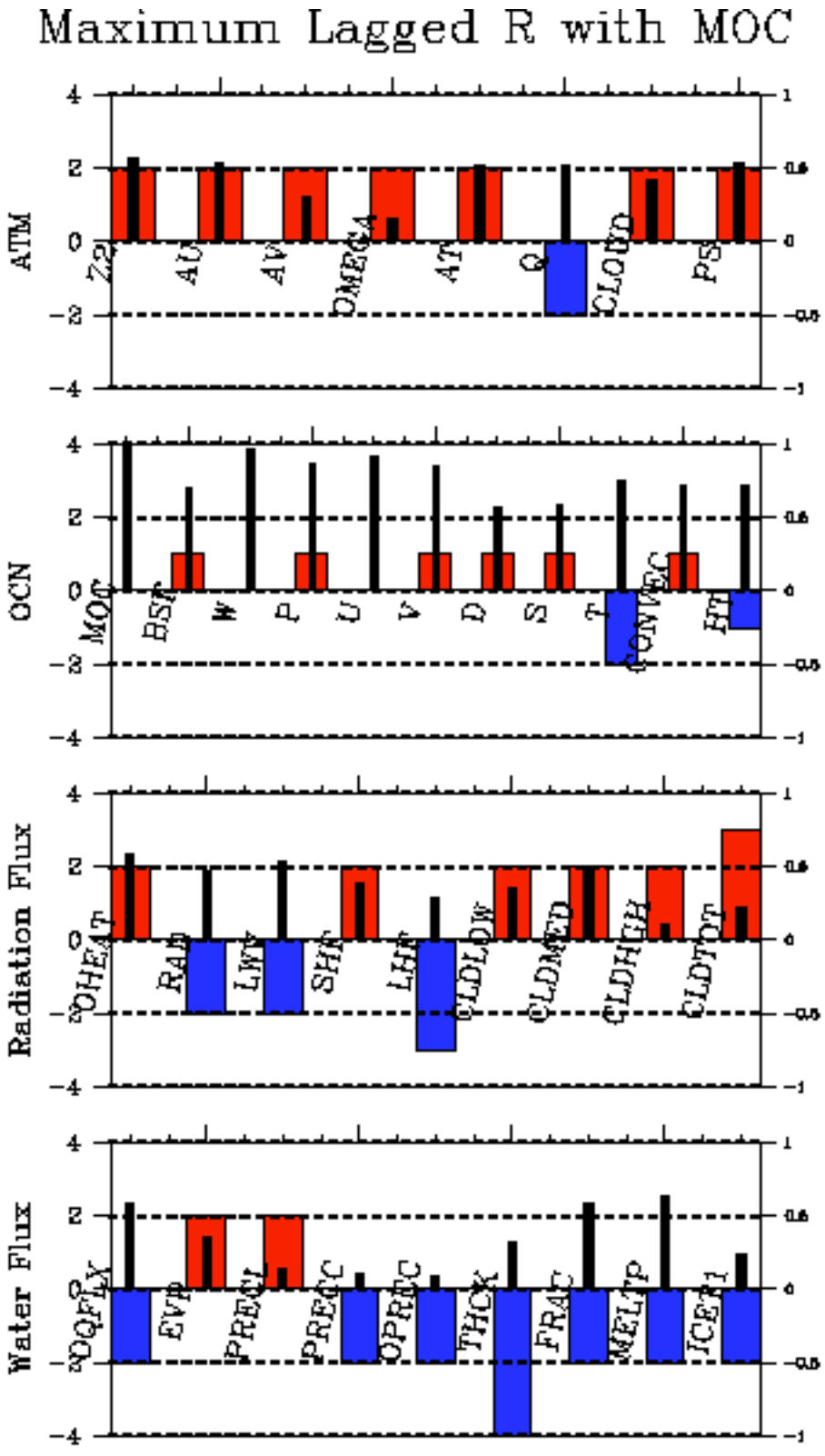
Maximum Lagged R with MOC
ATM
OCN
Radiation Flux
Water Flux
shading
The Lag at Maximum Correlation

Fig. 8. The maximum lagged correlations (MLC) and the corresponding lag of MLC (LoMLC) between PC1 of AMOC and PC1 of (a) Atmospheric, (b) oceanic, (c) radiative and (d) freshwater variables. Atmospheric variables include 3D geopotential heights (Z2), 3D zonal wind (AU), 3D meridional wind (AV), 3D vertical motion (OMEGA), 3D air temperature (AT), 3D specific humidity (Q) and surface pressure (PS). Oceanic variables include Atlantic Meridional overturning circulation (MOC), barotropic streamfunction (BSF), 3D vertical current (W), 3D dynamic topography (P), 3D zonal currents (U), 3D meridional currents (V), 3D density (D), 3D salinity (S), 3D ocean temperature (T), convections (CONVEC) and heat transport (HT). Radiative variables include heat flux into the ocean (OHEAT), short wave radiation (RAD), long wave radiation (LWV), sensible heat flux (SHF), latent heat flux (LHF), low cloud (CLDLOW), median cloud (CLDMED), high cloud (CLDHGH) and total cloud (CLDTOT). Freshwater variables include freshwater flux into the ocean (OQFLX), evaporation (EVP), large scale precipitation (PRECL), convective precipitation (PRECC), precipitation from atmosphere (OPREC), sea ice thickness (THCK), sea ice fraction (FRAC), melting potential (METLP), surface ice temperature (ICET1). The maximum lagged correlation (thin black bars) and the associated lag (thick red/blue bars) are scaled by the right and left axis, respectively. Only the absolute value of MLC is plotted.

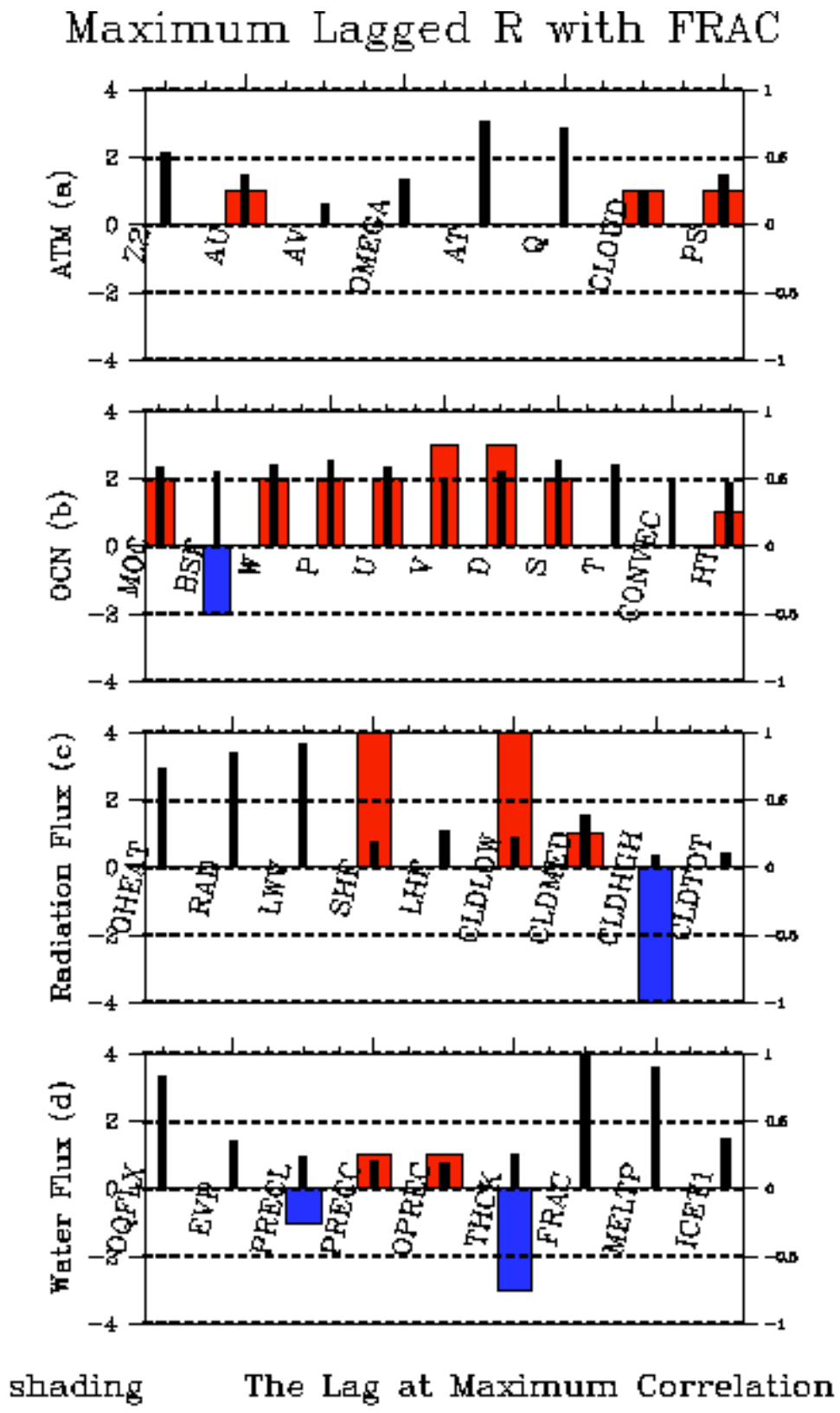

Fig. 9. Same as Fig. 5, but using PC1 of sea ice fraction (FRAC) as the index.

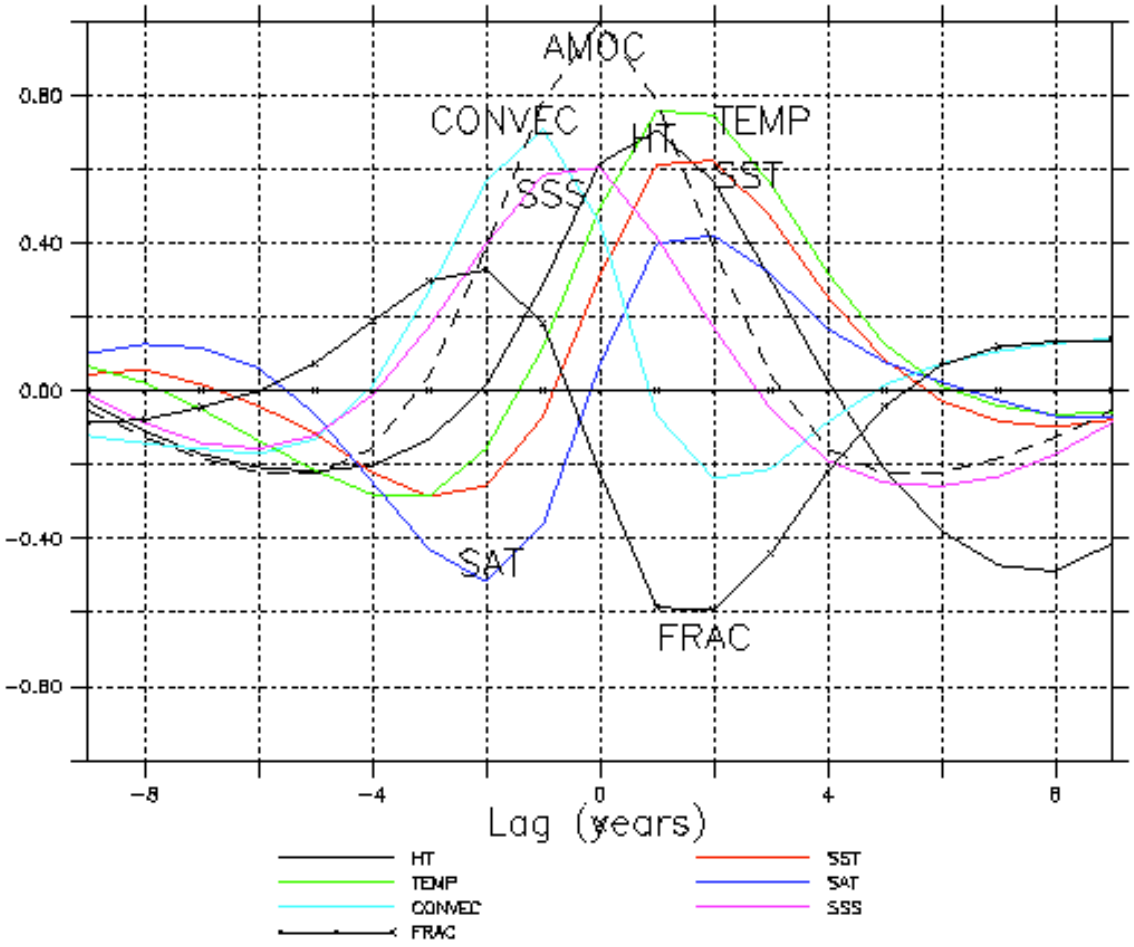

Fig. 10. Annually lagged correlation between the leading PC of AMOC and the leading PC of SAT (blue), convections (light blue), SST(purple), heat transport (black), 3D ocean temperature (green), SST (Red), AMOC (black dash), ice fraction (black dot).

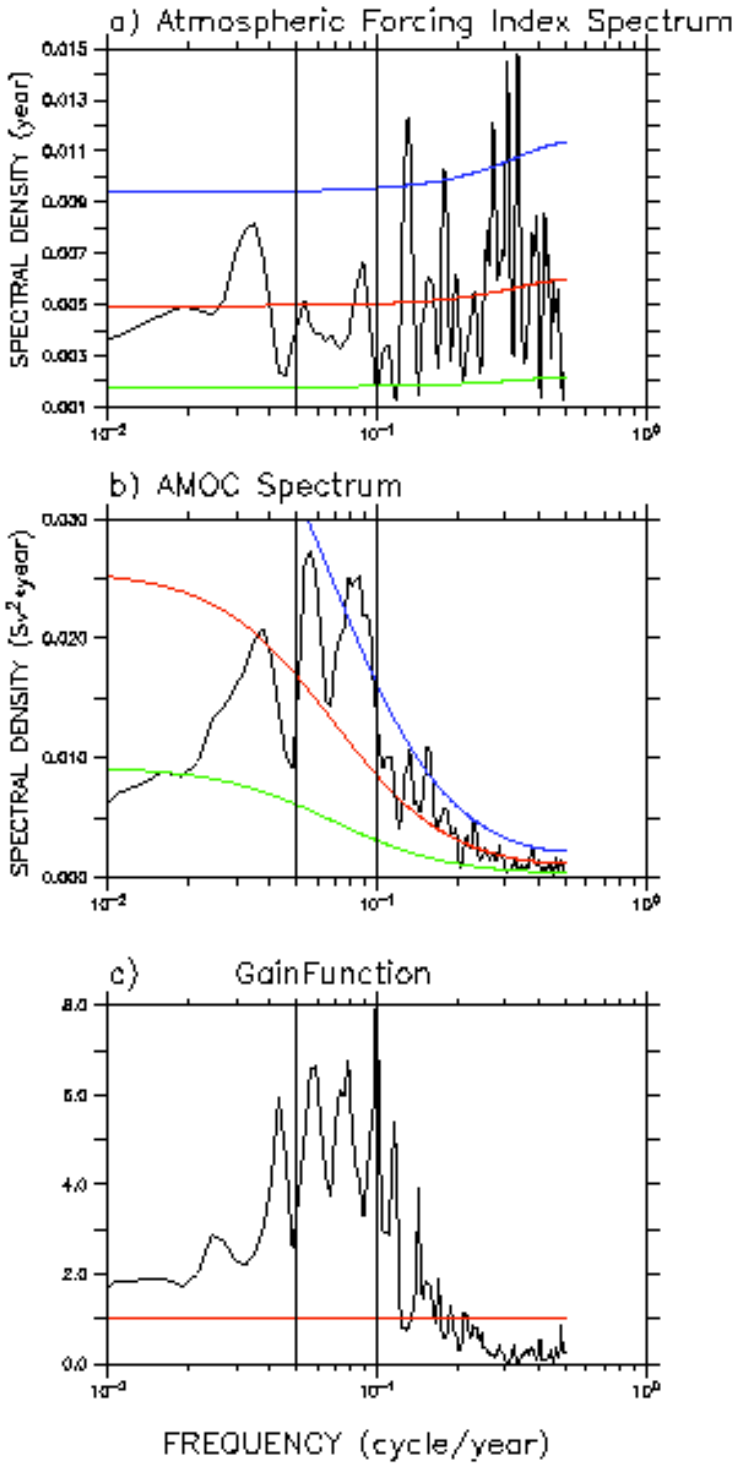

Fig. 11. (a) Power spectrum (1^2*year) of the atmospheric forcing index in DATM-STOC simulation. (b) as (a), but for the power spectrum (Sv^2*year) of leading PC of AMOC . (c) gain function for DATM-STOC simulation. The ratio between the normalized spectra of (b) and (a) is plotted as the gain function. Theoretical Markov spectrum and the 0.05/0.95 lower and upper confidence curves are also plotted. The vertical lines delineate the power spectra of the periods between 10 years and 20 years.

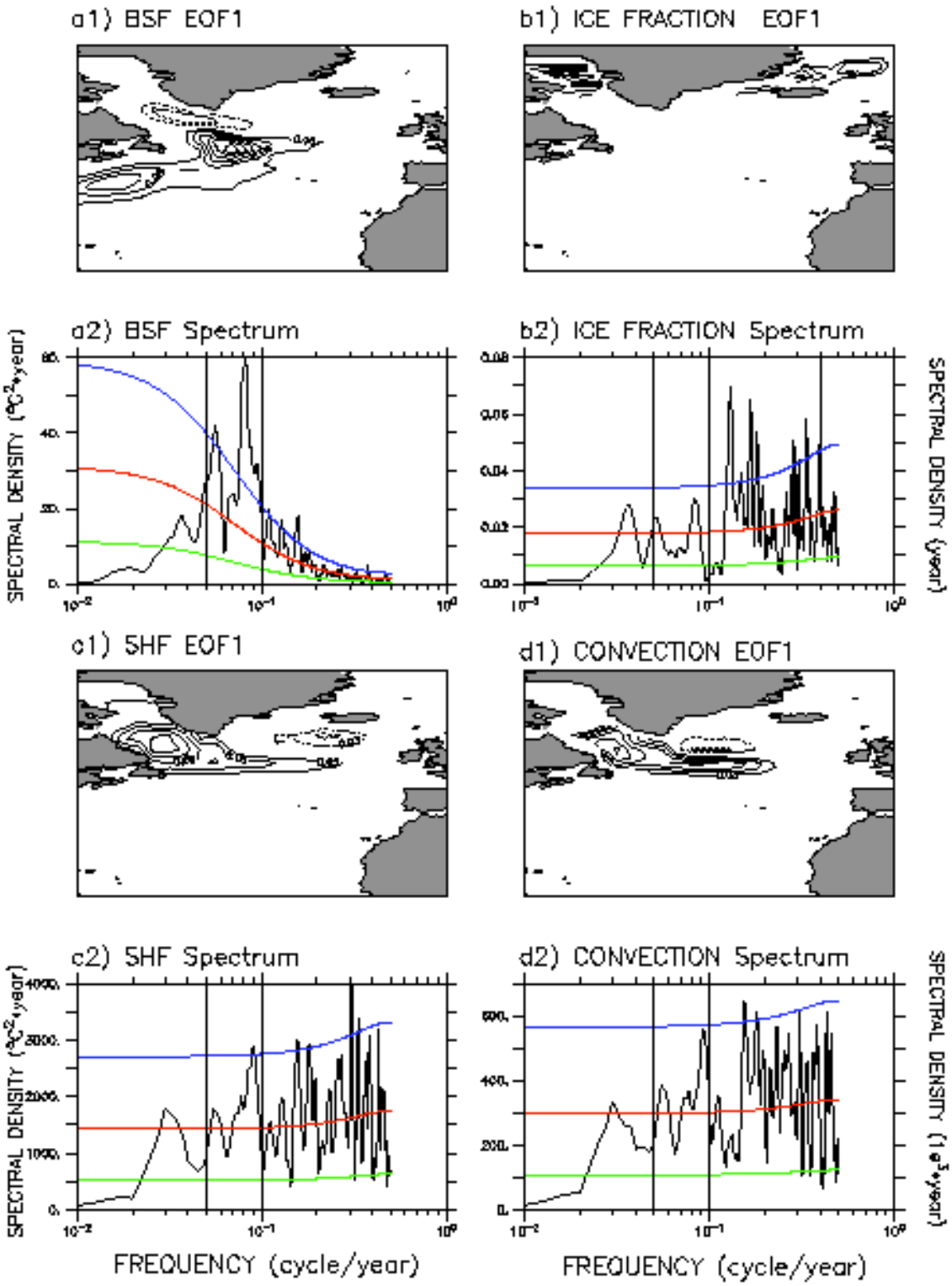

Fig. 12. As in Fig. 2, but for DATM-STOC. (a1,a2), BSF; (b1,b2), sea ice fraction; (c1,c2), sensible heat flux; (d1,d2), convective frequency.

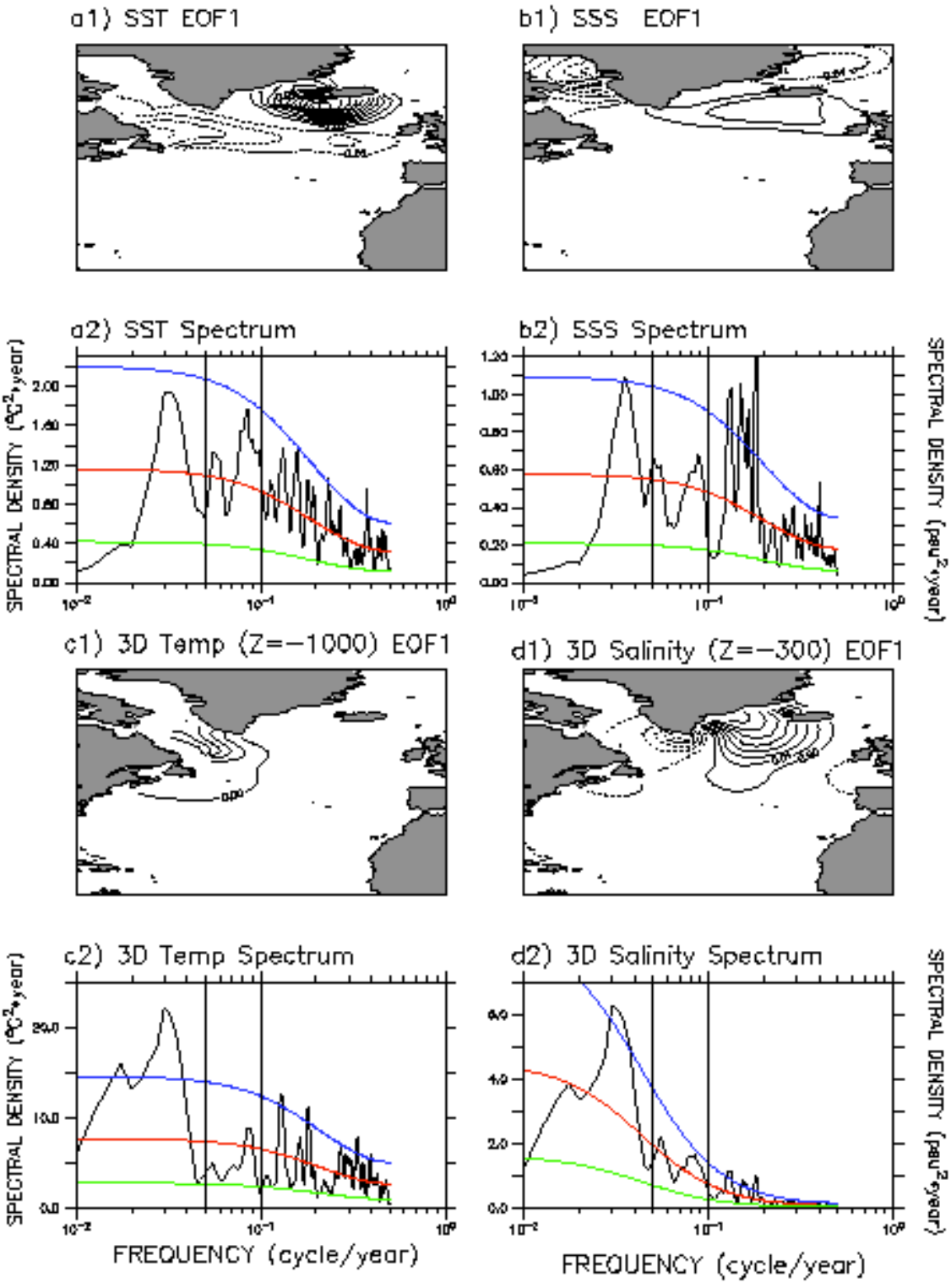

Fig. 13. As in Fig. 12, but for SST (a1,a2), SSS (b1,b2), 3D ocean temperature at 1000 m depth (c1,c2), 3D ocean salinity at 300 m depth (d1,d2).

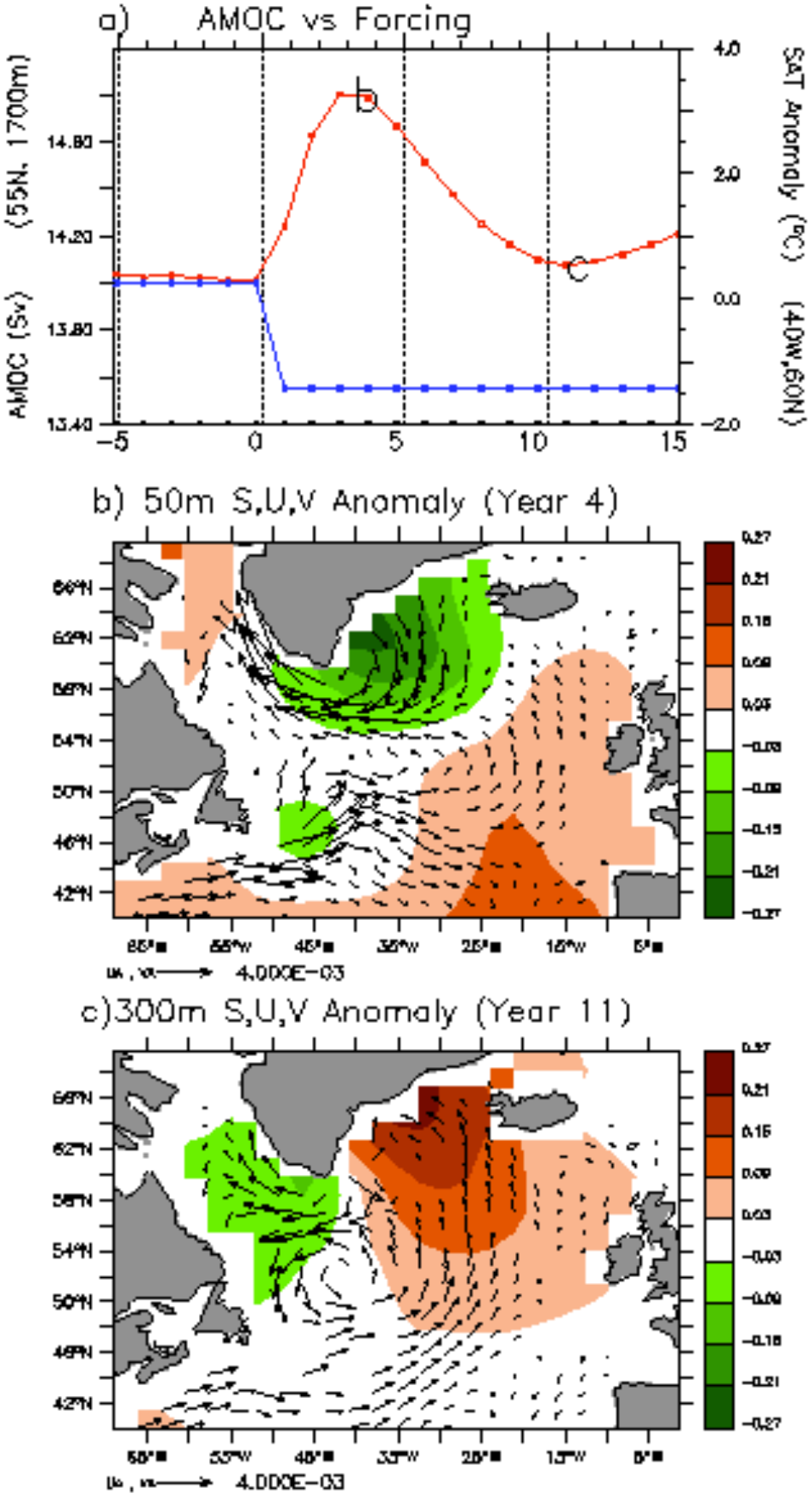
a) AMOC vs Forcing
AMOC (Sv) (55N, 1700m)
SAT Anomaly (°C) (40W,60N)
14.80
14.20
13.80
13.40
4.0
2.0
0.0
-2.0
-5
0
5
10
15
b
c
b) 50m S,U,V Anomaly (Year 4)
66°N
62°N
58°N
54°N
50°N
46°N
42°N
65°W
55°W
45°W
35°W
25°W
15°W
5°W
0.27
0.21
0.15
0.09
0.03
-0.03
-0.09
-0.15
-0.21
-0.27
4.000E-03
c)300m S,U,V Anomaly (Year 11)
66°N
62°N
58°N
54°N
50°N
46°N
42°N
65°W
55°W
45°W
35°W
25°W
15°W
5°W
0.27
0.21
0.15
0.09
0.03
-0.03
-0.09
-0.15
-0.21
-0.27
4.000E-03

Fig. 14. (a) AMOC intensity (Sv) and SAT anomaly (ºC) in DATM-SWITCH simulation. The positive NAO forcing is switched on at year zero. AMOC intensity is defined as the annual mean value of the streamfunction at 55N and 1700 m. SAT anomaly is plotted using the annual mean SAT anomaly at southern tip of Greenland (40W,60N). The letter "b" and "c" delineate the state of AMOC during which the Figure (b) and (c) is plotted, respectively. (b) The anomaly of salinity (psu; ci: 0.06), zonal (m/s) and meridional current (m/s) at 50m depth four years after the positive NAO forcing is switched-on. The current vector is omitted when either zonal current or meridional current is less than 1e-4 m/s. (c) as (b), but at 300 m and 11 years after the positive NAO forcing is switched-on.

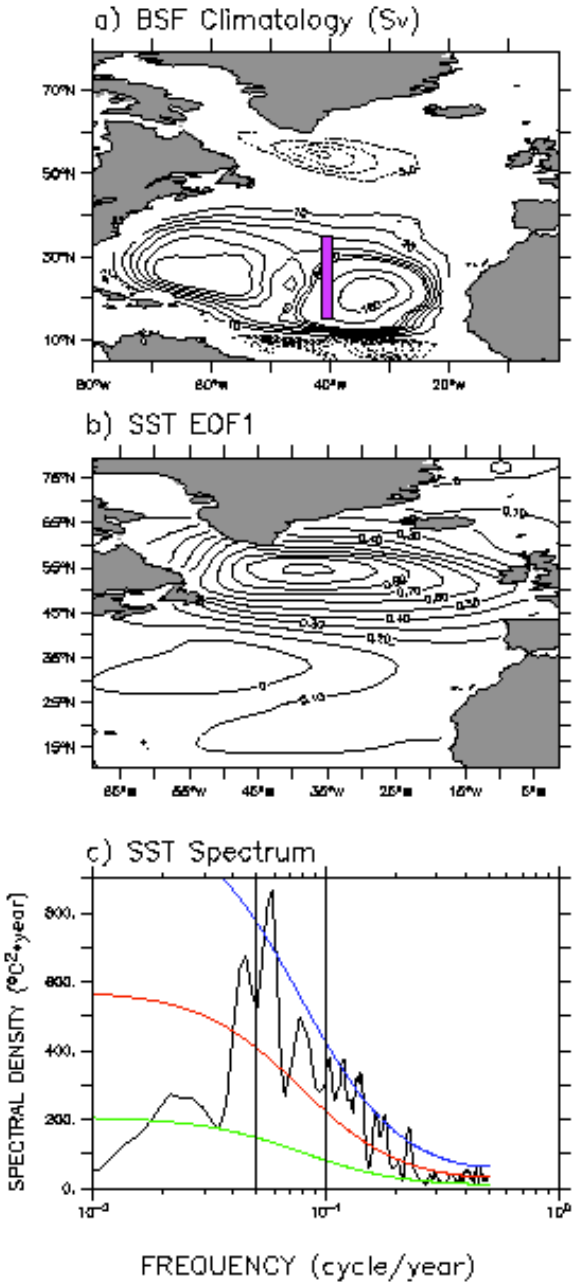

Fig. 15. (a) Climatology of barotropic streamfunction (Sv), (b) the leading EOF (normalized) and (c) the power spectrum ($^{o}C^{2}$*year) of the leading PC of SST based on 400 year annual data from experiment PBATL1535N. The solid bar in (a) denotes the position of the "sponge wall". The contour intervals in (a) are 5 Sv for negative BSF, 10 Sv for BSF smaller than 60 and 60 Sv for BSF larger than 60. Theoretical Markov spectrum and the 0.05/0.95 lower and upper confidence curves are also plotted. The vertical lines delineate the power spectra of the periods between 10 years and 20 years.

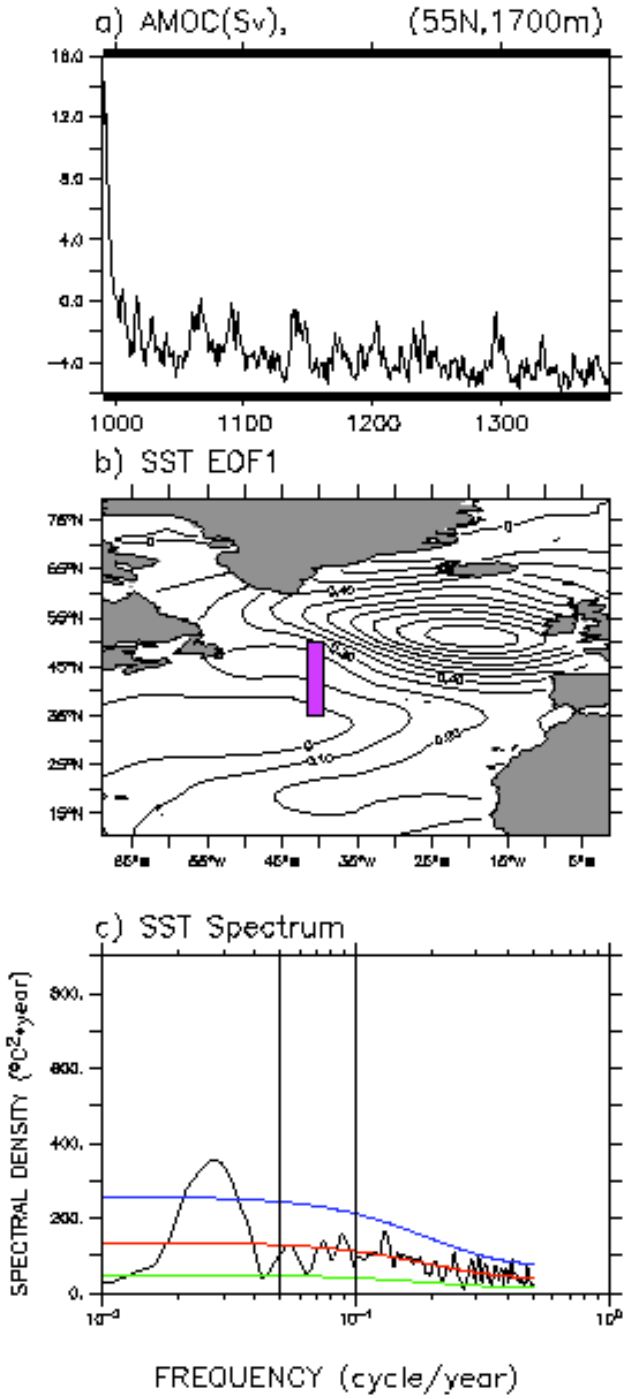

Fig. 16. (a) Time series of AMOC (Sv) at (55N, 1700 m), (b) the leading EOF (normalized) and (c) the power spectrum ($^oC^2$*year) of the leading PC of SST based on 400 year annual data from experiment PBATL3550N. The solid bar in (b) denotes the position of the "sponge wall". Theoretical Markov spectrum and the 0.05/0.95 lower and upper confidence curves are also plotted. The vertical lines delineate the power spectra of the periods between 10 years and 20 years.

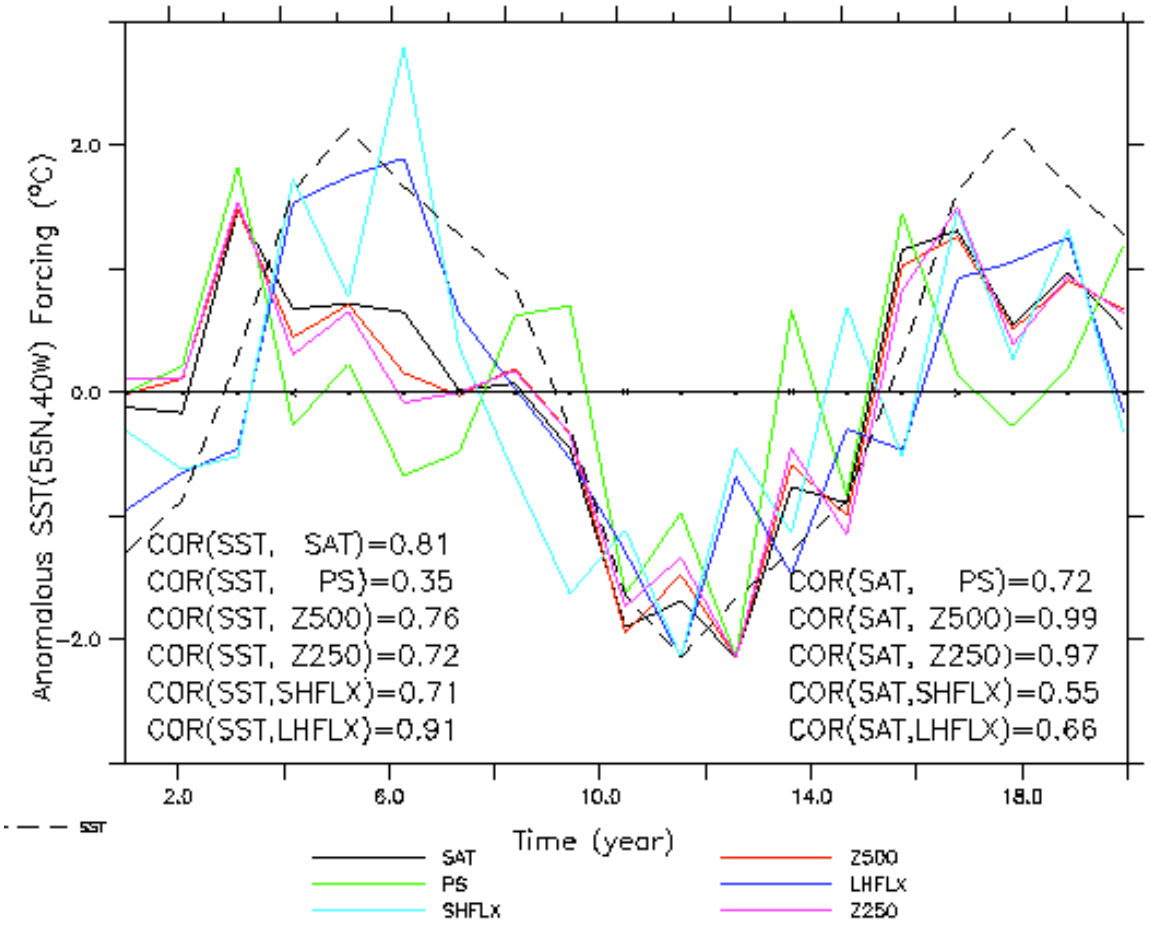

Fig. 17. The atmospheric response coefficient in experiment D_ATM_R. The 20-member ensemble of the difference of the various quantities in each twin experiment are analyzed using EOF technique. The derived leading EOF/PC are the atmospheric response patterns/coefficients for various quantities. The PCs are scaled by multiplying the ratio of minimum anomalous SST forcing at southern tip of Greenland (40W,55N) and the minimum of PCs, and the EOFs are scaled back by dividing the corresponding ratio. The atmospheric response coefficient of various quantities are SAT (black), Z500 (red), PS (green), latent heat flux (blue), sensible heat flux (light blue) and Z250 (purple). The SST forcing at Greenland (40W,55N) is also plotted in black dash. The correlation between the SST forcing and the response coefficient of various quantities are 0.81 (SAT), 0.35(PS), 0.76 (Z500), 0.72 (Z250), 0.71 (SHFLX) and 0.91 (LHFLX). The correlation between the response coefficient of SAT and that of other various quantities are 0.72 (PS), 0.99(Z500), 0.97 (Z250), 0.72 (Z250), 0.55 (SHFLX) and 0.66 (LHFLX).

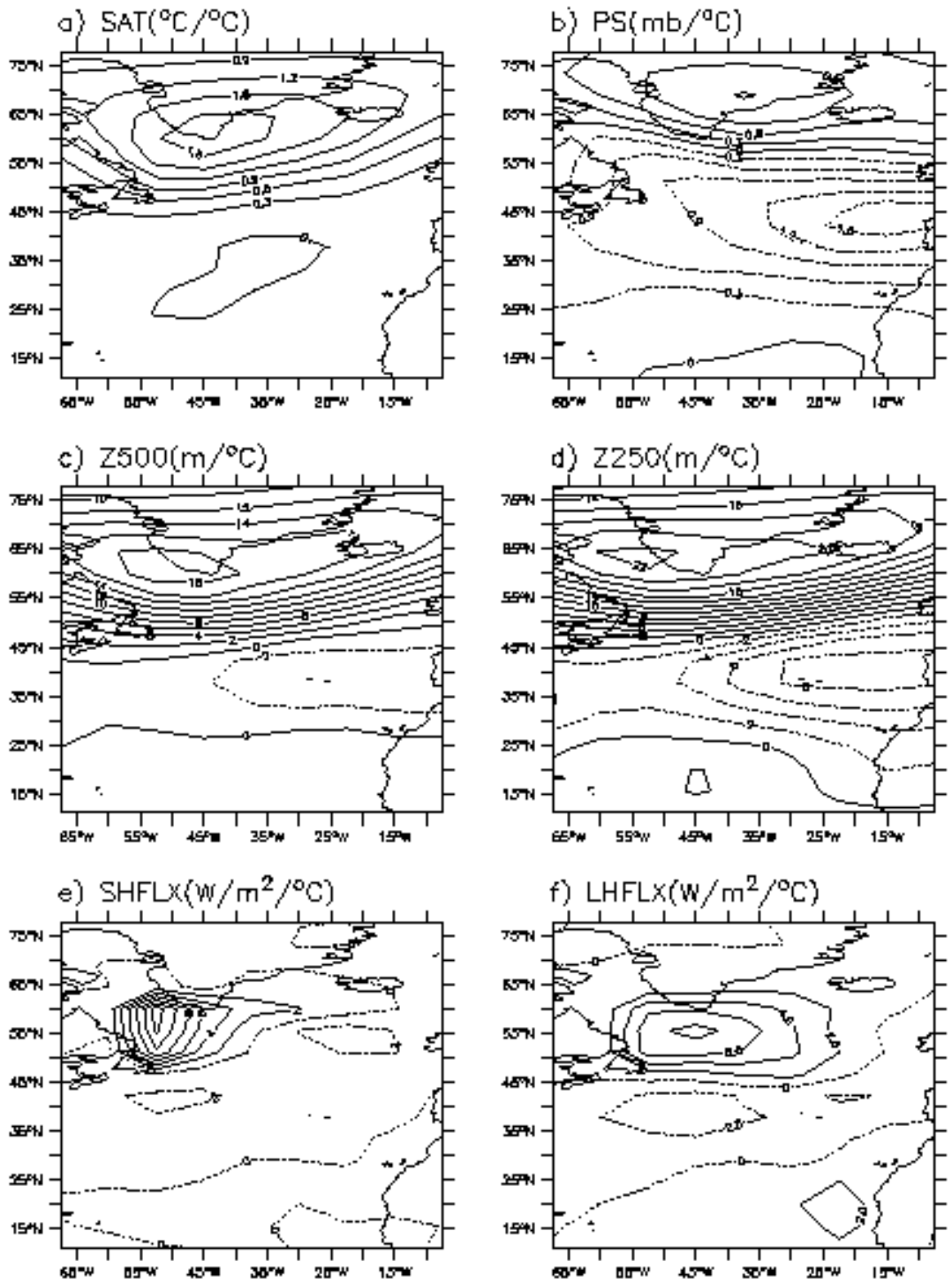

Fig. 18. The atmospheric response pattern: a) SAT (ci: 0.3 °C/°C), b) PS (ci: 0.3 mb/°C), c) Z500 (ci: 2 m/°C), d) Z250 (ci: 2 m/°C), e) SHFLX (ci: 2 W/m^2/°C), f) LHFLX(ci: 2 W/m^2/°C).

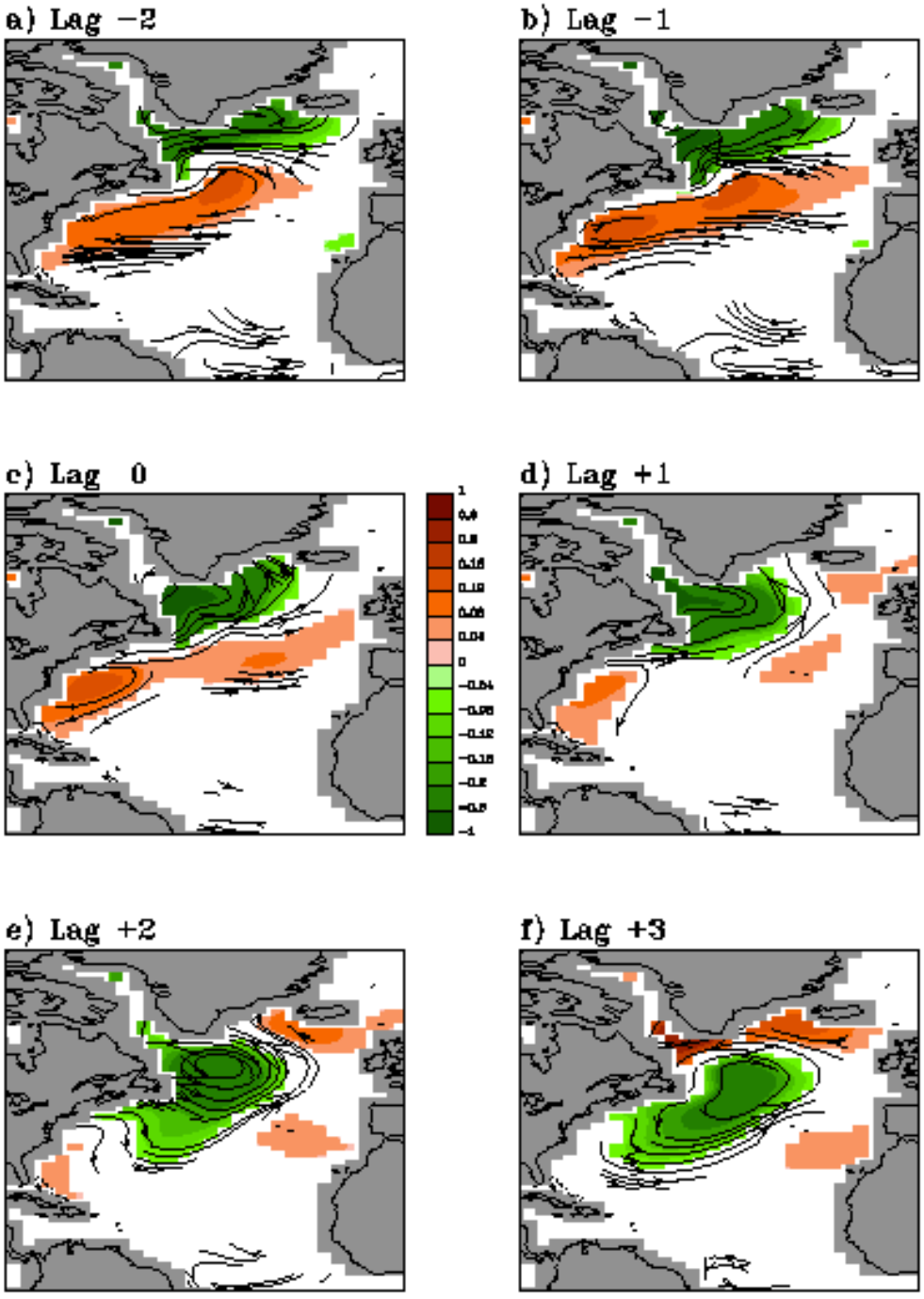

Fig. 19. The map of the lagged regression of 30m dynamic topography and the horizontal streamline upon the leading PC of AMOC in FOAM's control simulation. The contour intervals are 0.02 $m^2/s^2/Sv$ for values between -0.2 and 0.2 and 0.4 $m^2/s^2/Sv$ for values between -1 and -0.2 and between 0.2 and 1. The data are omitted for values weaker than 1/30 of the strongest lagged regression coefficients. The negative/positive lag indicates dynamic topography and the streamline is leading/lagging the 1st PC of AMOC.

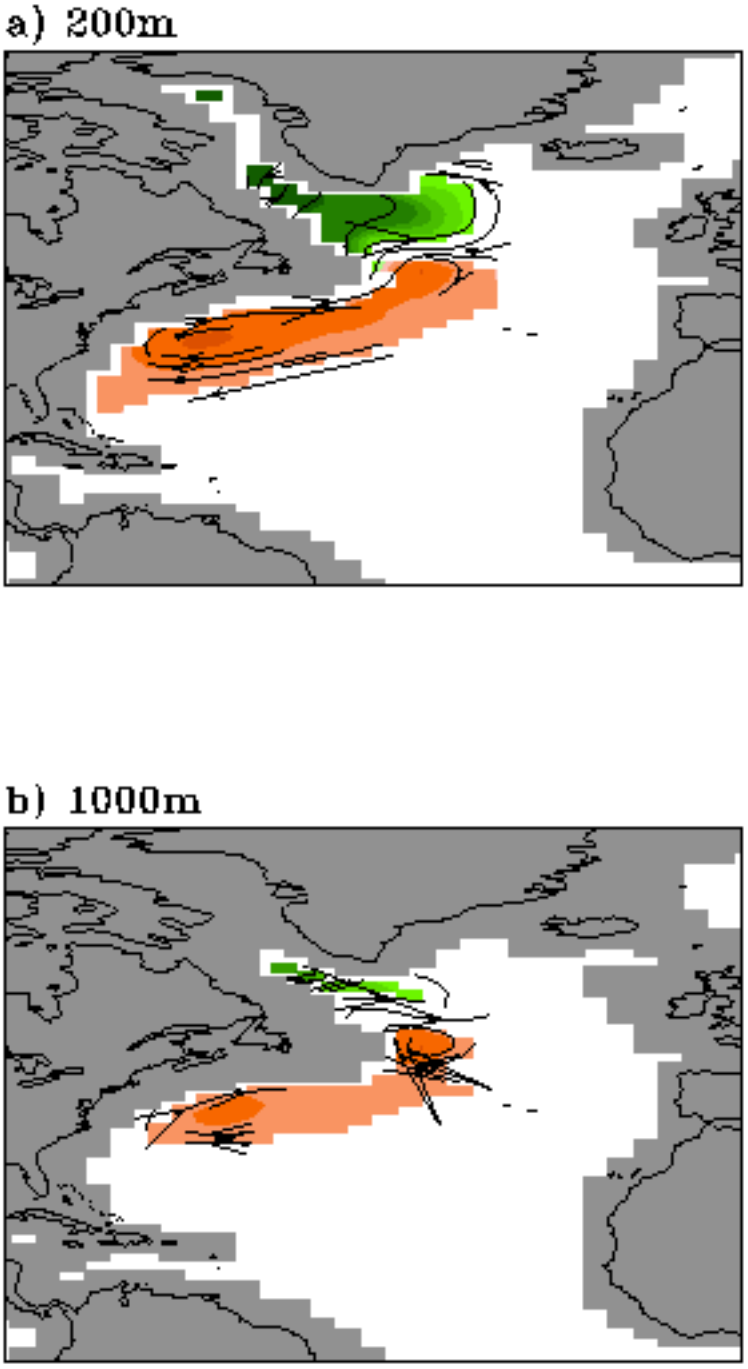

Fig. 20. Same as Fig. 14., but at a) 200 m and b) 1000 m during lag -1.

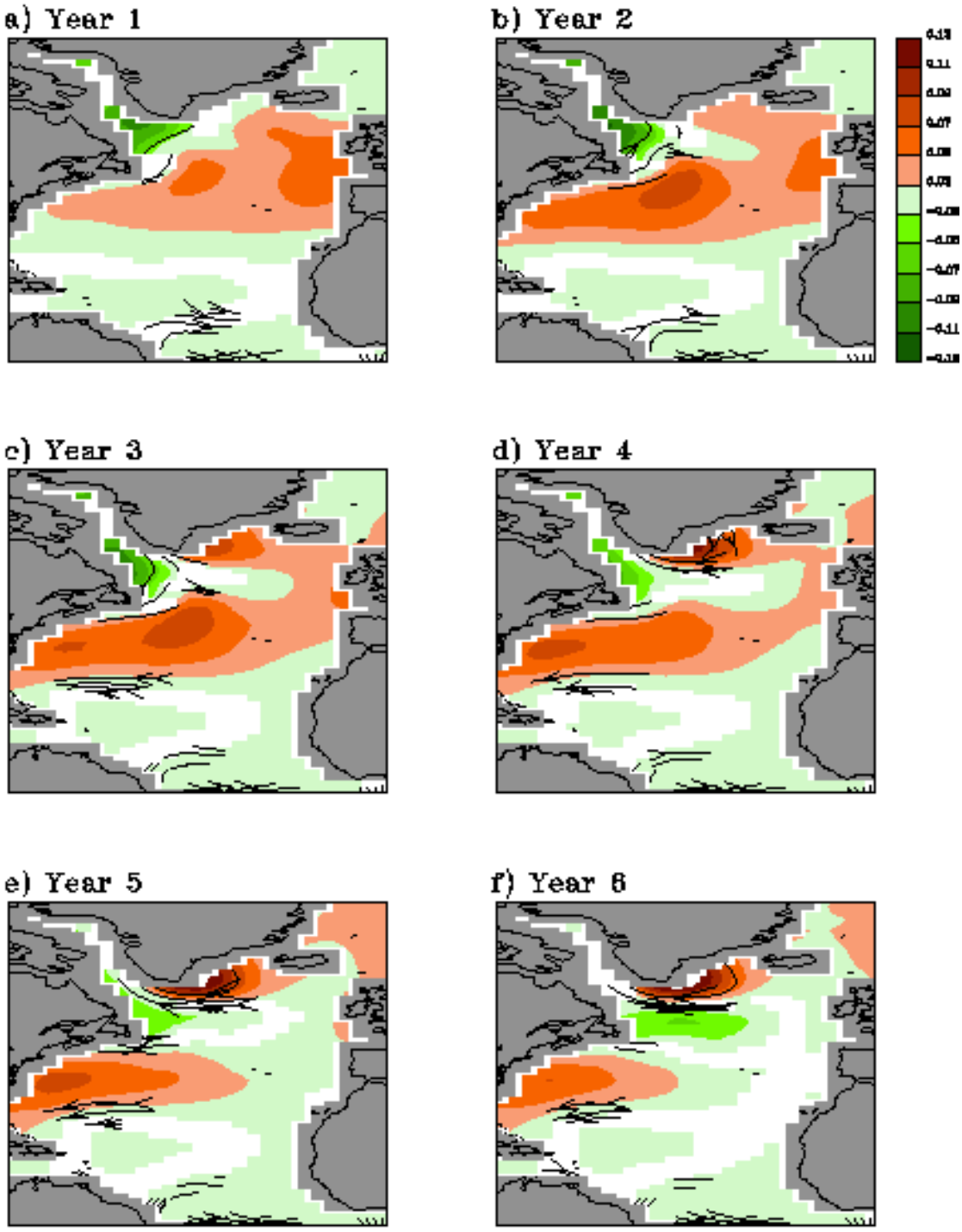

Fig. 21. 30m dynamic topography and the horizontal streamline anomaly in experiment DATM-SWITCH. The contour intervals are 0.02 m^2/s^2. The data are omitted for values weaker than 1/30 of the strongest anomaly.

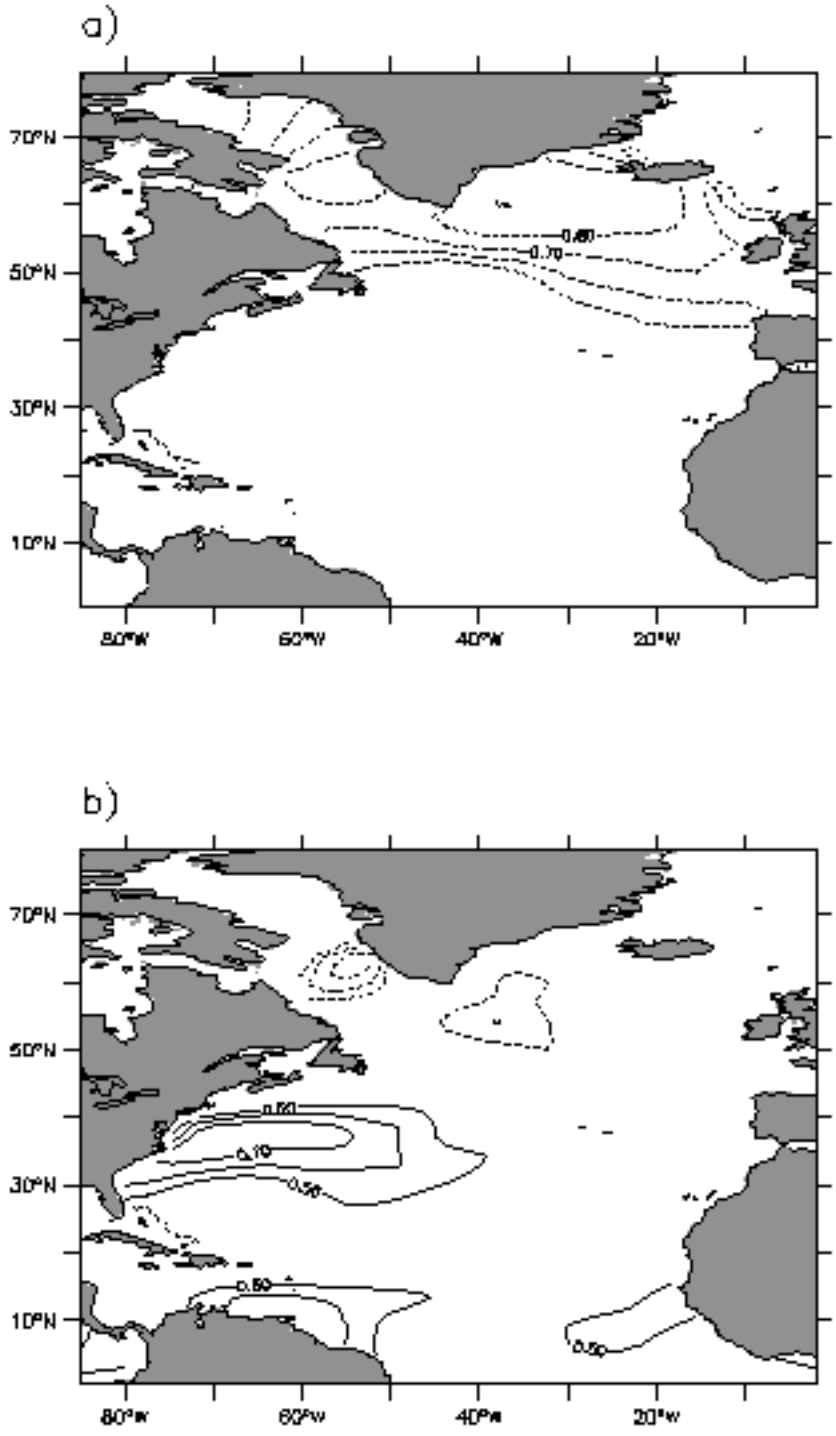

Fig. 22. Pointwise correlation between dynamic topography and a) salinity and b) temperature at 30m depth in FOAM's control simulation.

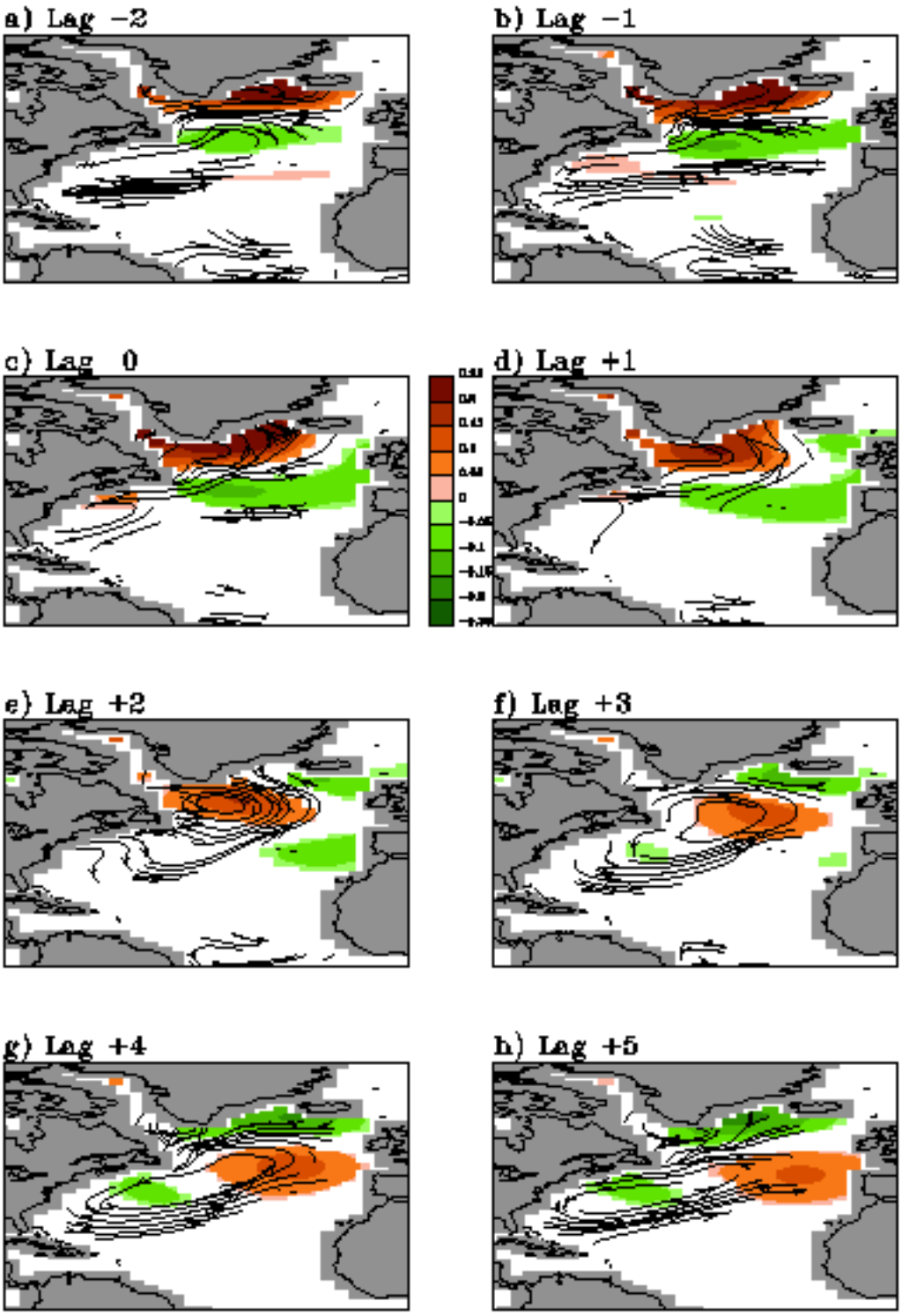

Fig. 23. Same as Fig. 14, but for salinity. The contour intervals are 0.05 psu/Sv for values between -0.20 and 0.20 and 0.15 psu/Sv for values between -0.35 and -0.20 and between 0.20 and 0.35. The data are omitted for values weaker than 1/10 of the strongest lagged regression coefficients.

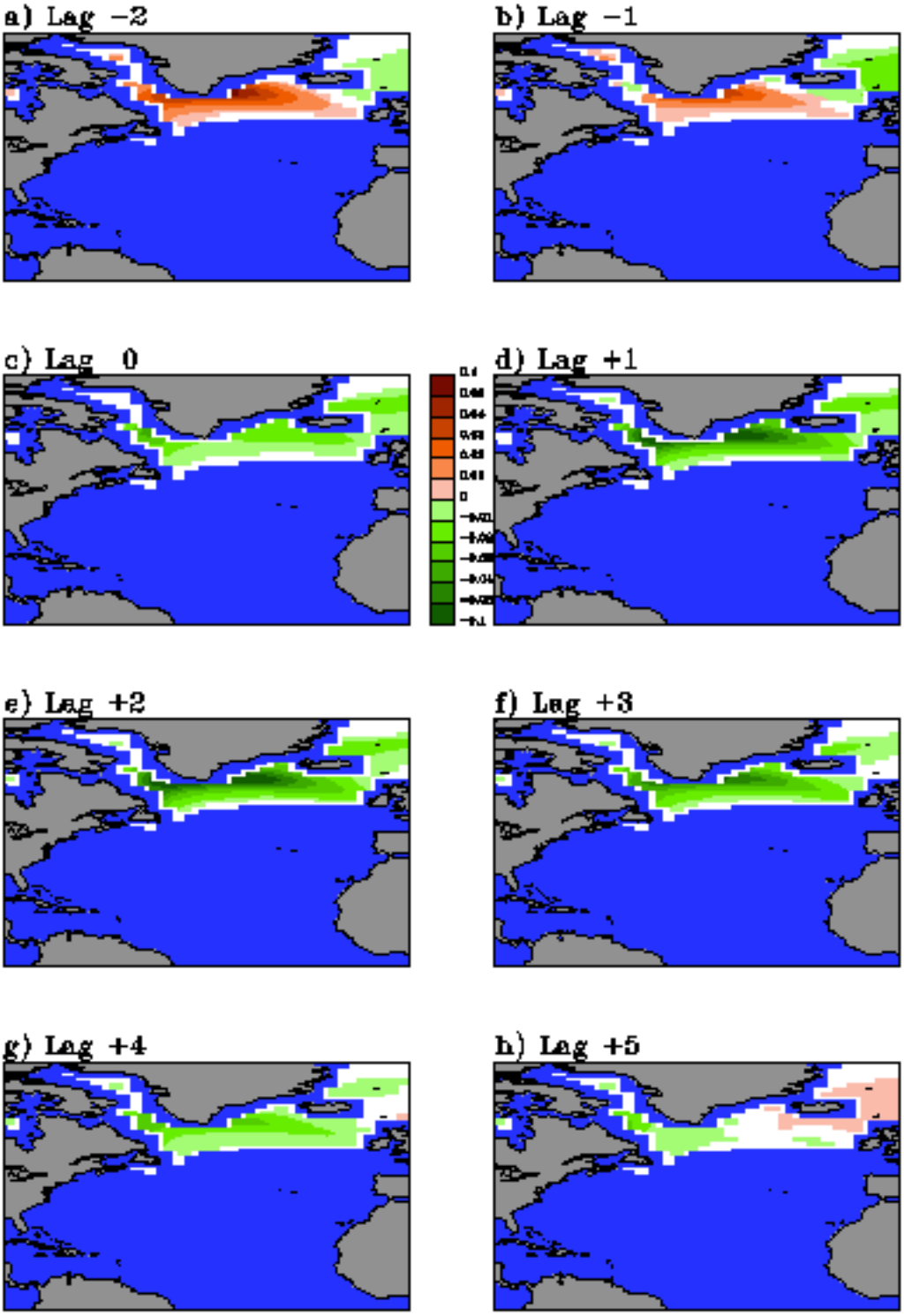

Fig. 24. Same as Fig. 14., but for sea ice fraction and without horizontal streamline. The contour intervals are 0.01 Sv^{-1} for values between -0.05 and 0.05 and 0.05 Sv^{-1} for values between -0.10 and -0.05 and between 0.05 and 0.10.

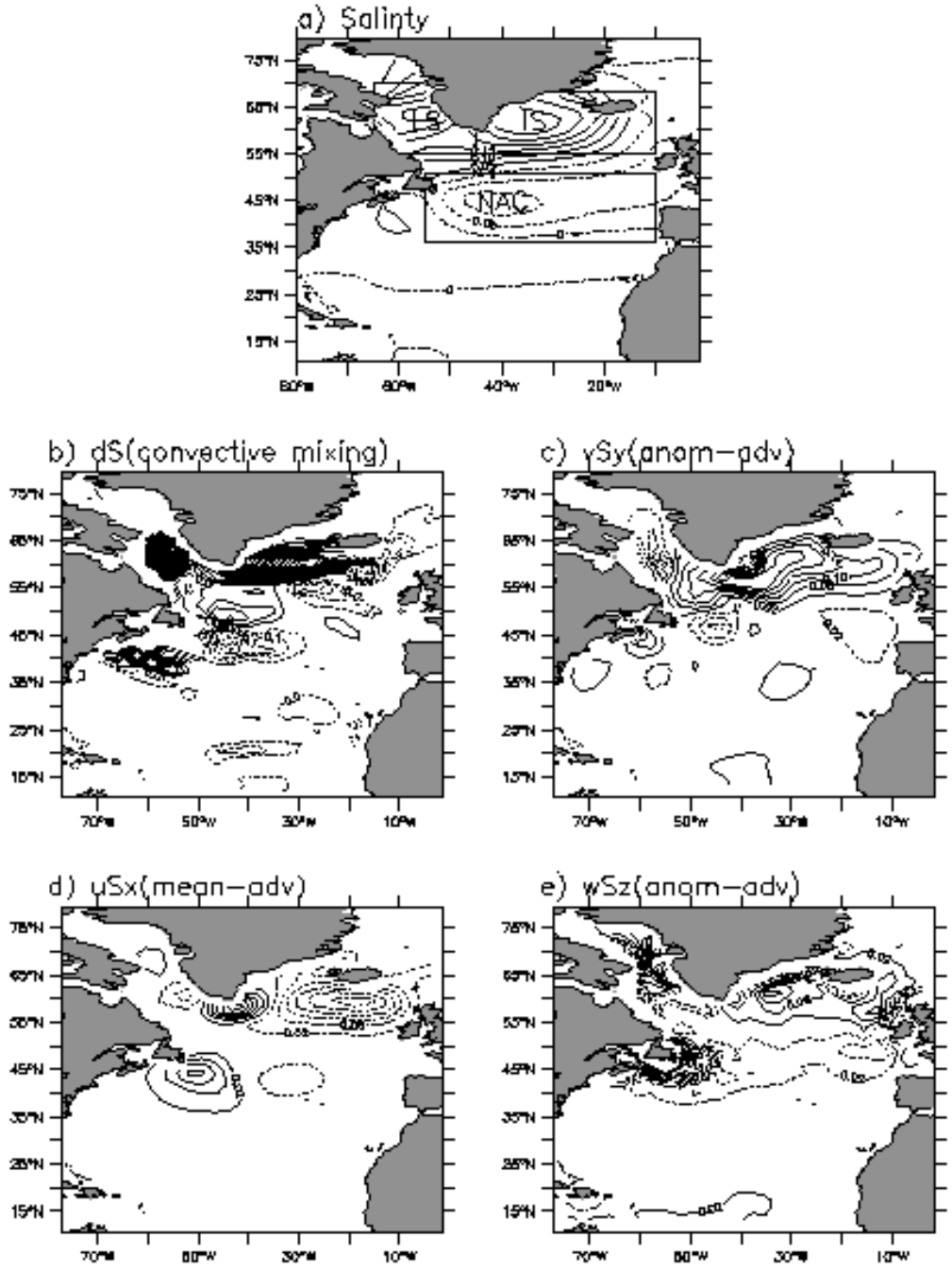

Fig. 25. The map of lagged regression of a) salinity and b)-e) various salinity tendency terms upon the leading PC of AMOC in FOAM's control simulation at 30m depth during lag -1. The various tendency terms are b) convective mixing, c) anomalous meridional transport, d) mean zonal transport, e) anomalous vertical transport. The contour intervals are a) 0.05 psu/Sv and b)-e) 0.04 psu/year/Sv. The boxes in a) denotes the detailed location of Irminger Sea (IS), Labrador Sea (LS) and the North Atlantic Current (NAC) in Fig. 26.

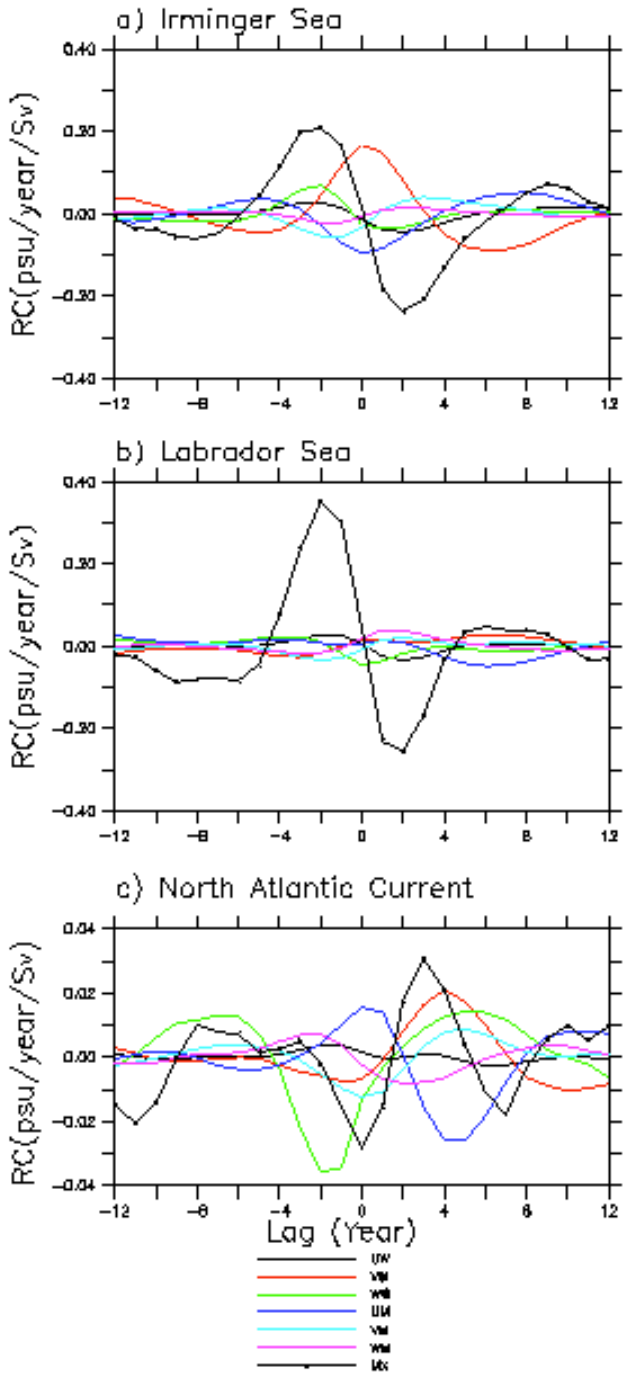

Fig. 26. Area-averaged lagged regression coefficient (RC, psu/year/Sv) from a) Irminger Sea, b) Labrador Sea and c) the North Atlantic Current between various tendency terms and the leading PC of the AMOC. The various tendency terms are anomalous/mean zonal transport (black/blue), anomalous/mean meridional transport (red/light blue), anomalous/mean vertical transport (green/purple), and vertical mixing (black dot). The detailed location for the three region is labeled in Fig. 25a..

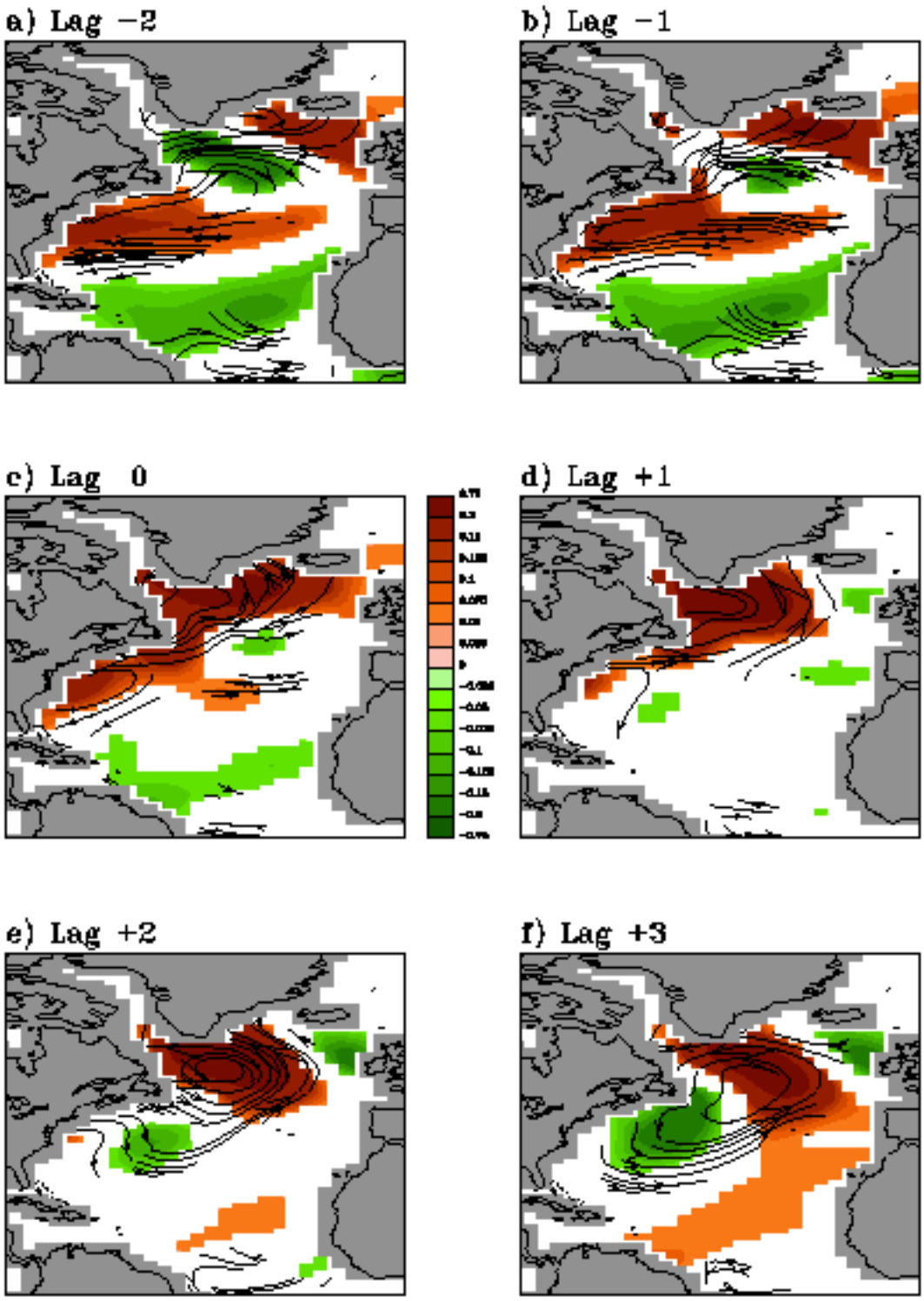

Fig. 27. Same as Fig. 19, but for temperature. The contour intervals are 0.025 ºC/Sv for values between -0.15 and 0.15 and 0.45 ºC/Sv for values between -0.75 and -0.40 and between 0.40 and 0.75. The data are omitted for values weaker than 1/15 of the strongest lagged regression coefficients.

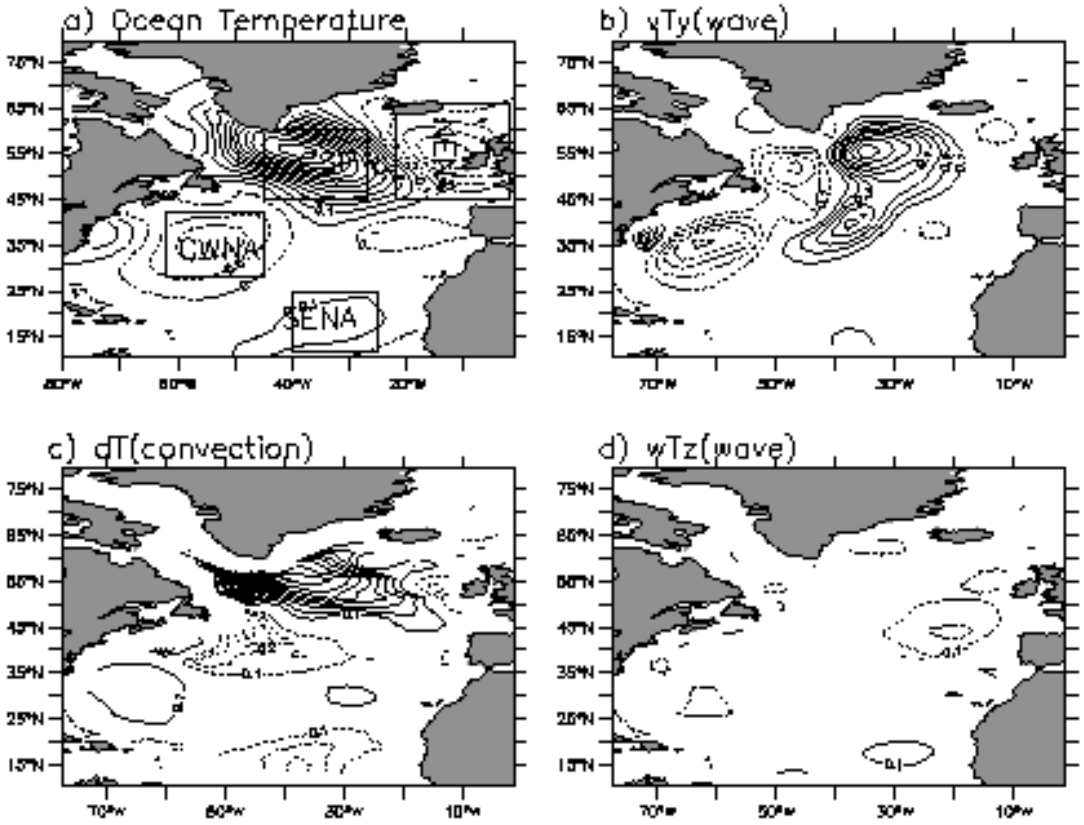

Fig. 28. The map of lagged regression of a) ocean temperature and b)-d) various temperature tendency terms upon the leading PC of AMOC in FOAM's control simulation at 30m depth during lag +2. The various tendency terms are b) anomalous meridional transport, c) convective mixing, d) anomalous vertical transport. The contour intervals are a) 0.05 ºC/Sv and b)-d) 0.01 ºC/year/Sv. The boxes in a) denotes the detailed location of Central Subpolar Gyre (CSG), Central West North Atlantic (CWNA), southeast North Atlantic (SENA) and Northeast North Atlantic (NENA) in Fig. 30.

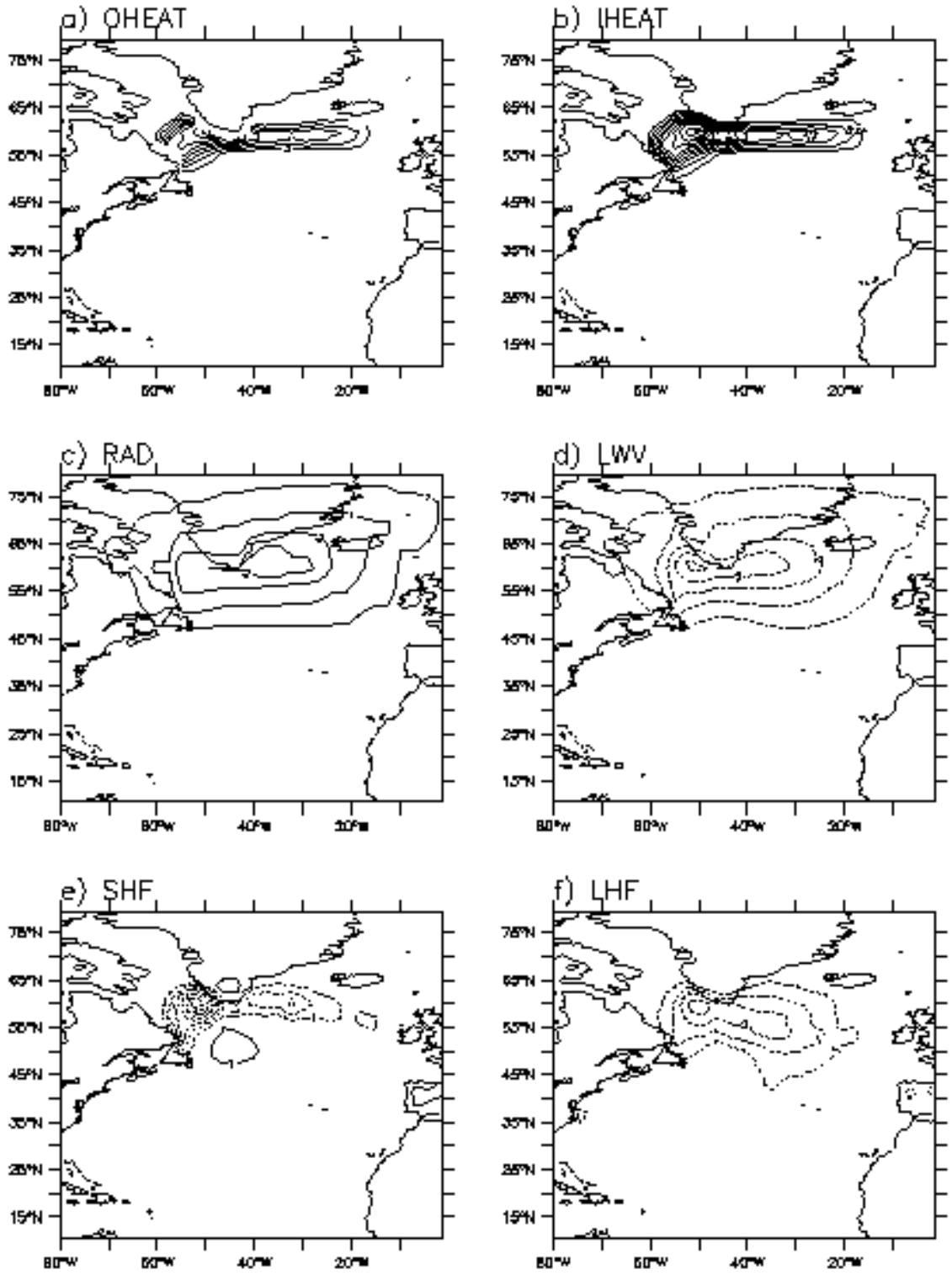

Fig. 29. The map of lagged regression of surface heat flux (ºC/year/Sv, positive into the ocean) upon the leading PC of AMOC in FOAM's control simulation at lag +2. a) total surface heat flux, b) surface heat flux due to ice melting, c) net short wave radiative flux, d) net long wave radiative flux, e) sensible heat flux, f) latent heat flux. The contour intervals are a)-b) 3 ºC/year/Sv and c)-f) 0.5 ºC/year/Sv.

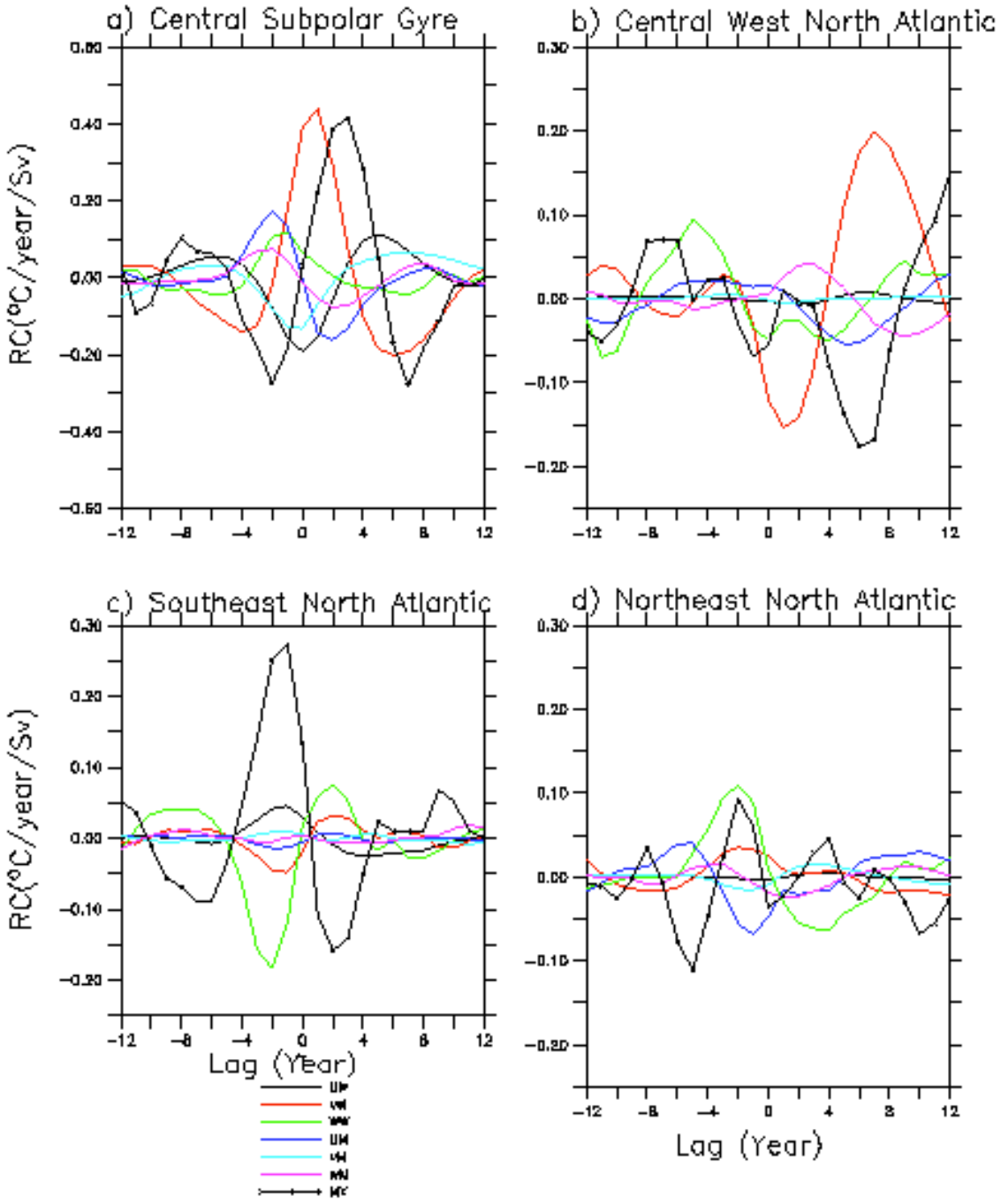

Fig. 30. Area-averaged lagged regression coefficient (RC, °C/year/Sv) from a) Central Subpolar Gyre, b) Central West North Atlantic, c) southeast North Atlantic and d) Northeast North Atlantic between various tendency terms and the leading PC of the AMOC. The various tendency terms are anomalous/mean zonal transport (black/blue), anomalous/mean meridional transport (red/light blue), anomalous/mean vertical transport (green/purple), and vertical mixing (black dot). The detailed location for the three region is labeled in Fig. 28a.

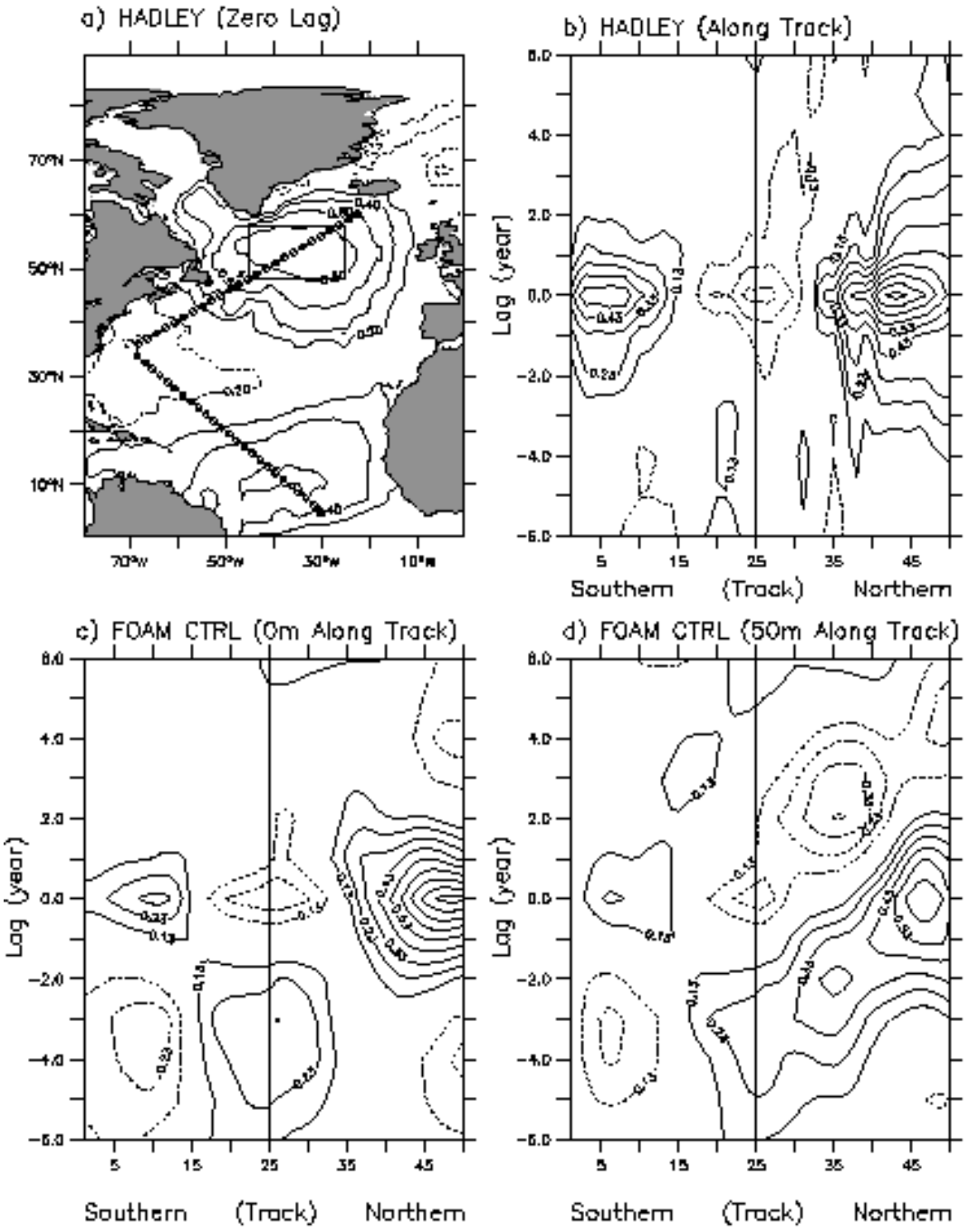

Fig. 31. a) The map of simultaneous correlation of winter (DJF) HadISST SST upon the area-averaged winter SST in the subpolar region (black box). The contour interval is 0.2. The black dot lines are the track along which the lagged correlation Hovmoller diagram is drawn in b)-d). b) Along track lagged correlation Hovmoller diagram for HadISST SST. Negative lags mean the SST along the track are leading the subpolar SST. The vertical line in the middle separates the southern track from the northern track. The contour interval is 0.1 and the correlation smaller than 0.13 is not drawn. c) same as b), but for FOAM control simulation. d) same as c), but for ocean temperature at 50m.